

**HEAT TRANSFER IN A BLADED MIXER: SCALE UP AND EFFECT OF
MATERIAL AND PROCESS PARAMETERS**

By

CLARA HARTMANSHENN

A dissertation submitted to the

School of Graduate Studies

Rutgers, The State University of New Jersey

In partial fulfillment of the requirements

For the degree of

Doctor of Philosophy

Graduate Program in Chemical and Biochemical Engineering

Written under the direction of

Benjamin J. Glasser

And approved by

New Brunswick, New Jersey

October 2020

ABSTRACT OF THE DISSERTATION

Heat Transfer in a Bladed Mixer: Scale Up and Effect of Material and Process Parameters

By CLARA HARTMANSHENN

Dissertation Director:

Benjamin J. Glasser

Granular materials make up a significant portion of the products manufactured by a variety of industries, including the pharmaceutical, bulk chemical, food, and construction industries. Yet, despite the ubiquity of particulate systems, a strong fundamental understanding of their behaviors is lacking. In the pharmaceutical industry, agitated drying of active pharmaceutical ingredients (APIs) is often a complex manufacturing step because it requires a combined understanding of the flow, heat transfer, mass transfer, and physicochemical properties of granular materials. During the process, a wet bed of API is heated in a jacketed cylindrical vessel while being agitated by a rotating impeller until the moisture content is reduced to a desired level. Complications often plague the procedure, including issues such as lengthy drying times, over-drying, nonuniform drying, agglomeration, attrition, and form changes. These circumstances make agitated drying a complicated process to understand and control. When considering scale up, these challenges are coupled with the difficulties typically associated with transferring knowledge from lab scale to pilot or manufacturing scale. As a result, it can be difficult to design a drying protocol that optimizes performance and can be translated from scale to scale while minimizing the risk for adverse conditions.

In this work, we decouple the problem and focus on studying the heat transfer aspect of agitated drying using a combination of computational and experimental techniques. More specifically, we studied the influence of material properties and operating conditions on both the rate of heat transfer and the heating uniformity for a bed of dry granular material in a bladed mixer. We conducted numerical simulations using the discrete element method (DEM) coupled with a conductive heat transfer model to assess the effect of the material thermal conductivity and the agitation rate on the heating performance. We also carried out experiments using a laboratory-scale agitated dryer and an infrared camera to assess the effect of the agitation rate and compare with the simulation results. Both the simulations and the experiments suggested that slowly agitating the bed considerably improved heat transfer, but that rapid agitation did not always enhance heat transfer. The results indicated that there is a critical rotation rate beyond which agitating the bed faster did not significantly improve heat transfer and that the critical rotation rate depends on the thermal conductivity of the material. Additionally, we developed a dimensionless scaling that enabled us to collapse the data together and obtain an equation relating the heating time of the bed to the thermal properties of the material and the agitation rate. We also quantified the heating uniformity and found that the temperature standard deviation depended on both the thermal conductivity and the agitation rate. For the parameters studied, we found that the scaling could be used to approximately predict both the mean temperature of the bed and the standard deviation over time. Finally, we demonstrated that heat transfer in a bladed mixer could also be studied using a more theoretical approach by calculating the conduction and granular convection fluxes in the bed. Overall, the findings from this

work improve fundamental understanding of heat transfer in a bladed mixer and provide insights into how the performance of agitated filter dryers and scale up of these processes can be optimized.

ACKNOWLEDGEMENTS

First and foremost, I would like to thank my thesis advisor, Prof. Benjamin Glasser for being a phenomenal research supervisor and mentor. I am grateful for his guidance with the direction of this project, his technical insights and exciting ideas, and for helping me grow both professionally and personally. I want to thank him for welcoming me into his research group and for making my PhD a truly wonderful experience. I would also like to thank the members of my thesis committee, Prof. George Tsilomelekis, Prof. Yee Chiew, and Dr. Matthew Metzger for their helpful suggestions and feedback. I appreciate their flexibility and availability, given the challenging times we currently face with Covid-19.

I thank our collaborators from Takeda, Dr. Charles Papageorgiou, Christopher Mitchell, and Justin Quon, as well as Prof. Johannes Khinast from Graz University of Technology in Austria for their contributions to this research. I appreciate the many helpful discussions and their careful review of my manuscripts. Special thanks to Takeda for providing our group with the equipment and making the experimental portion of this work possible. Many thanks to the students who have contributed to this project. In particular, I would like to acknowledge Prin Chaksmithanont, Maddie Halota, Sagar Patel, Digvijay Ghare, and Nabaneeta Chakraborty, for their assistance with both the experimental and the computational aspects of this project. I also thank Dr. Brenda Remy, Dr. Veerakiet Boonkanokwong, and Dr. Bereket Yohannes for building such a strong foundation for particle dynamics research in our group. I would also like to acknowledge financial support from the GAANN and the NSF GRFP fellowships.

I am especially grateful to my parents Celine and Christian, my siblings Laureline, Annefleur, and Milo, as well as my future family-in-law Beth Ann, Bill, and Danny for their unwavering support during the past five years. I also want to thank Megerle Scherholz, Jonathan Colon, Alison Acevedo, Silvio Dantas, Lisia Dias, and Pedro Gerum for their friendship and for making my time at Rutgers University an unforgettable experience.

Last but certainly not least, I would like to thank my fiancé Billy. I am extremely grateful for his endless encouragement, patience, and unconditional love throughout this experience. I would not have been able to achieve this dream without him by my side. Finally, I would like to dedicate this thesis to my grandfather, Dr. Richard Olivier Hartmanshenn, who inspired me to become a chemical engineer and encouraged me to pursue a doctoral degree. I am proud to follow in his footsteps.

TABLE OF CONTENT

ABSTRACT.....	ii
ACKNOWLEDGMENTS.....	v
LIST OF ILLUSTRATIONS.....	ix
LIST OF TABLES.....	xiii
1. INTRODUCTION.....	1
1.1 Motivation and Significance	1
1.2 Background: Flow and Heat Transfer in Granular Materials	3
1.3 Background: Agitated Drying of Active Pharmaceutical Ingredients	6
1.4 Literature Review: Experimental Work.....	10
1.5 Literature Review: Modeling Work.....	13
1.6 Remaining Questions	15
2. NUMERICAL AND EXPERIMENTAL METHODS.....	17
2.1 Numerical Methods.....	17
2.1.1 Flow and Contact Model.....	18
2.1.2 Heat Transfer Model and Assumptions	21
2.1.3 Modeling Scale Up	26
2.2 Experimental Methods	28
2.2.1 Experimental Setup.....	28
2.2.2 Experimental Procedure.....	33
2.2.3 Analytical Procedure.....	34
3. EFFECT OF THERMAL PROPERTIES AND AGITATION RATE ON HEAT TRANSFER.....	37
3.1 Visualizing Heat Transfer	38
3.2 Effect on the Rate of Heat Transfer	41
3.3 Nondimensionalization	49
3.4 Effect on the Bed Uniformity	57
3.5 Conclusions About the Effect of Thermal Properties and Agitation Rate on Heat Transfer	64
4. INFRARED TEMPERATURE EXPERIMENTS AND VALIDATION OF DEM SIMULATIONS	66
4.1 Heat Transfer Experiments	66
4.2 Comparison with Heat Transfer Simulations.....	78
4.3 Conclusions About Infrared Temperature Experiments and Validation of DEM Simulations	87
5. SCALE UP OF HEAT TRANSFER	90
5.1 The Effect of the H/D Ratio.....	91
5.2 The Effect of the D/d Ratio.....	106
5.3 Conclusions About Scale Up of Heat Transfer.....	114
6. CONDUCTION AND GRANULAR CONVECTION	116
6.1 Heat Transfer Through Conduction.....	116
6.2 Explaining Unexpected Trends from Chapter 3 Using Conduction at the Wall...	120
6.3 Heat Transfer Through Granular Convection	128
6.4 Conclusions About Conduction and Granular Convection.....	131

7. CONCLUSIONS AND FUTURE WORK	133
7.1 Conclusions	133
7.2 Future Work	140
APPENDIX.....	147
A.1 Appendix for Chapter 3.....	146
A.2 Appendix for Chapter 4.....	148
A.3 Appendix for Chapter 5.....	149
NOTATION.....	154
List of Variables.....	153
List of Subscripts	156
List of Greek Letters	156
ACKNOWLEDGMENT OF PREVIOUS PUBLICATIONS.....	159
REFERENCES.....	160

LIST OF ILLUSTRATIONS

Figure 2.1: Modeling approximation of the bladed mixer system.....	17
Figure 2.2: Particle collision with contact radius a and normal overlap δ_n	23
Figure 2.3: Experimental setup of the agitated dryer system. The image shows the cylindrical vessel with the heating jacket, the impeller, the motor, and the aluminum stand.	29
Figure 2.4: Overview of the experimental setup. The image shows the agitated dryer system, the HMI, and the circulator.....	30
Figure 2.5: (a) Glass beads used in the heating experiments. (b) Optical microscope image of the glass beads. Image credit: James Scicolone.....	31
Figure 2.6: (a) Side view and (b) top view of the experimental setup with the laboratory-scale agitated dryer and the infrared camera.....	32
Figure 2.7: Effect of removing the contribution of the impeller on (a) the mean temperature of the surface, (b) the standard deviation of the surface.	36
Figure 3.1: Particles heating over time for $k = 10$ W/mK and $\omega = 10$ rpm. Particles start at room temperature (298 K) and are heated by the walls at a temperature of 323 K.	39
Figure 3.2: (a) Effect of agitation rate for the same thermal conductivity $k = 50$ W/mK when time $t = 30$ s. (b) Effect of thermal conductivity for the same agitation rate $\omega = 10$ rpm when time $t = 60$ s. (c) Effect of thermal conductivity for the same agitation rate. ..	40
Figure 3.3: Mean temperature of the bed over time as a function of agitation rate and conductivity, where (a) $k = 1$ W/mK, (b) $k = 100$ W/mK.....	43
Figure 3.4: Natural logarithm of dimensionless temperature driving force over time for the conditions $\omega = 100$ rpm, $k = 50$ W/mK (dark green) and $\omega = 25$ rpm, $k = 10$ W/mK (light blue).....	44
Figure 3.5: (a) Thermal time τ_b as a function of agitation rate for varying conductivity. (b) Effective heat transfer coefficient h_{eff} as a function of agitation rate for varying conductivity. (c) Blow-up of heat transfer coefficient for slow agitation rates. (d) Average coordination number as a function of agitation rate. The legend in Figure 3.5a also applies to Figure 3.5b and 3.5c.	46
Figure 3.6: Three relevant timescales: (a) bed thermal time, (b) particle thermal time, (c) contact time.....	50
Figure 3.7: Nondimensionalization of the results showing different heating regimes based on ϕ	54
Figure 3.8: (a) Temperature evolution of an individual particle (gray) compared to the mean temperature (red). (b) Temperature evolution of all particles (gray) compared to the mean (red).	58

Figure 3.9: Frequency distribution of particles in the bed for low ϕ (0.5 rpm, 100 W/mK), medium ϕ (25 rpm, 50 W/mK), and high ϕ (100 rpm, 1 W/mK) at the time when $T_b = (T_w - T_0)/2$.	59
Figure 3.10: Normalized standard deviation over time for a material with (a) low conductivity ($k = 1$ W/mK) and (b) high conductivity (100 W/mK) for varying agitation rates. Data are fitted to an exponential decay equation with coefficients γ and β (black solid line). The legend in Figure 3.10b is applicable to Figure 3.10a.	61
Figure 3.11: Coefficients (a) γ and (b) β of the exponential decay as a function of ϕ and τ_b respectively. The data have been codified into symbols according to thermal conductivity.	63
Figure 4.1: Thermal images for glass beads over time. The impeller agitation rate was set to 5 rpm.	67
Figure 4.2: Thermal images of the bed surface over time for different agitation rates.	69
Figure 4.3: (a) Temperature of the bed surface versus time for 5 rpm agitation rate. The plot shows the reproducibility of the experiment over 3 trials. (b) Dimensionless temperature versus time for 5 rpm agitation rate.	71
Figure 4.4: (a) Mean temperature of the bed surface over time for different agitation rates. (b) Heating time of the bed surface for different agitation rates. (c) Effective heat transfer coefficient of the bed surface for different agitation rates.	73
Figure 4.5: Histograms showing the temperature distribution of the bed surface after $t = 1$ min, 5 min, 10 min, and 40 min of heating for an impeller agitation rate of (a) 0 rpm, (b) 5 rpm, (c) 10 rpm, (d) 100 rpm.	74
Figure 4.6: Temperature distribution of the bed surface after $t = 5$ min of heating for different impeller agitation rates.	75
Figure 4.7: (a) Temperature standard deviation of the bed surface over time for 5 rpm agitation rate. The plot shows the reproducibility of the experiment over 3 trials. (b) Temperature standard deviation of the bed surface for different impeller agitation rates. The error bars represent 3 replicates for each agitation rate.	76
Figure 4.8: (a) Close-up of the agitated dryer system. (b) Model representation of the system used in the DEM simulations.	78
Figure 4.9: Using the dimensionless scaling to calibrate k . (a) Uncalibrated simulations ($k = 5$ W/mK), the fitting equation, and the experiment used for the calibration (25 rpm). (b) Calibrated simulations ($k = 2.5$ W/mK) and the experiments for 5 rpm, 10 rpm, 25 rpm, and 100 rpm.	81
Figure 4.10: Comparison of the experimental thermal images (left) and the DEM simulations (right) for different agitation rates after 1, 5, and 10 minutes.	83
Figure 4.11: Comparison of the experimental and simulation results for different agitation rates: (a), (b) Mean temperature of the bed surface over time. (c), (d) Dimensionless temperature of the bed surface over time. (e) Heating time of the bed surface. (d) Heat transfer coefficient of the bed surface.	85

Figure 4.12: (a) Experimental standard deviation of the bed surface temperature over time for different agitation rates. (b) Simulation standard deviation of the bed surface temperature over time for different agitation rates.	87
Figure 5.1: (a) Oblique view and (b) side cross-section view of particle beds with different H/D at time = 100 s.	92
Figure 5.2: (a) Mean temperature over time for beds with different H/D. (b) Dimensionless temperature over time for beds with different H/D. The legend in Figure 5.2a also applies to Figure 5.2b. (c) Relationship between the heating time τ_b and H/D.	95
Figure 5.3: Relationship between H/D and (a) AM* ratio of the heated surface area A of the vessel to the mass M of material normalized over the area $A_{shallow}$ and mass $M_{shallow}$ for a shallow bed, (b) normalized mean % contact overlap between particles in the bed, (c) mean coordination number in the bed.	98
Figure 5.4: Horizontal slides of the bed right above the blades ($H = 3.0$ cm) at time = 100 s. Slices are shown for a shallow bed, an intermediate bed, and a deep bed.	102
Figure 5.5: Visuals for beds with H/D = 0.53, 1.19, and 1.54 after 0.5, 2, and 10 revolutions. Particles are color-coded dark red and gray at time = 0 s to show particle mixing over time.	103
Figure 5.6: Relative standard deviation as a function of impeller revolutions for different bed heights.	105
Figure 5.7: (a) Oblique view and (b) Side cross-section of beds with different D/d at time = 100 s. The legend in Figure 5.7a is also applicable to Figure 5.7b.	108
Figure 5.8: (a) Mean temperature over time for beds with different D/d (colors) and different agitation rates (solid or dotted line). (b) Heating time as a function of D/d for two different agitation rates.	110
Figure 5.9: Relationship between the D/d ratio and: (a) AM* ratio of the heated surface area A of the vessel to the mass M of material normalized over the area $A_{shallow}$ and mass $M_{shallow}$ for a shallow bed, (b) normalized mean % contact overlap between particles in the bed, (c) mean coordination number in the bed, (d) relative standard deviation as a function of impeller revolutions.	112
Figure 5.10: Visuals for beds with D/d = 25.0, 37.5, 50.0, and 62.5 after 0.5, 2, and 10 revolutions. Particles are color-coded dark red and gray at time = 0 s to show particle mixing over time.	113
Figure 6.1: Evolution of the conductive flux over time in the radial (R), theta (θ), and axial (Z) direction for a shallow bed with H/D = 0.46.	118
Figure 6.2: (a) Radial conductive flux over time for beds with different H/D. (b) Radial conductive flux averaged over time versus H/D.	119
Figure 6.3: Heat transfer coefficient for a material with a thermal conductivity of (a) 100 W/mK and (b) 1 W/mK.	121
Figure 6.4: Mean temperature difference between the wall temperature and the temperature of the particles touching the wall over time for different agitation rates. The	

simulations are for materials with a thermal conductivity of (a) $k = 100$ W/mK and (b) $k = 1$ W/mK.	124
Figure 6.5: Mean contact overlap between the wall and particles at the wall for materials with a thermal conductivity of (a) 100 W/mK and (b) 1 W/mK.	125
Figure 6.6: Total number of wall contacts for materials with a thermal conductivity of (a) 100 W/mK and (b) 1 W/mK.	126
Figure 6.7: Wall conduction flux summed over time as a function of agitation rate of a material with a thermal conductivity of (a) 100 W/mK and (b) 1 W/mK.	127
Figure 6.8: Granular convection flux density over time in the radial R , theta θ , and vertical Z directions.	130
Figure 6.9: Granular convection over time in the radial, theta, and vertical direction for different agitation rates.	131
Figure A.2.1: (a) Experimental standard deviation of the bed surface temperature over time for different agitation rates. (b) Simulated standard deviation of the bed surface temperature over time for different agitation rates.....	139
Figure A.3.1: (a) Effect of varying the shear modulus on the heating time for beds with different fill heights. (b) Effect of no agitation and 5 rpm agitation rate on the heating time for beds with different fill heights.....	140

LIST OF TABLES

Table 2.1: Geometry dimension of agitated bed dryer for DEM simulations.	18
Table 2.2: Parameter values for DEM simulations.	20
Table 2.3: Material properties of the glass beads and operating conditions.	31

1. INTRODUCTION

1.1 Motivation and Significance

The processing and production of granular materials play a dominant role in a wide variety of industries, including the pharmaceutical [1], bulk chemical [2], food [3], and construction industries [4, 5], to name a few [6]. A closer look at the chemical sector shows that nearly half of manufactured products and over three-quarters of raw materials involve particulates [7]. Yet, despite the ubiquity of particulate systems across nature and manufacturing industries, a strong fundamental understanding of their behavior is lacking. Granular materials are composed of discrete particles, and hence, cannot easily be represented by continuum mathematical models. The intrinsic stress and contact heterogeneities that exist within particulate systems make the study of heat transfer in these materials rather complicated [8]. Particle interactions can further convolute things as they make granular materials prone to effects such as agglomeration, attrition, and segregation [9].

In the pharmaceutical industry, agitated drying of the drug substance, i.e., the active pharmaceutical ingredient (API), is a manufacturing step that requires a combined understanding of the flow, heat transfer, and mass transfer in granular materials within the transient system. This understanding, however, exists in a rudimentary form. Agitated drying is a process in which a wet bed of API is dried using heating and mixing, often under vacuum. One of the more commonly used equipment units for API drying is the bladed mixer [10]. This geometry can be simplified as a vertical cylindrical vessel in which wet particles rest at the bottom of the unit. Heat is typically supplied via conduction through a heated jacket around the wall of the vessel while an impeller rotates to distribute heat and

promote evaporation throughout the bed. Heat and mass transfer occur simultaneously: the average temperature of the bed rises to approach the temperature of the heating jacket while the moisture level decreases as the liquid (solvent or water) evaporates.

Drying is typically one of the last steps in API synthesis and is arguably one of the most delicate [11]. Its success directly impacts the API's critical quality attributes (CQAs) and therefore has the potential to affect subsequent manufacturing steps [12, 13]. Selecting an optimal impeller agitation protocol is a key element of the agitated drying process. Insufficient agitation can lead to nonuniform drying and hot spots, while too much agitation can lead to attrition. Attrition affects the particle size distribution, which is often an important CQA [14]. Finding an optimal agitation protocol that enhances heat transfer in the bed, while minimizing the potential for attrition and/or agglomeration, is often an important consideration in agitated drying. Other complications that often plague the procedure include lengthy drying times, over-drying, nonuniform drying, agglomeration, and form changes [15]. These issues make agitated drying a complicated process to understand and control. Furthermore, when considering scalability of the process, these challenges are coupled with the difficulties typically associated with transferring knowledge from lab scale to pilot or manufacturing scale. As a result, designing an appropriate drying protocol that optimizes heat transfer and can be translated from scale to scale while minimizing the risk for adverse conditions can be quite difficult.

To this day, despite the widespread implementation of agitated drying, fundamental understanding of how heat transfer, mass transfer, and changes in physicochemical properties occur during the process remains limited. The challenge stems from the fact that too many phenomena occur simultaneously, making it difficult to understand how different

input variables (e.g.: material properties, operating conditions, equipment scale) influence the output respectively (e.g.: drying time, product quality). The research presented in this dissertation tackles this challenge by isolating the different facets of agitated drying and focusing on the heat transfer. This approach significantly simplifies the problem and allows for a deeper investigation of the contribution of heat transfer during agitated drying. More specifically, the project consists of studying heat transfer through dry granular material in a bladed mixer using both numerical simulations and experiments. Of course, heat transfer is only one aspect of agitated drying and more work is needed to understand how mass transfer and physicochemical properties of the material influence the process. However, fundamental research like this has the potential to greatly aid in the development of more efficient and robust drying protocols.

1.2 Background: Flow and Heat Transfer in Granular Materials

The presence of particulate systems around us is more extensive than most probably realize or pay attention to. In our daily lives, granular materials appear in the form of construction supplies (soil, rocks, sand), cooking ingredients (spices, sugar, flour, coffee, nuts), and household items (laundry detergent, dishwasher cleaner). However, despite the ubiquity of granular materials, scientific knowledge of their properties and behaviors still lacks in certain respects. The difficulty associated with granular materials stems from the fact that they behave neither like a true solid, a true liquid, nor a true gas. One grain is a solid and behaves as one, but the same cannot be said of a collection of grains. For example, if a pile of sand rests at a slope below its angle of repose, the material will rest like a solid despite the gravitational forces acting on it. If the pile reaches a slope greater than the angle

of repose, sand particles will flow down, similarly to a flowing liquid, until the pile reaches the angle of repose again [16]. Analogous phenomena are observed in snow avalanches, where the mass of accumulated snow exceeds the resistance of the slope and falls until a balance can be achieved again [17]. The inability of particulate systems to be classified as a solid, liquid, or gas has even led some scientists to argue that they should be considered as an additional state of matter [16].

Granular media consist of a conglomeration of discrete particles. While behavior at the macroscopic scale is often the primary scale of interest, phenomena occurring at underlying scales can affect large-scale behavior and therefore cannot be neglected [18]. Heterogeneities at the microscopic level can lead to uneven distribution of properties such as stress at the macroscopic scale. To this end, the characteristics of granular materials must be specified for either a single particle or bulk quantities. A common example is true density versus bulk density [19, 20]. The true density of a single particle is easily measurable if one can obtain a block of continuous material. Obtaining an accurate value for the bulk density for a particulate system can prove to be more troublesome to measure because it encompasses the solid as well as the air between the particles. The amount of air within the material can be altered if the material is compressible, making the bulk density highly variable. Inhomogeneities within the material can also make it difficult to obtain a single value for bulk density that properly represents the material in its entirety.

Acquiring insight into the flow of particulate systems can be a convoluted matter. Particles in granular media are subjected to body forces, frictional forces, and inelastic collisions and can move using gliding, spinning, or rolling motions. Cohesive forces can also exist between particles either due to electrostatic interactions or due to the presence of

moisture in the material. The flow of particulate systems has been categorized according to three regimes: quasi-static, intermediate, and rapid flow [21]. The quasi-static regime is characterized by low shear and high concentration, where particles have close nearly constant contact with their neighbors. On the other end of the spectrum, a rapid flow regime occurs in conditions with low concentration and high shear. Considerable experimental and simulation efforts have been undertaken to improve knowledge of the rheology of particulate systems in various geometry, including plane shear flow [22, 23], Couette flow [24, 25], and rotating drums [26, 27]. Pioneering work by Cundall and Strack on the discrete element method has greatly benefitted modeling efforts geared towards simulating particulate systems in these geometries [28].

Heat transfer through granular material has also been studied extensively but some scientific findings remain partially empirical [8, 29]. Heat transfer in granular materials is complex and can take place simultaneously in the form of conduction, convection, and radiation. Thermal diffusion occurs through a single grain when the core temperature is different from that of the outer layer of the particle. Conduction ensues when particles of unequal temperature come into contact and exchange heat. Convection occurs between the solid particles and the fluid in the void spaces. Lastly, heat transfer through radiation can become important at high temperatures [8]. Typical mathematical models describing heat transfer in granular beds are based on those applying to liquids and solids but may contain fitting coefficients or lumped parameters to better describe the material itself or its interactions with its environment. Due to the discrete nature of granular materials, models often contain “effective” parameters, such as effective heat transfer coefficients or effective conductivity, to describe heating of the bulk material [30-33]. This is further complicated

by the fact that bulk properties may vary with time if dynamic conditions exist. For example, thermal conductivity of the bulk is a function of solid conductivity but also varies according to parameters such as particle shape and size [34], moisture [35, 36], and void fraction [37], all of which may change with time during agitated drying.

Several dimensionless groups exist to describe how the different modes of heat transfer scale in traditional states of matter, such as solids, liquids, and gases. For example, the Peclet number describes the ratio of the heat transferred through the motion of a fluid to the heat transferred by thermal conduction. The Biot number refers to the ratio of the heat transfer resistances inside of a solid and at the surface of a solid. The Nusselt number is the ratio of convective to conductive heat transfer at a boundary in a fluid. In the literature, several studies have proposed methods to adapt the use of these dimensionless groups to granular materials [38-40].

1.3 Background: Agitated Drying of Active Pharmaceutical Ingredients

Despite the challenges associated with working with particulate systems, they remain an essential part of the pharmaceutical industry. Oral solid dosage forms such as tablets and capsules account for 80% of products for US consumption [1], and many of the APIs and excipients used to make these drug products exist in the form of powders. As a result, particulates are widely present throughout the drug production chain, in steps such as drying, milling, granulation, blending, and tablet compaction [1]. Once the API is synthesized, it is purified and crystallized to achieve the appropriate crystal form. After crystallization, the produced slurry must be filtered and dried in order to obtain a flowable

API powder that can later be blended with other excipients to form a drug product that can be pressed into tablets.

While a variety of drying equipment are used in the pharmaceutical industry, one of the most popular types is a bladed mixer [10]. The apparatus is composed of a cylindrical vertical vessel with a heated jacket and an impeller, which can also be heated in some cases. The bladed mixer geometry offers several notable benefits in terms of design, such as a high thermal efficiency, the ability to process a wide variety of materials, low cost of operation, and environmental advantages [41]. Furthermore, it can be equipped with a filter (in a unit called an agitated filter-bed dryer) and thereby enable API filtration to be carried out in the same unit prior to drying [42]. Using the same unit for multiple stages of the process is a tremendous benefit because it reduces the potential for product loss and limits the risk for worker exposure to potent and possibly toxic materials that can occur when transferring material to a different equipment.

Drying of granular materials is a complex dynamic problem in which heat transfer, mass transfer, and sometimes physicochemical changes occur simultaneously. Heat transfer in agitated drying can occur primarily via two modes: conduction and convection [8]. Conduction occurs as the vessel wall jacket supplies thermal energy to the layer of adjacent particles. Particle-to-particle conduction also exists when particles collide and exchange energy through the surface area in contact. Convection takes place between the fluid and the adjacent particles. Radiation would become significant only if the processing temperatures were much higher than are currently used in the pharmaceutical industry and so its contribution to heat transfer can be deemed insignificant compared to that of conduction and convection [43].

Mass transfer during agitated drying occurs as the solvent permeates through the particle bed and evaporates. This process is complex, as the changing levels of solvent during drying affect the degree of cohesion between the particles and significantly influences how the bed flows. At the beginning of the process, the bed is very wet and solvent at the surface of the bed readily evaporates so the drying rate is relatively fast [44]. The high solvent content in the bed lubricates the particles and allows them to slide easily past each other, leading to relatively good flowability [45]. As the drying front advances, it becomes increasingly difficult for moisture to reach the surface leading to the formation of wet pockets of solvent within the bed [46]. Mixing enables a more even distribution of moisture across the bed by breaking these pockets of solvents and promoting mass transfer to the free surface. This intermediate stage of moisture level, where the bed is neither very wet nor very dry, is termed the “sticky point” because of the high level of cohesion that exists amongst particles during this stage [47]. Thin liquid bridges form between particles such that two united neighboring particles experience a strong cohesive force preventing them from detaching. The flowability of the powder during this phase of drying is poor and mixing often leads to agglomeration of particles [48, 49]. Further drying of the bed helps reduce the cohesive forces induced by the liquid bridges and improve the flowability of the granular material [50]. Eventually, the rheology of the bed approaches a more frictional flow. At this point, too much mixing when the material is dry may result in attrition, as shear forces from fast or long mixing may be too strong and lead to breaking of particles’ crystal lattice [51].

Many complications can occur during agitated drying. Because APIs tend to be temperature-sensitive, heating must be carefully monitored and controlled to prevent

degradation of the API, generation of impurities, loss of crystallinity, nonuniform drying, or incomplete drying [15]. A desired final liquid content must be decided upon in order to design the heating protocol, as insufficient drying can result in: a) the presence of water that can lead to microbial growth that can contaminate the product or b) the presence of residual solvents that exceed allowable toxicity limits [52]. Differentiation between free surface moisture and bound moisture in the drug substance must also be established [53]. Heating temperatures are typically kept at low levels, as using elevated temperatures could destroy the chemical stability of API and hinder the therapeutic abilities of the molecule. In addition to damaging the API, high temperatures could increase the solubility of the API in the remaining solvent, leading to partial dissolution of the API and the formation of agglomerates [54]. Unfortunately heating large quantities of wet material at low temperatures can lead to exceedingly long drying times, especially at the pilot plant level or at the industrial scale. In fact, API drying is known to be a lengthy process that can sometimes bottleneck the manufacturing chain [11]. Depending on the market demand of the drug and the rate at which it needs to be supplied, such lengthy processing times may be prohibitive. Additional physicochemical changes occurring during drying may lead to potential complications and must be considered if the API in question is a hydrate or solvate, or if it has multiple polymorphs. If the desired form of an API is a hydrate or a solvate, then one must be careful not to over-dry the material [55]. Polymorphism changes during drying can also impact crystal morphology, as shown for cubic and needle-like particles by Lekhal *et al.* [51].

Agitated drying can influence the CQAs of the API and must therefore be conducted carefully. For example, if agglomeration or attrition occur during the process, it

can change the particle size distribution of the API. Particle size can affect how readily an API dissolves in gastrointestinal fluids, and therefore, influences its bioavailability [56, 57]. Large particles of API may be unable to dissolve quickly enough in the human body and may therefore not achieve the desired therapeutic effect [56]. While smaller particles are typically desirable for bioavailability purposes, they can often cause processing problems. Fine particles are known to form dust that endanger the safety of operators, are susceptible to electrostatic or cohesive forces, and tend to stick to equipment surfaces [58]. Attrition can also form multimodal particle size distributions which can affect the downstream stages of manufacturing, such as blending with excipients prior to tablet compression [59].

1.4 Literature Review: Experimental Work

Significant experimental work has been done to improve process understanding of the different phenomena occurring during agitated drying. To overcome the challenges associated with understanding the process, some researchers have simplified the problem by isolating individual elements of drying and studying them on their own. For example, Lamberto *et al.* [15] conducted experiments where they investigated form conversion and solvent entrapment during agitated drying at different scales. Am Ende *et al.* [10] described different moisture regimes (pendular, funicular, capillary) that occur during drying and found that torque measurements could be used as a tool to determine when to agitate to mitigate attrition and agglomeration based on these regimes. Lekhal *et al.* [47] discussed the competition between attrition and agglomeration during drying and suggested that they happen based on the moisture content and whether it's above or below a "critical" moisture

level. Papageorgiou *et al.* [54] developed a screening protocol to determine the risk for agglomeration during agitated drying. They found that a resonant acoustic mixer could replicate the conditions that are conducive to granule formation in an agitated dryer and could be used to study agglomeration of APIs using a smaller quantity of material. Remy *et al.* [60] studied segregation of particles using dry glass beads in an agitated dryer. They found that the degree of polydispersity of the material strongly affects its propensity for segregating. The influence of impeller properties on the rate of mixing have also been examined. For example, Boonkanokwong *et al.* [61, 62] carried out experiments where they tested the mixing performance of impellers with different numbers of blades and several blade angles in a laboratory-scale agitated dryer. Sahni *et al.* [63] conducted a parametric investigation of the operating conditions that affect drying performance. More specifically, they quantified the effect of the wall temperature, the impeller speed, and the fill level of the material on the drying performance of an agitated filter dryer.

Over the recent decade, the pharmaceutical industry has worked toward incorporating numerous process analytical technologies (PAT) into their unit operations to track the drying process. For example, as was previously discussed, torque is often used as a tool to predict agglomeration and attrition in the particle bed during drying. Near infrared spectroscopy (NIR) has also been used to monitor drying processes [64, 65]. Zhou *et al.* [53] discussed how NIR could be used to determine and differentiate surface and bound water in drug substances. Heat transfer during drying is often quantified by recording the temperature of the bed over time. Typically, thermocouple probes are inserted into the bed and measure the temperature [66, 67]. The challenge with using thermocouples stems from the fact that they can only provide a temperature measurement at a single point in the bed.

As a result, the location of the thermocouple in the bed could significantly influence the temperature measurement, particularly if the bed temperature is not completely uniform. Additionally, temperature data measured from thermocouples can only be collected when there is no agitation or else if agitation is applied, the thermocouples should be positioned at a point above the agitator so that they are not disturbed by the motion of the impeller. Otherwise, the probe could act as a baffle and influence the flow of the particles. Fewer studies report on the use of noninvasive temperature measurements in agitated drying processes. Thermal imaging using an infrared (IR) camera has been used in other equipment, like a rotary drum for example [68]. IR imaging works by measuring infrared energy and reporting it as a temperature value. It can capture temperature data for an entire surface and can therefore provide large amounts of information. Up until now, little work had been published on the use of infrared imaging as a PAT tool for agitated drying.

Scale up of agitated drying is an important consideration in the pharmaceutical industry. Scale up is challenging because several factors change as a function of equipment scale, such as the amount of material that needs to be dried, the shear forces in the particle bed, the hydrostatic pressure in the bed, the rate of mixing, and the surface area available for heat transfer among others. Lamberto *et al.* [69] carried out experiments where they studied hydrostatic forces in agitated dryers at the laboratory-scale and the pilot-plant scale. They placed a weight onto a particle bed in a laboratory-scale agitated dryer and showed that this method could be used to reproduce the large hydrostatic forces experienced by particles in the pilot plant. Am Ende *et al.* [10] used a similar experimental setup and described a protocol to predict an API's propensity to undergo attrition. Remy *et al.* [70]

further expanded on that work by using torque measurements to correlate the amount of shear stress experienced by the API particles to the degree of attrition.

1.5 Literature Review: Modeling Work

Another technique that researchers are using to study the underlying physics of particle beds in agitated dryers is mathematical modeling. In Mollekopf and Schlunder's "penetration model", a wet bed of particles undergoes a sequence of static heating with intermittent mixing steps [71]. During the static period, heat penetrates through the wet bed and is modeled as a drying front. Mixing is modeled with empirical relations based on the Froude number and the contact time between the bed and the geometry. However, despite their ease of use, penetration models have several limitations. Not only do such models require adequate experimental data in order to function, but they also fail to provide information about particle property distributions, and may be difficult to apply for scale up scenarios [72]. Additionally, their accuracy is particularly limited for scenarios where complexities such as particle agglomeration occurs [73].

Due to the discrete nature of particulate materials, there has been a shift in the last decades towards exploring models that make use of the discrete element method (DEM). DEM modeling employs a time-stepping algorithm that integrates Newton's equations of motion for each particle in the system and provides information on each particle's position, velocity, and resultant forces at a given time [28]. The concept of DEM modeling is not a new one, as it was first introduced in the 1970s by Cundall and Strack [28], but recent technological advances and improvements in computational power have increased the

usefulness of DEM modeling and have made it a promising and popular tool to study particulate systems.

DEM modeling has been successfully leveraged to evaluate the effect of numerous parameters on flow and mixing of granular materials in bladed mixers. Notably, the effects of particle polydispersity, particle shape, fill level, impeller positioning and rotation rate, number of impeller blades, particle and wall friction, and moisture content have been reported in literature [60, 61, 74-79]. These studies have generated valuable insights into understanding how different operating parameters can influence mixing efficiency and flow behaviors such as cohesion, segregation, and attrition. For example, in Remy *et al.* [78], DEM modeling was used to demonstrate how the fill height of the material and the vessel diameter affect mixing patterns and efficiency, particle velocities, torque, and hydrostatic pressure in the bed.

At the same time, considerably less DEM modeling work has been carried out for heat transfer in bladed mixers. In the past, DEM modeling efforts for heat transfer in granular materials have focused on geometries, such as rotary drums [43, 80-83], fluidized beds [84], chute flows [85], pneumatic conveying [86], shear flows [39, 87], or static packed beds [33]. Prior to this research, few publications existed on DEM modeling for heated bladed mixers. Chaudhuri *et al.* [11] have done simulations where they modeled the drying process taking into account heat transfer between particles, heat transfer through the liquid, evaporation of the liquid, and the effect of liquid on the flow of the particles. This leads to a fairly complex model with a number of unknown or adjustable parameters. It is therefore challenging to validate the model and difficult to examine how the results change with scale. In this work, we use a simpler model where we only consider heat transfer

between the particles to shed light on the effect of material properties, operating conditions, and scale on the heating process. By focusing on heat transfer only, we isolate one aspect of the drying process and we can more readily do validation experiments. It is possible for later work to integrate mass transfer and contrast the case of heat transfer alone with the more complex case of drying.

1.6 Remaining Questions

Despite the widespread implementation of agitated drying, fundamental understanding about how heat transfer, mass transfer, and changes in physicochemical properties occur during the process remains limited, particularly when it comes to scaling up the process [70]. The research presented in this dissertation focuses on investigating the heat transfer aspect of agitated drying by studying dry granular material in a bladed mixer. This approach simplifies the problem significantly and allows for a deeper analysis of the underlying phenomena. The objective of this work is to answer questions such as:

- How do material thermal properties play a role in how a material heats up in a bladed mixer?
- Which operating conditions influence heat transfer?
- How can operating protocols be optimized to maximize the rate of heat transfer while mitigating the risk for adverse effects?
- How does heat transfer change during scale up of the process?
- Can thermal imaging be used as a noninvasive PAT tool for quantifying heat transfer in a bladed mixer?

Chapter 2 of this dissertation provides an overview of modeling and experimental techniques used in this work. The methods section for the numerical simulations includes a description of the heat transfer theory and the contact model used in this work as well as the input parameters. In Chapter 3, DEM modeling is used to investigate how the thermal properties of a material and the agitation rate influence heat transfer in a bladed mixer. The effects of these parameters on both the average temperature in the bed and the temperature distribution is analyzed. Nondimensionalization of the system is also discussed. Chapter 4 presents heat transfer experiments carried out in a laboratory-scale agitated dryer using an infrared camera. The experiments quantify the effect of the impeller agitation rate on the surface temperature of the bed and its uniformity. Comparisons with the modeling results are also presented. Chapter 5 describes how the model is applied to study scale up of the process. More specifically, DEM simulations are conducted to investigate how the fill height and the mixer diameter influence heat transfer through a particle bed. Chapter 6 uses a fundamental approach to explore heat transfer theory for granular material in a bladed mixer by computing the conduction flux and the granular convection flux for different scenarios. Finally, Chapter 7 summarizes the significant findings and important conclusions from this work and provides suggestions for future work.

2. NUMERICAL AND EXPERIMENTAL METHODS

2.1 Numerical Methods

Simulations were conducted using the commercial software EDEM[®], while data analysis and visualization was carried out using MATLAB[®]. EDEM[®] models each particle as a distinct entity and considers a granular material to be an assembly of these particles. EDEM[®] relies on a time-stepping algorithm to update the position and velocity of each particle. We assume non-cohesive particles and utilize a contact model based on Hertz-Mindlin theory [88] and a conduction heat transfer model. The model is applied to an agitated dryer geometry. Such dryers are fairly simple in form in that they can be approximated as a cylinder with a rotating impeller with heated jacketed walls. Figure 2.1 depicts a general visual of the bladed mixer simulated in this work. Table 2.1 provides the corresponding values for the dimensions shown in the schematic for our base case simulations. The base dimensions were chosen to approximate a laboratory-scale bladed mixer, although other dimensions were also used to study scale up in Chapter 5 (see Section 2.1.3).

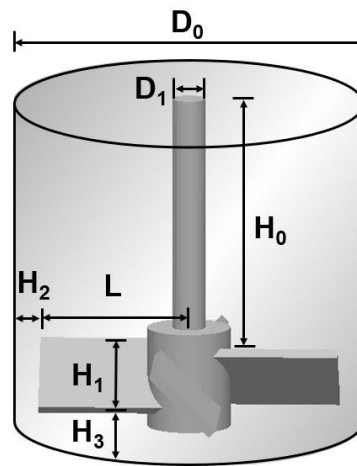


Figure 2.1: Modeling approximation of the bladed mixer system.

Table 2.1: Geometry dimension of agitated bed dryer for DEM simulations.

Parameter (units)	Symbol	Value
Vessel diameter (mm)	D_0	50
Impeller diameter (mm)	D_1	5
Blade length (mm)	L	22.5
Blade to top of vessel (mm)	H_0	102.5
Blade height (mm)	H_1	10
Blade to wall gap (mm)	H_2	2.5
Blade to bottom gap (mm)	H_3	2.5
Number of impeller blades	-	4
Impeller blade angle (degrees)	-	45
Direction of blade rotation	-	Counterclockwise

2.1.1 Flow and Contact Model

EDEM[®] enables the computation of particle dynamics by integrating Newton's laws of motion to obtain information about each particle's displacement, velocity, and resultant forces. Equations 2.1 and 2.2 describe the motion of each particle:

$$m_i \frac{dv_i}{dt} = \sum_j (F_{Nij} + F_{Tij}) + m_i g \quad (2.1)$$

$$I_i \frac{d\omega_i}{dt} = \sum_j (r_i \times F_{Tij}) + \tau_{rij} \quad (2.2)$$

where m_i is the mass of particle i , v_i is the velocity of the particle, t is time, and g is the acceleration due to gravity. F_{Nij} and F_{Tij} are the normal and tangential forces, respectively, resulting from the contact between particle i and j . In Equation 2.2, I_i , ω_i , and r_i are the moment of inertia, the angular velocity, and the radius of the particle, respectively. The stress term, τ_{rij} , is obtained from

$$\tau_{rij} = -\mu_r |F_{Nij}| r_i \omega_i \quad (2.3)$$

where μ_r is the rolling friction coefficient. The default contact model in EDEM[®] for non-cohesive material is based on Hertz-Mindlin theories [88], where colliding spheres experience a deformation related to the force of the contact. The normal component of the contact force F_N is obtained by Equation 2.4 below:

$$F_N = -\tilde{k}_n \delta_n^{3/2} - \tilde{\gamma}_n \dot{\delta}_n \delta_n^{1/4} \quad (2.4)$$

where \tilde{k}_n is the normal stiffness coefficient, δ_n is the normal displacement, and $\tilde{\gamma}_n$ is the normal damping coefficient. The normal stiffness coefficient \tilde{k}_n is given by

$$\tilde{k}_n = \frac{E \sqrt{2r_{ij}}}{3(1 - \nu^2)} \quad (2.5)$$

where E is the Young's modulus, and ν is the Poisson ratio. The effective radius of the particles in contact, denoted by r_{ij} , which is obtained from

$$r_{ij} = \frac{r_i r_j}{r_i + r_j} \quad (2.6)$$

with r_i and r_j being the radius of particle i and j , respectively. The normal damping coefficient $\tilde{\gamma}_n$ is given by Equation 2.7.

$$\tilde{\gamma}_n = \ln(e) \frac{\sqrt{m \tilde{k}_n}}{\sqrt{\ln^2 e + \pi^2}} \quad (2.7)$$

where e is the coefficient of restitution.

The tangential component of the contact force F_T is given by the following equation:

$$F_T = -\tilde{k}_t \delta_t - \tilde{\gamma}_t \dot{\delta}_t \delta_n^{1/4} \quad (2.8)$$

where \tilde{k}_t is the tangential stiffness coefficient, δ_t is the tangential displacement, and $\tilde{\gamma}_t$ is the tangential damping coefficient. The tangential stiffness coefficient is calculated from

$$\tilde{k}_t = \frac{2\sqrt{2r_{ij}G}}{2-\sigma} \delta_n^{1/2} \quad (2.9)$$

where G is the shear modulus of the particle. The value of G is assumed to be the same for all particles. The tangential displacement δ_t is described:

$$\delta_t = \int v_{rel}^t dt = \int [(v_i - v_j) * s + \omega_i r_i + \omega_j r_j] dt \quad (2.10)$$

where v_{rel}^t is the relative tangential velocity, which in turn is defined by the velocity v , radius r , and angular acceleration ω of the particles. The parameter s is the tangential decomposition of the unit vector connecting the center of the particles in contact.

EDEM[®] updates the position and velocity of each particle using a time-stepping algorithm, as shown by Equations 2.11 and 2.12.

$$x(t + \Delta t) = x(t) + v(t)\Delta t \quad (2.11)$$

$$v(t + \Delta t) = v(t) + a(t)\Delta t \quad (2.12)$$

The variable x denotes the particle position and a is the particle acceleration resulting from a time change Δt . The time step needs to be small enough to ensure numerical stability and accuracy but not so small that the computational time becomes prohibitively long. Typically, the default time step value is chosen to be 20% to 30% of the Rayleigh time [89]. The parameter values needed for the model are displayed in Table 2.2. The parameter value for the rolling friction coefficient, the sliding friction coefficient, and the coefficient of restitution were selected according to previous experimental and modeling work by Remy *et al.* [79, 90].

Table 2.2: Parameter values for DEM simulations.

Parameter (units)	Symbol	Value
Wall temperature (K)	T_w	323
Initial particle temperature (K)	T_0	298

Agitation rate (rpm)	ω	0 - 100
Total number of particles	N	5000
Mean particle diameter (m)	d	0.002
Mean particle radius (m)	r	0.001
Particle size distribution type	-	Normal
Particle size distribution standard deviation (m)	-	0.0002
Particle size distribution bounds (m)	-	0.0016 to 0.0024
Particle thermal conductivity (W/mK)	k	0.1 - 100
Wall thermal conductivity (W/mK)	k_w	30
Particle density (kg/m ³)	ρ	2200
Specific heat capacity (J/kg K)	C_p	840
Rolling friction coefficient	μ_r	0.005
Sliding friction coefficient	μ_s	0.5
Coefficient of restitution	e	0.6
Poisson ratio	ν	0.25
Elastic modulus (Pa)	E	6500000
Shear modulus (Pa)	G	2600000

2.1.2 Heat Transfer Model and Assumptions

Heat transfer in a bladed mixer system can take place in the form of conduction, convection, and radiation. In this work, only particle-particle and wall-particle conductive heat transfer was considered. Heat transfer through an interstitial fluid was not modeled. Conduction in a bed of particles is made up of two contributions: a direct mechanism or direct conduction through the contact area between the particles and an indirect mechanism or indirect conduction through the thin layer of interstitial fluid between the two particles [91]. The work presented in this dissertation serves as a first step to understanding heat transfer between the particles without the complexities of the interstitial fluid. This work therefore only models direct conduction through the contact area between the particles. While this assumption may not be valid for certain cases, this approach of isolating heat transfer between particles first may provide insight into the contributions of direct and

indirect conduction (conduction from one particle to the fluid to another particle). In addition, a wide range of thermal conductivities have been studied to try to capture cases where the overall heat transfer is larger than would be due to direct conduction. Furthermore, the hope is that like in classical heat transfer, further work on direct and indirect conduction will lead to values for lumped, average, or effective thermal conductivities or heat transfer coefficients that can be used in a dry particle simulation.

In this system, heat was supplied from the vessel wall/bottom, which was assumed to remain at a constant temperature value of T_w (Table 2.2). Heat losses to the outside environment were not considered. The contribution of radiation to the overall heat transfer would become significant only if the processing temperatures were much higher than those generally used in the pharmaceutical industry, so it was deemed negligible [43]. For those reasons, particle-particle conduction and wall-particle conduction were assumed to be the dominant modes of heat transfer in our system. Particle-to-particle conduction ensues when two particles of unequal temperatures collide and exchange energy through the surface area in contact. The heat flux Q_{ij} exchanged by two particles i and j is [8]:

$$Q_{ij} = H_{cij}(T_j - T_i) \quad (2.13)$$

where T_i and T_j denote the temperature of each particle and H_{cij} is the heat conductance between them. Batchelor *et al.* [92] defined the conductance between two touching particles with a circular contact area as:

$$H_{cij} = 2k_{ij}a_{ij} \quad (2.14)$$

where the conductance is a function of the effective particle thermal conductivity, k_{ij} , and the contact radius, a_{ij} , between particles i and j . The effective particle thermal conductivity is obtained from

$$k_{ij} = \frac{2 * k_i k_j}{(k_i + k_j)} \quad (2.15)$$

where k_i and k_j are the thermal conductivities of particles i and j , respectively. In this work, we assume that all particles had the same conductivity, such that $k_i = k_j = k$.

The contact radius is given by

$$a_{ij} = \sqrt[3]{\frac{3F_{Nij}r_{ij}}{4E_{ij}}} \quad (2.16)$$

where F_{Nij} is the normal force as defined by Equation 2.4, r_{ij} is the geometric mean of the particles radii as defined by Equation 2.6, and E_{ij} is the effective Young's modulus obtained from

$$E_{ij} = \frac{2 * E_i E_j}{(E_i + E_j)} \quad (2.17)$$

where E_i and E_j are the Young's modulus of particles i and j , respectively. In this work, the Young's modulus is assumed to be the same for all particles, such that $E_i = E_j = E$.

Figure 2.2 illustrates the contact radius between two spherical particles.

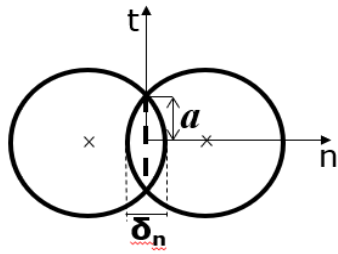


Figure 2.2: Particle collision with contact radius a and normal overlap δ_n .

The temperature evolution of particle i is given by:

$$\frac{dT_i}{dt} = \sum_j^{N_i} \frac{Q_{ij}}{\rho_i V_i C_{pi}} \quad (2.18)$$

where Q_{ij} is the heat flux exchanged from each contact, N_i is the number of touching neighboring particles, ρ_i is the particle density, V_i is the particle volume, and C_{pi} is the specific heat capacity.

The equations for the heat flux between a particle and a wall, Q_{iw} , can be defined as [93]:

$$Q_{iw} = \frac{4a(T_w - T_i)}{\frac{1}{k_i} + \frac{1}{k_w}} \quad (2.19)$$

where T_w is the temperature of the wall and k_w is the thermal conductivity of the wall. The temperature evolution of particle i is given by:

$$\frac{dT_i}{dt} = \frac{Q_{iw}}{\rho_i V_i C_{pi}} \quad (2.20)$$

The heat transfer equations were added to EDEM[®] to allow for both the position and temperature of particles to be tracked with time. Relevant parameter values for our base case material (glass beads) are included in Table 2.2 in Section 2.1.1.

The particles studied in this series of simulations were assumed to be perfectly spherical and have the same physical properties, such that the thermal conductivity $k_{ij} = k$, Young's modulus $E_{ij} = E$, density $\rho_i = \rho$, and specific heat capacity $C_{pi} = C_p$. Overall, the chosen parameter values for our base case are consistent with the properties of glass beads. The Young's modulus used in the DEM model was lower than that of real glass beads to decrease the computational time, although the resulting percent overlap between particles were found to be small relative to the radius of the particles. Previous work has shown that modifying the Young's modulus has a negligible impact on flow patterns, velocity profiles, and interparticle shear stresses for non-cohesive particles [48]. For heat

transfer, the dependence between the contact overlap and the Young's modulus likely influences the heat conductance H_c . However, because heat conductance also encompasses the thermal conductivity (Equation 2.14), it can be assumed that testing a wide range of thermal conductivities in this work effectively approximates cases for soft and hard particles in terms of effective heat transfer. Morris *et al.* [94] describe a good solution for dealing with the artificial softening where they propose to apply time- and area-corrective approaches to compensate for the greater contact area and time induced by artificial particle softening and thereby remove the impact it has on conductive heat transfer.

Particle sizes were chosen to have a normal distribution with truncated bounds to avoid abnormally large or fine particles (see Table 2.2). Initially, monodisperse particles were simulated, but it was found that the scenario without agitation resulted in crystalline packing, leading to voids in the bed and unrealistic heating of isolated particles in contact with the walls. A similar phenomenon was observed by Emady *et al.* [43], where agitation of monodisperse particles in a rotary drum led to unexpected flow patterns due to the packing. Based on this, some polydispersity was incorporated into the system, which is also more representative of typical industrial pharmaceutical materials. The mean radius of the particles was selected to be small enough to obtain an adequate number of particles in the bed while also ensuring that the computation time would not be prohibitively long. When modeling a shallow bed, the fill height of the bed covered the blades of the impeller. The work in Chapter 3 simulated a relatively small number of particles in order to be able to carry out many simulations to investigate a wide range of thermal properties and agitation rates.

The aim of Chapter 3 was to analyze and quantify the effect of agitation rate and thermal properties on heat transfer. Agitation rates ranging from 0 rpm to 100 rpm were investigated. Although agitations rates of 100 rpm may seem fast, it is necessary to note that scaling blade tip speed may be more relevant than scaling impeller rotation rate. For a small geometry scale such as the one used here, particles mixed at 100 rpm can experience tip speeds comparable to those mixed with slower rotation rates at large manufacturing scale. In terms of studying the thermal properties, Equations 2.13, 2.14, and 2.18 suggest that heat transfer is governed by the ratio $\frac{k}{\rho C_p}$ and that doubling the conductivity or halving the specific heat capacity should be the same [43]. Simulations were run to confirm this, so this work therefore focuses on varying k . The thermal conductivities k that were studied ranged from 0.1 W/mK to 100 W/mK. For comparison purposes, the solid conductivities of wheat flour, glass, stainless steel, and zinc are 0.45 W/mK, 1 W/mK, 16 W/mK, and 116 W/mK respectively [95]. In Chapter 4, we discuss experimental validation of the simulations presented in Chapter 3.

2.1.3 Modeling Scale Up

Chapter 5 investigates how scale up influences heat transfer through dry cohesionless granular material in a bladed mixer. More specifically, the H/D and D/d ratios were varied to analyze the influence on the rate of heat transfer in the bed. The H/D ratio refers to the material fill height in the bed H divided by the diameter of the vessel D . The D/d ratio represents the diameter of the vessel divided by the average particle diameter d . These ratios are common metrics when considering the scale up of a process in a cylindrical vessel [78]. In agitated filter dryers, the H/D ratio is known to be a

particularly important scaling relationship, as increasing the fill level of the bed increases the hydrostatic pressure and can affect the rate of particle attrition [62, 70]. The D/d ratio is a common scaling ratio that changes when comparing results for a material obtained from laboratory-scale equipment versus pilot-scale or manufacturing-scale equipment.

In the simulations investigating the H/D ratio, the fill level of material was varied by changing the number of particles in the system, while keeping the vessel diameter constant. The vessel diameter was that of a laboratory-scale mixer (Table 2.1). The range of fill heights studied was 2.1 cm (shallow bed with just enough material to cover the impeller blades) to 14.5 cm (deep bed), leading to H/D ratios ranging from 0.42 to 2.91. In the simulations investigating the influence of the D/d ratio, we carried out a linear scale up of the system where all dimensions were increased while the particle diameter was kept constant. The vessel diameters studied ranged from 5.0 cm to 12.5 cm, leading to D/d ratios ranging from 25.0 to 62.5. The vessel dimensions listed in Table 2.1 represent the smallest vessel we tested, which describe a laboratory-scale vessel with a D/d ratio of 25.0. The larger vessels we simulated were linear scale ups of the laboratory-scale vessel. More specifically, the dimensions of the vessels with $D/d = 37.5, 50.0$ and 62.5 had 1.5x, 2.0x, and 2.5x times the dimensions of the small vessel in Table 2.1. The only dimension parameter that was kept constant across the different vessels was H_2 , which is the size of the gap below the impeller blades. This method of studying scale up using the D/d ratio in a bladed mixer is consistent with previous work carried out by Remy *et al.* [78]. Studying larger vessels to model manufacturing scale systems, while of interest, was too computationally expensive for current resources. The number of particles in the model varied from 4,500 to 78,050 depending on the fill height and the

vessel size simulated. The parameter values for the material modeled in these simulations are listed in Table 2.2 above.

2.2 Experimental Methods

Experiments using a laboratory-scale agitated bed dryer were conducted to better understand how operating conditions influence the rate of heat transfer in a bed of particles. Additionally, the experimental results served to validate the numerical model described in Section 2.1. Most of the equipment used in this work was provided by a pharmaceutical company as part of an ongoing research collaboration.

2.2.1 Experimental Setup

The experimental setup is shown in Figure 2.3 and Figure 2.4 below. The equipment includes a Chemglass[®] cylindrical glass vessel with a heating jacket, an 80/20[®] aluminum frame, a stainless steel impeller shaft with 2 blades, a Maxon[®] motor, a Huber[®] circulator, a thermocouple, and a Red Lion[™] Human Machine Interface (HMI). The glass vessel has an internal diameter of 52 mm and a height of 170 mm. The impeller shaft has a width of 12.5 mm. The two blades have a total length of 45 mm, a height of 15 mm, and an angle of 60°. The clearance between the bottom of the vessel and the bottom of the blades is 10 mm. The frame stand holds the motor in place and permits adjustment of the motor in 3D above the vessel. The impeller shaft was connected to the motor using a rigid coupling to prevent the impeller from wobbling and accidentally hitting the vessel walls. The circulator heats liquid in a bath and circulates it to the vessel's heating jacket via insulated pipes. The fluid inside the circulator was deionized

water with a few drops of algaecide from PolyScience® to prevent microbial growth inside the circulator and the heating jacket. The HMI serves as an equipment controller and a data recorder. It is programmed to control the motor speed, set the circulator temperature, and record the temperature data from the thermocouple.

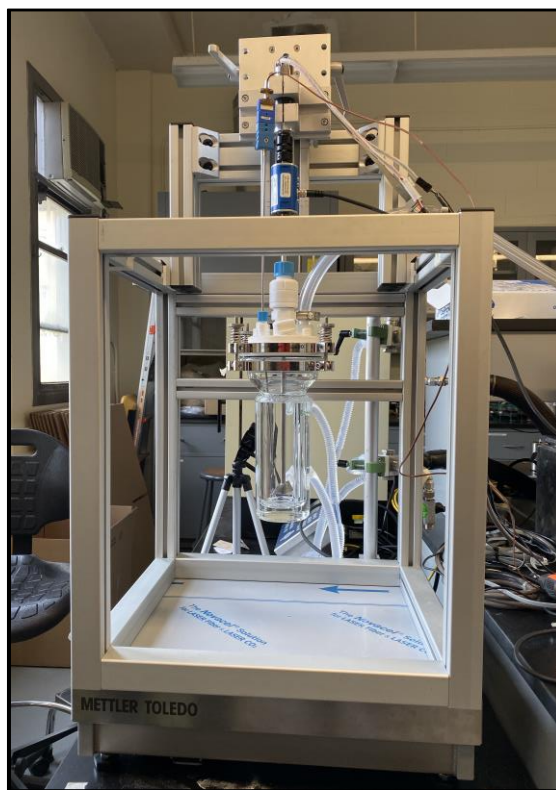


Figure 2.3: Experimental setup of the agitated dryer system. The image shows the cylindrical vessel with the heating jacket, the impeller, the motor, and the aluminum stand.



Figure 2.4: Overview of the experimental setup. The image shows the agitated dryer system, the HMI, and the circulator.

The material used in the experiments was dry spherical soda-lime glass beads from Mo-Sci[®] (GL0191). Glass beads are often used as a model for granular materials since they can exhibit flow behaviors similar to pharmaceutical powders. Figure 2.5a and Figure 2.5b depict images of the glass beads taken using a regular camera and an optical microscope, respectively. Overall, the beads are relatively smooth and cohesionless. The material properties of the glass beads and the operating conditions are provided in Table 2.3. The material specifications were provided by the supplier. The material used in the experiments was as-received.

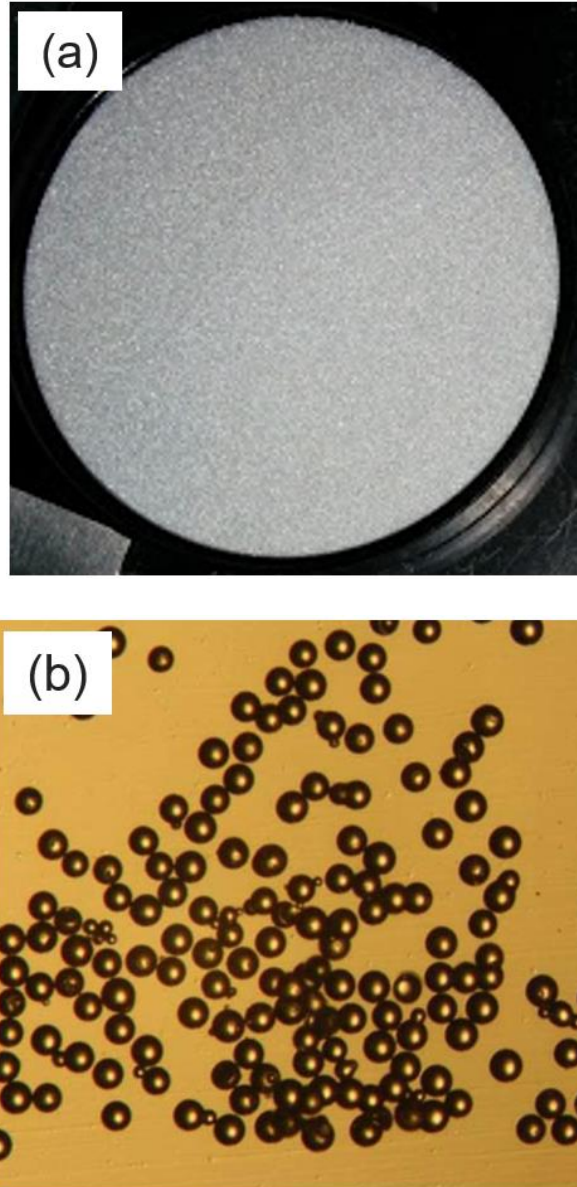


Figure 2.5: (a) Glass beads used in the heating experiments. (b) Optical microscope image of the glass beads. Image credit: James Scicolone.

Table 2.3: Material properties of the glass beads and operating conditions.

Parameter (units)	Symbol	Value
Mean particle diameter (mm)	d	0.1
Particle size range (mm)	-	0.09 - 0.106
Particle density (kg/m^3)	ρ	2500

Bulk density (kg/m ³)	ρ_{bulk}	1423
Jacket temperature (K)	T_w	323
Agitation rate (rpm)	ω	0, 5, 10, 25, 100
Material fill height (mm)	H	35
Bed mass (kg)	M_b	0.106

Temperature was measured in two ways during the experiment: with thermocouples and with infrared imaging. One thermocouple was used to record the starting temperature of the beads before each experiment while another was used to measure the room temperature during the experiment. The bed surface temperature was measured using an infrared camera that was positioned above the vessel. Infrared measurements were carried out using a FLIR® C3 camera with 80x60 thermal resolution. Figure 2.6a and Figure 2.6b show the experimental setup for the infrared camera.

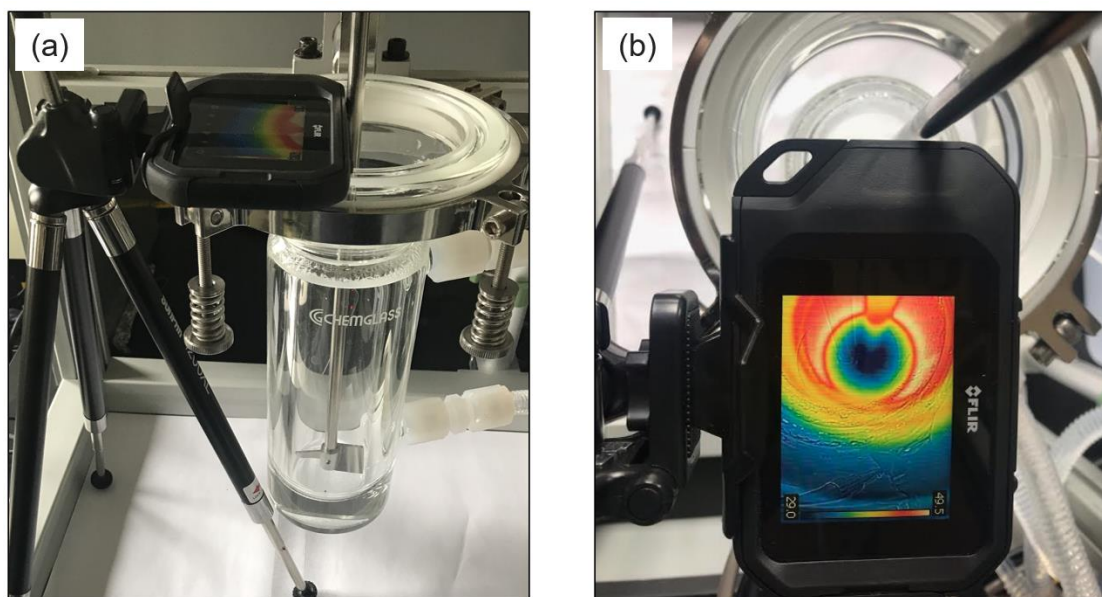


Figure 2.6: (a) Side view and (b) top view of the experimental setup with the laboratory-scale agitated dryer and the infrared camera.

2.2.2 Experimental Procedure

First, the vessel was secured to the frame using a clamp and the assembly was leveled with a bubble level. A set mass of glass beads was weighed and was placed into a beaker until the start of the experiment. A thermocouple was inserted into the beaker to measure the initial temperature of the glass beads. The temperature of the circulator was set to 50°C using the HMI. The impeller was connected to the motor using the bearing. The positioning of the motor and the impeller were adjusted such that there was a 1 cm gap between the bottom of the blades and the bottom of the vessel. The infrared camera was attached to the tripod and was placed in a marked position where the entire surface of the bed could be viewed from the top. The motor rotation was set to the desired agitation rate using the HMI. When the setup of the experiment was ready, the beads were carefully poured inside the vessel and the HMI started to log data from the motor, the circulator, and the thermocouple. The infrared camera captured an image of the bed surface every 1-minute for the duration of the experiment. Each experiment was carried out for 40 minutes. At the end, the HMI data logging was stopped, the motor was turned off, and the circulator heating was shut off. The vessel was disassembled from the frame, and the beads were emptied out into a separate container. The vessel was cleaned with a vacuum to remove any remaining particles. The data from the HMI were extracted using a USB stick. The images from the infrared camera were uploaded onto a computer.

The goal of the experiments was to evaluate the effect of the impeller agitation rate on the rate of heat transfer in the agitated dryer as well as the heating uniformity. Experiments were conducted for five different agitation rates: 0 rpm (i.e.: no agitation), 5 rpm, 10 rpm, 25 rpm, and 100 rpm. Each experiment was done three times, generally

back-to-back. Before starting a new experiment, the impeller was left to cool down until it returned to room temperature. The reason for this is because we had found during preliminary experiments that the initial temperature of the impeller significantly influenced the results. By allowing the impeller to start at room temperature each time, it allowed us to remove a variable that could have introduced experimental error into the results. Similarly, a new batch of glass beads was used for each experiment to ensure that the material started at room temperature each time. The temperature of the laboratory varied from day-to-day, so we made sure to record the room temperature for each experiment.

2.2.3 Analytical Procedure

The infrared images were analyzed using the software FLIR ResearchIR. Each pixel in the image has an associated temperature measurement. In this work, we were only interested in collecting information about the bed surface. Other regions of the image (i.e.: the edge of the vessel and the lab bench as shown in Figure 2.6b) were not of interest. The first step of the analysis was therefore to extract the temperature data of the bed surface and to crop out the rest of the image. The software allows the user to draw a “region of interest” (ROI) on the image and export data for that region. After selecting the ROI, the temperature data for each pixel in the ROI were exported as a .csv file and MATLAB[®] was used to compute the mean temperature and the standard deviation of the bed surface. The procedure was repeated for each image (i.e.: each time point) for all experiments.

Initially, we drew a circular ROI on the surface of the bed around the particle bed to perform our analysis. The circle also included part of the impeller shaft. Unfortunately, we noticed that the impeller shaft did not always have the same temperature as the bed and that it could affect the results. Removing the impeller shaft from each image is time-intensive so we sought to quantify the extent to which the shaft influenced the results. We selected images from a case where the impeller shaft was particularly prominent (trial 1, 25 rpm agitation rate) and carried out our analysis for a circular ROI with the impeller and a polygon ROI without the impeller. The circular and polygon ROIs are illustrated in Figure 2.7a. Figure 2.7a and Figure 2.7b show the influence of the shaft temperature on the mean temperature and the standard deviation of the bed surface over time, respectively. We see in Figure 2.7a that the effect of the impeller shaft on the mean temperature results of the ROI is relatively negligible. Overall, the mean temperature of the ROI with the impeller is slightly lower than when the impeller is removed. However, the difference between the circular ROI and the polygon ROI in this analysis is fairly minor. By contrast, we observe in Figure 2.7b that the impeller shaft strongly influences the results for the temperature standard deviation. We see that the standard deviation for the ROI with the impeller is considerably higher than the ROI without the impeller throughout the heating process.

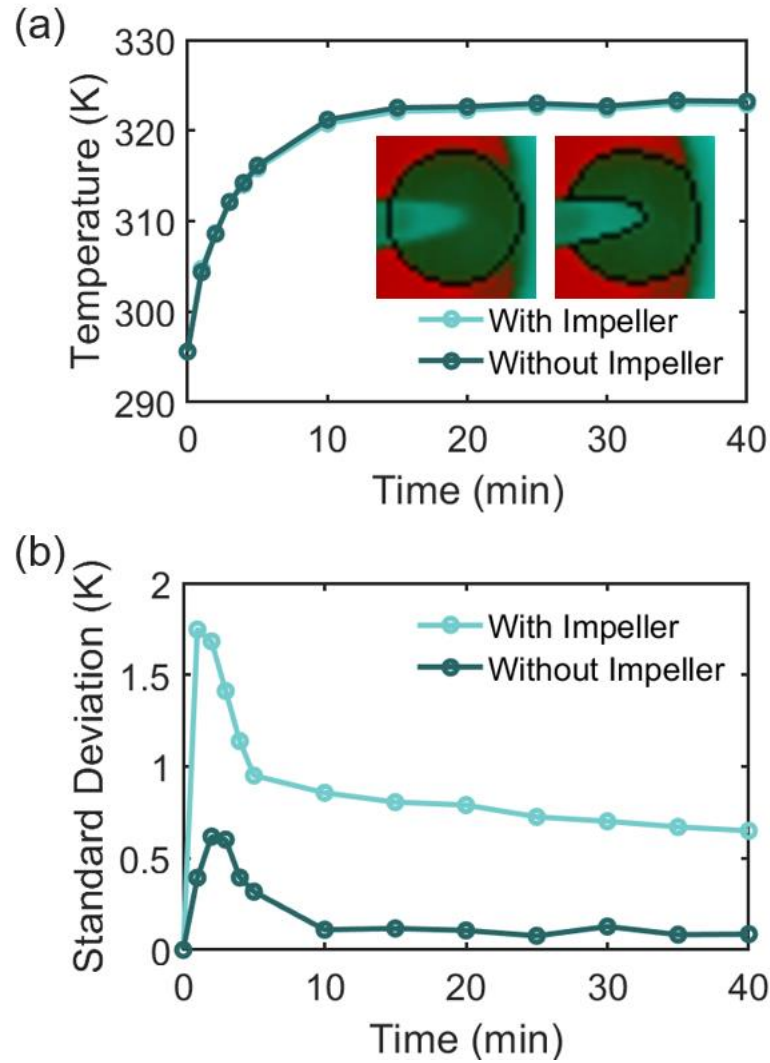


Figure 2.7: Effect of removing the contribution of the impeller on (a) the mean temperature of the surface, (b) the standard deviation of the surface.

Upon seeing the results from Figure 2.7b, we decided to proceed with removing the impeller shaft from all the images for each experiment to minimize error in the results for the bed uniformity. The mean temperature and the standard deviation of the bed surface were calculated for each experiment for each agitation rate. Heating times and heat transfer coefficients were also computed for each condition. The results are presented in Chapter 4.

3. EFFECT OF THERMAL PROPERTIES AND AGITATION RATE ON HEAT TRANSFER

In this chapter, DEM simulations were used to learn more about how heat transfer occurs in dry granular material in a bladed mixer both visually and quantitatively. Two important parameters were varied in the simulations: the agitation rate of the impeller and the material thermal conductivity. The agitation rate of the impeller is an essential parameter to optimize during the design of drying protocols because it helps promote heat transfer by bringing cold and hot particles together and enhancing the temperature uniformity of the bed. However, strong shear forces due to excessive agitation can induce particle breakage which is typically undesirable. It is therefore important to understand how heat transfer is influenced by agitation so that the impeller speed can be chosen carefully. The thermal properties of the material are important because each API is different and has unique thermal properties. Understanding the influence of the thermal properties helps shed light on how the heating process differs for different materials. This chapter provides an in-depth analysis of the effect of mixing and material thermal properties on heat transfer in the bed. First, the mean temperature of the bed is computed over time for different thermal conductivities and agitation rates. Next, the heat transfer coefficients are computed for each scenario. A dimensional analysis is carried out to define relevant dimensionless groups and nondimensionalize the results. Next, the effect of conductivity and agitation on the distribution of temperatures in the bed is investigated. Finally, the implications of these results are discussed.

3.1 Visualizing Heat Transfer

A significant advantage of the DEM simulations is that they provide the ability to track particles in the bed and visualize how their temperature evolves over time. Figure 3.1 depicts the temperature of particles in the bed at different time points for the condition $k = 10 \text{ W/mK}$ and $\omega = 10 \text{ rpm}$. The vessel side walls and base were both kept at a constant temperature T_w . At the start of the simulation, the bed had an initial temperature of T_0 . Figure 3.1 shows some fairly typical results in terms of heat transfer in the system. One can see that the particles at the bottom of the bed heat up faster than the particles near the side walls (see Figure 3.1 at 25s). The reason for this is that the gap between the blades and the bottom of the cylinder wall is larger than the mean particle diameter. As a result, there is a layer of particles which is fairly stationary at the bottom of the bed and while this layer does mix with the rest of the bed, it spends more time in contact with the wall and heats up quickly due to contact with the hot base of the cylinder. This creates a vertical temperature gradient; at 25 s the particles at the base of the cylinder have almost reached the wall temperature, while particles on the surface are still at the initial temperature. As time progresses, particles in direct contact with the side walls and base of the cylinder reach the wall temperature (see Figure 3.1 at 100 s) and then transfer their heat to neighboring particles until the entire bed content approaches the vessel wall temperature (see Figure 3.1 at 200s).

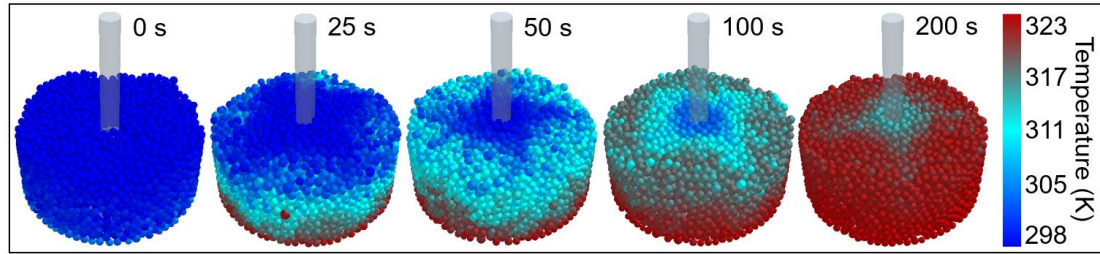


Figure 3.1: Particles heating over time for $k = 10$ W/mK and $\omega = 10$ rpm. Particles start at room temperature (298 K) and are heated by the walls at a temperature of 323 K.

Figure 3.2 captures the influence of agitation rate and thermal conductivity on particle temperatures. Figure 3.2a shows beds with identical thermal conductivity but differing agitation rates at the same point in time. The figure illustrates that higher agitation rates resulted in a better distribution of heat throughout the bed, as shown by increasingly more uniform temperature gradients.

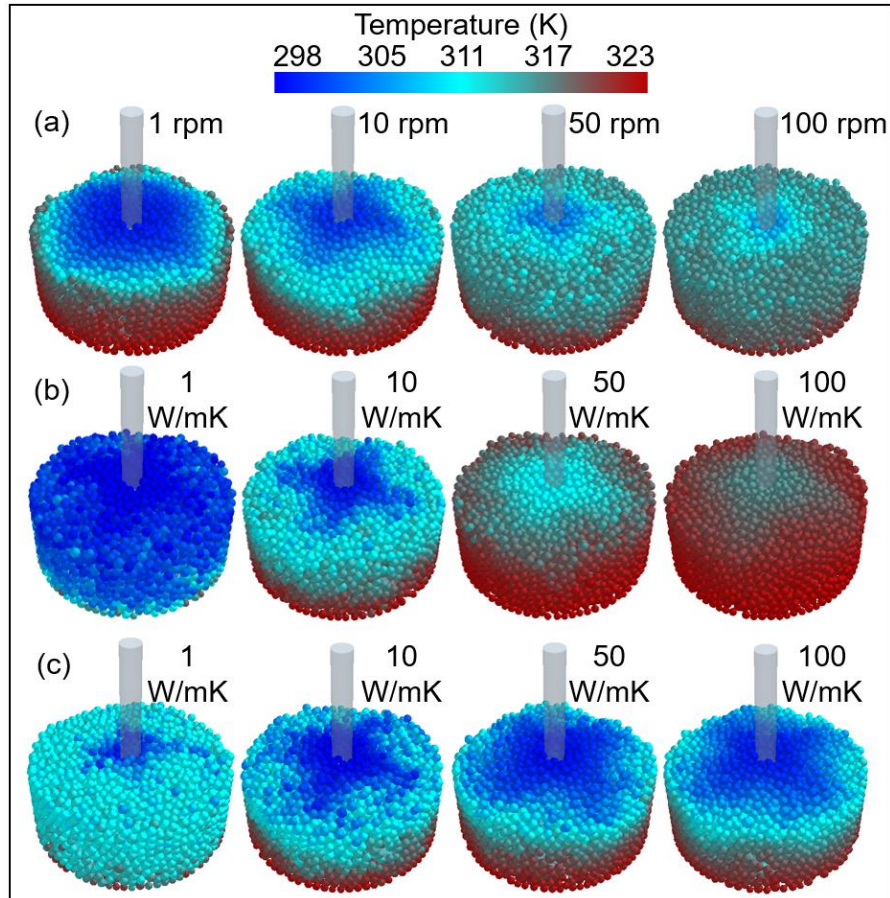


Figure 3.2: (a) Effect of agitation rate for the same thermal conductivity $k = 50$ W/mK when time $t = 30$ s. (b) Effect of thermal conductivity for the same agitation rate $\omega = 10$ rpm when time $t = 60$ s. (c) Effect of thermal conductivity for the same agitation rate.

On the other end, slower agitating led to longer contact times for particles at the hot wall, creating a more significant temperature gradient between the particles near the wall and those near the center. For the lowest agitation rate (see Figure 3.2a, 1 rpm) the bed heats up in a similar way to how a stationary (non-agitated) bed would heat up, with an annular temperature gradient. Another observation was the appearance of a cross shaped cooler core for higher agitation rates (see Figure 3.2a, 10 rpm), which can likely be

attributed to the shape of the four angled impeller blades lifting warm particles from the heated bottom of the vessel to the colder surface of the bed.

Figure 3.2b depicts temperatures for particles with different thermal conductivities mixed at the same agitation rate at the same point in time. As expected, it illustrates that beds with a higher conductivity approach the wall temperature more rapidly. Since beds with high thermal conductivities heat up much more rapidly than those with low conductivity, it is also interesting to compare the beds at times when they are at the same temperature. Figure 3.2c compares beds with different conductivities mixed at the same agitation rate when they reach a mean bed temperature of $\bar{T}_b = \frac{(T_w - T_0)}{2}$. As can be seen in Figure 3.2c, for the cases with lower thermal conductivity, although heating occurred more slowly, the material heated more uniformly. As k was increased, the bed was heated more rapidly but with a more significant temperature gradient. While Figure 3.2c only captures this phenomenon for a single point in time, it was observed for all times. The influence of thermal conductivity and agitation rate on heating uniformity will be further discussed later in Section 3.4 when the results on temperature distributions are reported. The results in Section 3.2 and Section 3.3 focus on analyzing the mean temperature of the bed.

3.2 Effect on the Rate of Heat Transfer

The objective for these simulations is to not only understand general trends of the relationship between agitation rate, conductivity, and heat transfer but also to quantify these trends. For example, does doubling the agitation rate double the rate of heat transfer through the bed? The answer to this question is not necessarily trivial for granular materials. Thus, it is important to quantify the relationship. As a first step to answering this

question, Figure 3.3 provides a quantitative visualization of Figures 3.2a and 3.2b by plotting the mean temperature of the bed as a function of time for various thermal conductivities and agitation rates. Because of the slight polydispersity present in the bed, the mean temperature calculated at each time step was a particle-mass average. Once again, it can be observed that the beds with poorly conductive material (see Figure 3.3a) heated up more slowly than beds with higher thermal conductivity (see Figure 3.3b), as the mean bed temperature approached the temperature of the wall in less time. In Figure 3.3a, we notice that for a material with poor thermal conductivity, agitating at slow speeds drastically improves the heat transfer since increasing the agitation rate from 1 rpm to 2 rpm and to 5 rpm leads to a significant increase in the rate of heat transfer. Further increasing the agitation speed to 10 rpm and then 100 rpm does not lead to a significant increase in the rate of heat transfer. In fact, the results for 10 rpm and 100 rpm almost lie on top of one another (see Figure 3.3a). However, in Figure 3.3b we see that for $k = 100$ W/mK, there is very little difference between the results for 1, 2, and 5 rpm, and it is only when we increase the rate of agitation to 10 rpm and then 100 rpm that we start to see differences between the rates of heat transfer.

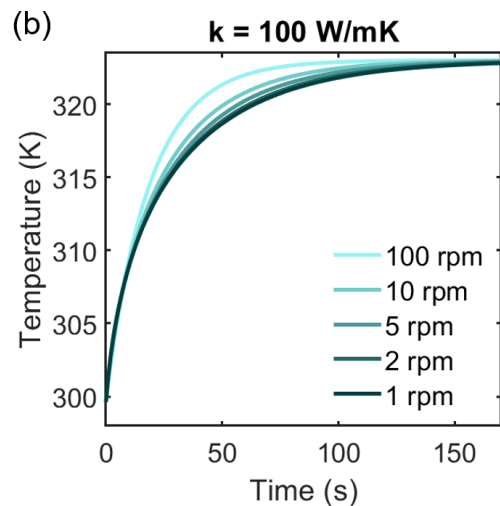
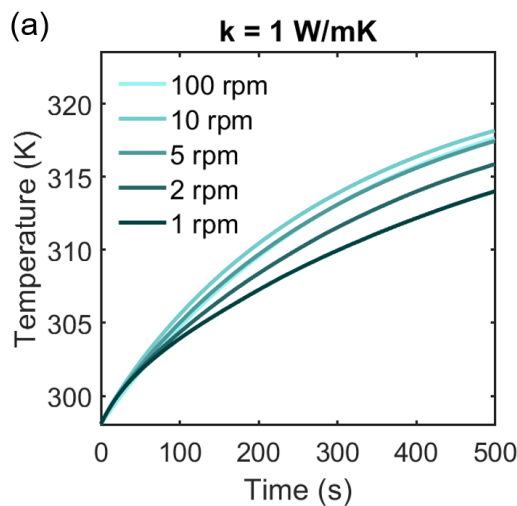


Figure 3.3: Mean temperature of the bed over time as a function of agitation rate and conductivity, where (a) $k = 1$ W/mK, (b) $k = 100$ W/mK.

When studying a wide range of thermal conductivities, it is difficult to visualize and interpret the results in terms of time because a material with a conductivity $k = 100$ W/mK heats up much more rapidly than a material with $k = 1$ W/mK. Therefore, we introduced a normalized time, τ_b , the thermal time scale for the bed, in order to allow for an easier comparison of the different scenarios, as described by Emady *et al.* [43] for heat transfer in a rotary drum. This time scale was obtained by considering an energy balance on a bed of particles in a rotary drum. We can create a similar heat balance for our system by relating the increase in mean temperature of the bed to the heat transfer from the cylinder to the particles:

$$M_b C_p \frac{d\bar{T}_b}{dt} = h_{eff} A_b (T_w - \bar{T}_b) \quad (3.1)$$

where T_w is the wall temperature, \bar{T}_b is the mean bed temperature, M_b is the mass of the bed, A_b is the surface area of the bed available for heat transfer, i.e., the surface area (of the walls of the cylinder) that is in contact with the bed of particles (which includes the cylinder base and vertical walls), h_{eff} is the effective heat transfer coefficient between the cylinder and the bed of particles, and C_p is the specific heat capacity of the bed of particles. The energy balance (Equation 3.1) can be integrated with the initial condition at $t = 0$, $\bar{T}_b = \bar{T}_{b,0}$ to obtain the following equation:

$$\ln \left(\frac{T_w - \bar{T}_b}{T_w - \bar{T}_{b,0}} \right) = - \frac{h_{eff} A_b}{M_b C_p} t = - \frac{t}{\tau_b} \quad (3.2)$$

The bulk properties can be lumped into a parameter, τ_b which we define as the thermal time of the bed, and it relates to the time needed to heat the entire bed of particles.

More specifically, it is the time required for the difference between the mean temperature of the bed and the wall temperature to drop by 63.2% of the initial difference, i.e., at $t = \tau_b$ the difference between the mean bed temperature and the wall temperature is 36.8% of the difference between the initial bed temperature and the wall temperature.

In Figure 3.4, we demonstrate that a straight line is obtained if the natural logarithm of $\frac{T_w - \bar{T}_b}{T_w - \bar{T}_{b,0}}$ is plotted versus time. Consequently, τ_b can be obtained for each simulation by calculating the negative inverse of the slope. Example simulations are shown for the conditions $\omega = 100$ rpm, $k = 50$ W/mK (dark green) and $\omega = 25$ rpm, $k = 10$ W/mK (light blue). The higher the value of τ_b , the longer the bed temperature takes to approach the wall temperature.

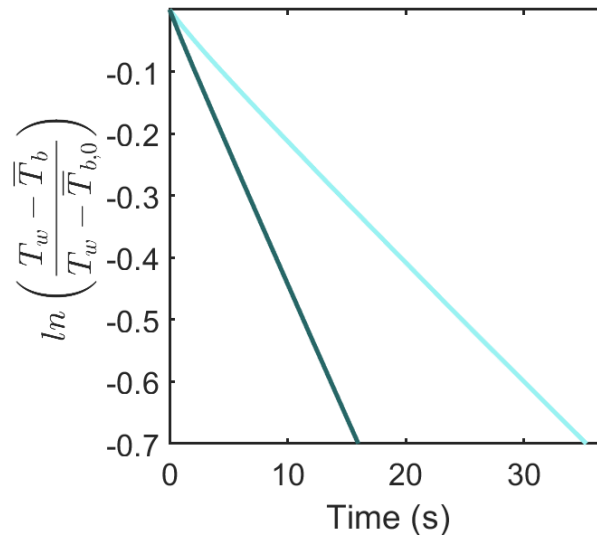


Figure 3.4: Natural logarithm of dimensionless temperature driving force over time for the conditions $\omega = 100$ rpm, $k = 50$ W/mK (dark green) and $\omega = 25$ rpm, $k = 10$ W/mK (light blue).

A common metric for interpreting results from a heating experiment is the heat transfer coefficient. The effective heat transfer coefficient illustrates how well heat is

transferred between the wall and the bed. When looking at the energy balance between the wall and the bed (Equation 3.2), we see that the effective heat transfer coefficient, denoted as h_{eff} , is related to τ_b by:

$$h_{eff} = \frac{M_b C_p}{\tau_b A_b} \quad (3.3)$$

Each temperature profile displayed in Figure 3.3 can be summarized by a single τ_b . Figure 3.5a and 3.5b show the τ_b calculated for each condition and the corresponding h_{eff} , respectively. The heat transfer coefficient is traditionally the more common value to analyze in heat transfer studies. Since τ_b is inversely proportional to h_{eff} , the trends observed in Figure 3.5a are simply the reversal of those depicted in the h_{eff} plot (Figure 3.5b). For $k = 1$ W/mK, the heat transfer coefficient initially increases with agitation rate and then plateaus around an agitation rate of 10 rpm (see Figure 3.5b). For $k = 10$ W/mK, the heat transfer coefficient also initially increases with agitation rate, but it plateaus around an agitation rate of 20 rpm. For higher thermal conductivities, the heat transfer coefficient has not yet reached a plateau at 100 rpm, but its rate of increase is considerably less between 80 and 100 rpm than between 20 and 40 rpm. These plots facilitate quantifying of the relationship between k , ω , and heat transfer. For example, when the agitation rate was doubled from 1 to 2 rpm, the heat transfer coefficient for $k = 1$ W/mK increased by 26%. However, for $k = 100$ W/mK when the agitation rate was doubled from 1 to 2 rpm, the heat transfer coefficient only increased by 4%. When the agitation rate was doubled from 25 to 50 rpm, h_{eff} for $k = 1$ and for $k = 100$ W/mK increased by 0% and by 15%, respectively. It can be concluded from these results that the extent to which the agitation rate contributes to the heat transfer depends on the conductivity of the material.

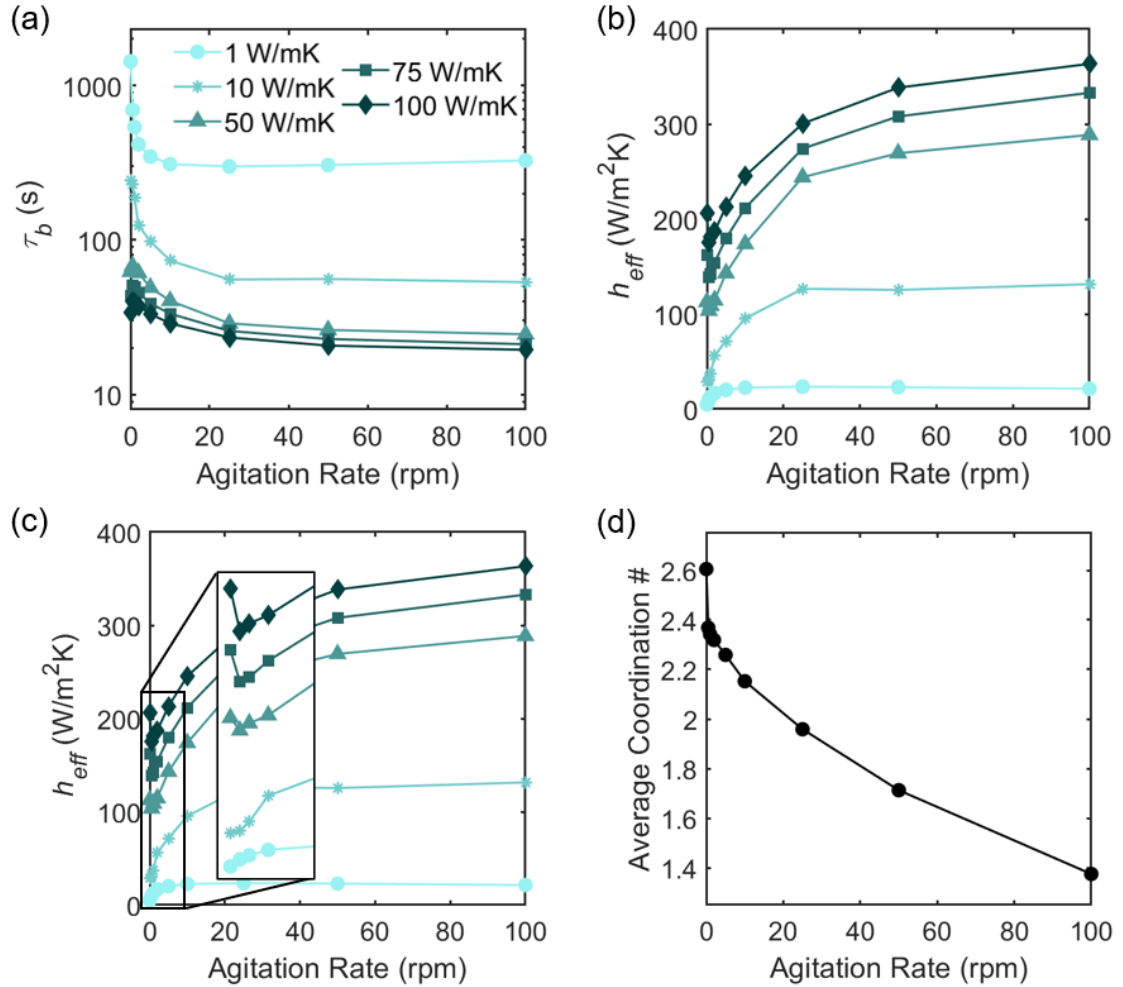


Figure 3.5: (a) Thermal time τ_b as a function of agitation rate for varying conductivity. (b) Effective heat transfer coefficient h_{eff} as a function of agitation rate for varying conductivity. (c) Blow-up of heat transfer coefficient for slow agitation rates. (d) Average coordination number as a function of agitation rate. The legend in Figure 3.5a also applies to Figure 3.5b and 3.5c.

For particle conductivities below $k = 50$ W/mK, the heat transfer coefficient was found to increase at slow agitation rates but plateau for faster agitation speeds. This result can prove to be particularly useful in agitated drying applications where attrition is a common challenge. Fast agitation rates tend to be associated with an increased risk of

attrition, and so minimizing the agitation rate while maintaining adequate heat transfer can be an important concern. In this bladed mixer system, we see that for a material with a thermal conductivity of 1 W/mK (similar to many APIs), heat transfer greatly improved when increasing agitation rate from 0 to 5 rpm but then improved marginally for agitation rates beyond 5 rpm. In a real experiment with an API with similar thermal properties, these results could be leveraged as a starting point to determine the slowest agitation rate needed to minimize attrition while optimizing heat transfer.

Figure 3.5c provides a closer look at a phenomenon that occurs at low agitation rates for materials with high conductivities. Unexpectedly, a dip in the heat transfer coefficient can be observed at agitation rates less than 1 rpm for materials with conductivities greater than 50 W/mK. It should be noted that conductivities above 10 W/mK are rather high for pharmaceutical materials, and therefore, this result is more of academic interest. A potential explanation for this phenomenon involves the coordination number. The coordination number is the number of touching neighbors for a particle. We see from Equation 2.18 in Chapter 2 that the higher the coordination number, the more contacts a particle has, and therefore, the more conduction occurs. The agitation rate can influence the coordination number because it affects particle positioning, contacts, and voids within the bed. The average coordination number for each agitation rate was obtained once the system has reached steady state by dividing the total number of particle contacts by the number of particles. Figure 3.5d shows the average coordination number as a function of agitation rate. The results indicate that the average coordination number decreased with increasing agitation rate. Since bed dilation is a common phenomenon that

is a prerequisite for shearing [96], apparently the bed dilates, and the additional voids in the bed explain the decreased number of particle contacts.

Interestingly, Figure 3.5d indicates that a sharp drop in the coordination number occurred between agitations rates of 0 and 0.5 rpm. It can be hypothesized that the drop observed in h_{eff} between 0 and 0.5 rpm for $k > 50$ W/mK may be related to the drop observed in the coordination number. Mixing the bed may affect the balance between heat transfer occurring through conduction (direct contact) and through convection (particles mixing and bringing their energy with them). Convection here does not describe heat transfer through an interstitial fluid, as this factor has been neglected in the model, but rather refers to “granular” convection. Granular convection is the process by which shearing leads to particles moving around the bed and transferring energy through movement [87]. As agitation increases, heat transfer occurring through convection increases. At the same time as agitation increases and the bed dilates, heat transfer occurring through conduction decreases. When thermal conductivity is low (in this case when $k \leq 10$ W/mK), heat transfer through conduction is relatively poor so any heat transfer provided via granular convection will increase h_{eff} . We therefore do not see a dip in heat transfer coefficient in Figure 3.5c. When thermal conductivity is high ($k \geq 50$ W/mK), heat transfer through conduction dominates, and consequently, a sharp decrease in coordination number will substantially decrease conduction and will lower h_{eff} ; we therefore do see a dip in h_{eff} between 0 and 0.5 rpm in Figure 3.5c. As the agitation rate is further increased, heat transfer occurring via granular convection becomes more significant and overall improves h_{eff} . The effect of agitation rate on heat transfer in a

bladed mixer therefore appears to be nontrivial as it affects the balance between conduction and granular convection. The interplay between granular convection and conduction in a sheared bed of particles has also been studied by Rognon *et al.* [87] using DEM simulations and experiments. They investigated heating of particles between two sheared plates and also found that the dominating mode of heat transfer in their system depends on the shearing rate. Interestingly, the results in Figure 3.5 demonstrate that the heat transfer coefficient varies significantly even with a small amount of agitation so fixed bed heat transfer models may not be appropriate for systems with slight agitation. This may be significant as continuum models that use a fixed bed thermal conductivity are commonly used in dense granular flows.

3.3 Nondimensionalization

For systems where a significant number of parameters can influence a response, it can be useful to consider a dimensional analysis to reduce the number of variables in the problem. In this case, many thermal properties and operating conditions can influence heat transfer in a bladed mixer, making it difficult to achieve a thorough understanding of the system. The next step of the analysis therefore consists of using a dimensional analysis detailed in Emady *et al.* [43] to come up with a reduced number of important scaling parameters. In their work, DEM simulations were used to investigate the effect of agitation rate and conductivity on heat transfer in a rotating drum. They identified three important timescales relevant to the heating process in a rotary drum; here we try to apply these timescales to a bladed mixer. Figure 3.6 depicts a schematic of the three timescales relevant to heating in a bladed mixer geometry.

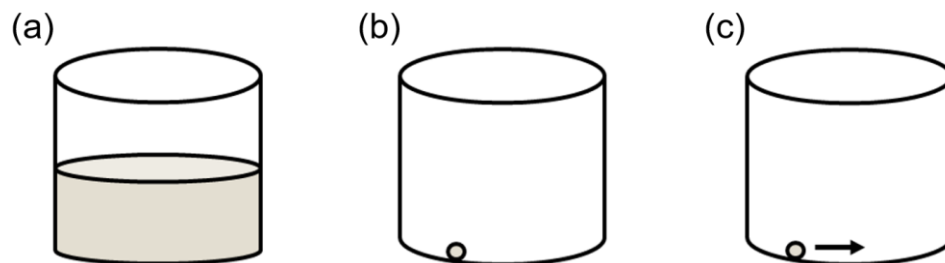


Figure 3.6: Three relevant timescales: (a) bed thermal time, (b) particle thermal time, (c) contact time.

It should be mentioned that flow and mixing behavior in a rotating drum and a bladed mixer greatly differ. It is therefore not at all obvious that the scaling used by Emady *et al.* [43] is an appropriate scaling for our system. As discussed by Bridgwater [97], there are two main classes of powder mixing equipment. In the first class, the shell rotates and these are often called tumbling blenders, which include the rotating cylindrical drums studied by Emady *et al.* [43] and Yohannes *et al.* [80]. In the second class of equipment, the shell is stationary and there are internal blades that move in order to achieve agitation of the powder, which include the bladed mixer considered in this work. In a rotating drum, the bed is angled on the wall of the cylinder and flow occurs due to gravity. In the work of Emady *et al.* [43] and Yohannes *et al.* [80], the top layer of particles flows down the surface of the bed and gets mixed along the surface and at the bottom. Mixing therefore only involves a relatively small fraction of the bed, leaving the core of the bed relatively unmixed. In our bladed mixer, impeller blades pass through the bed and create a significant displacement of particles throughout the bed with each revolution. As a result, the mixing process involves most of the particles during each rotation of the impeller.

Another important difference between our work and that of Emady *et al.* [43] and Yohannes *et al.* [80] is that they studied a narrow slice of the calciner with periodic

boundary conditions in the axial direction, meaning that their system was quasi-2-dimensional. In addition, they had a 1D imposed temperature gradient since they only had heating in the radial direction. The work presented here is for a 3D system and our system has a 2D imposed temperature gradient since we have heating in the radial and axial directions. At the same time, the scaling of Emady *et al.* [43] is able to collapse a large amount of data onto one line so it seems appropriate to try to apply it to our system.

The first time scale is τ_b , the thermal time for bulk heating, which has already been introduced in Equation 3.2. The second timescale τ_p represents the particle thermal time, or the time needed to heat a single particle (of the average size of particles in the bed) sitting on the wall. The wall is assumed to be at a constant temperature and the particle is resting under its own weight. In this case, an energy balance can be written for the single particle and the thermal time can be obtained analytically from the energy balance [43]:

$$\rho V C_p \frac{dT_i}{dt} = H_c (T_w - T_i) \quad (3.4)$$

where $H_c = 2ka$ and the variables are the same as in Equation 2.14 and Equation 2.16 from Chapter 2. The above equation can be integrated with the initial condition at $t = 0$, $T_i = T_{i,0}$ to obtain the analytical solution [43]:

$$\ln \left(\frac{T_w - T_i}{T_w - T_{i,0}} \right) = - \frac{2ka}{\rho V C_p} t = - \frac{t}{\tau_p} \quad (3.5)$$

with

$$\tau_p = \frac{\rho V C_p}{2ka} \quad (3.6)$$

where τ_p is the time required for the difference between the particle temperature and the wall temperature to drop by 63.2% of the initial difference i.e. at $t = \tau_p$ the difference

between the particle temperature and the wall temperature is 36.8% of the difference between the initial particle temperature and the wall temperature.

Finally, the third relevant timescale is the time that a particle spends in contact with the walls of the cylinder, τ_c . Since the flow of particles in the bladed mixer is somewhat complex, there is no obvious direct analytical expression for τ_c . However, since the flow is driven by the moving blades, this sets up a macroscopic time scale which can be related to the agitation rate. We therefore assume that τ_c is proportional to the inverse of the agitation rate and in its simplest form we can write the following relationship:

$$\tau_c = \frac{1}{\omega} \quad (3.7)$$

where the agitation rate ω is in units of radians per second.

The next phase of the analysis involves nondimensionalizing the data in Figure 3.5a, such that the relationship between agitation rate, conductivity, and heat transfer could be further examined. This was done in the hopes that the data can be collapsed into a single relation, such that we could draw broader conclusions about our system. Our approach for nondimensionalizing the results was based on previous work by Emady *et al.* [43] and was supported by applying the Buckingham π theorem (see Appendix A.1). The way Emady *et al.* [43] nondimensionalized their results is by plotting ratios of the heating timescales τ_b , τ_p , and τ_c until finding a proper combination that collapsed the data. They found that normalizing the bed and the particle thermal times by the contact time (τ_b/τ_c and τ_p/τ_c respectively) led to a collapse of the data. They defined a new dimensionless variable, ϕ , to represent τ_b/τ_c (Equation 3.8).

$$\phi = \frac{\tau_p}{\tau_c} = \frac{\rho C_p V \omega}{2ka} \quad (3.8)$$

In this work, we found that their scaling can be confirmed by applying the Buckingham π theorem to parameters relevant to heat transfer in this system, namely conductivity, density, specific heat capacity, agitation rate, volume, and contact radius. The theorem yielded three dimensionless groups: $\pi_1 = \tau_b \omega$, $\pi_2 = \frac{\rho C_p a^2 \omega}{k}$, and $\pi_3 = \frac{V}{a^3}$, which when combined and substituted for the timescales gave $\frac{\tau_b}{\tau_c} = f\left(\frac{\tau_p}{\tau_c}\right)$. As with Emady *et al.* [43], we defined the new dimensionless variable ϕ to represent τ_p/τ_c and obtained the final relationship $\frac{\tau_b}{\tau_c} = f(\phi)$.

Figure 3.7 illustrates that plotting τ_b/τ_c versus ϕ did collapse the data and yielded a linear relationship with a fairly high R^2 value. This plot is useful for scaling because if a new combination of k and ω were to be tested, the expected value of τ_b could be estimated from the fitted equation. The images A, B and C in Figure 3.7 correspond to the points labeled A, B and C in the graph and capture the particle temperatures at the time point when the bed has heated to a time that equals $\tau_b/2$. Interestingly, aligning the data in this way illustrated three heating regimes based on ϕ .

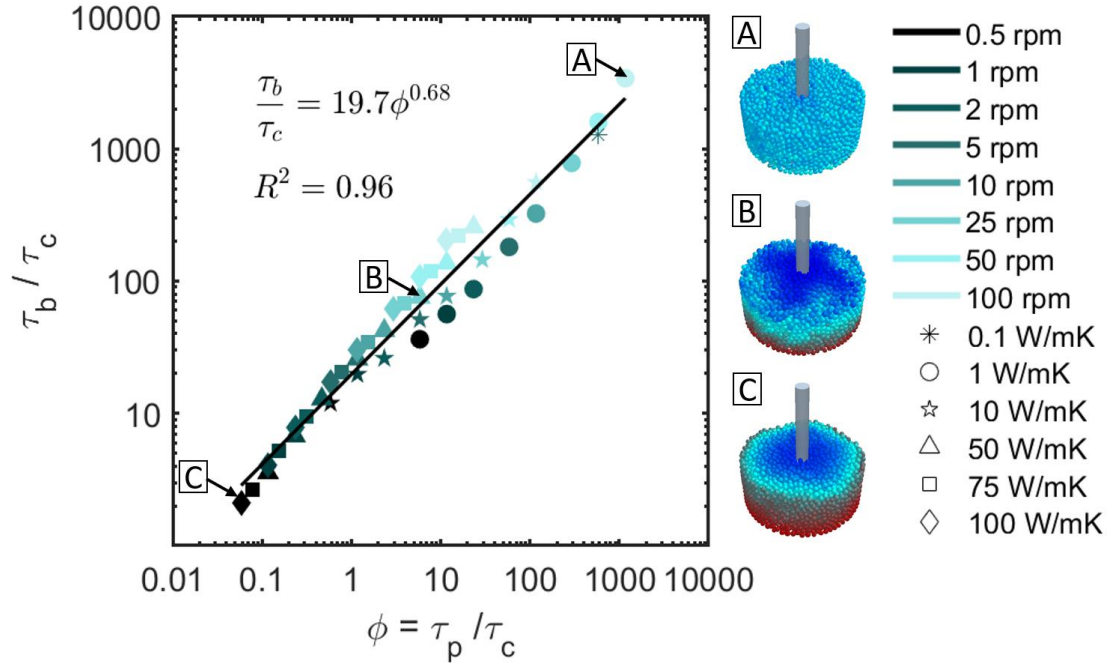


Figure 3.7: Nondimensionalization of the results showing different heating regimes based on ϕ .

A low ϕ yields a regime where hot particles along the vessel wall surrounded a colder core, forming annular rings of varying temperatures (image A). Low ϕ corresponds to beds with relatively low agitation rates and high thermal conductivities. This regime resembles how a static bed would heat up and represents a conduction-dominated regime where the bed heats rapidly but with a large temperature gradient. A high ϕ results in a fairly uniform temperature distribution (image C). High ϕ corresponds to beds with relatively high agitation rates and low thermal conductivities. This regime resembles how a well-mixed bed would heat up and represents a convection-dominated regime where the bed heats up slowly but uniformly. An intermediate ϕ leads to a regime with a smaller cross-shaped cold core that outlined the shape of the angled impeller blades pushing hot particles from the bottom of the vessel to the surface. In this regime conduction and granular convection contributed in a similar way to the heating of the bed.

It was also observed that conditions with a similar ϕ yielded heating regimes that look very similar, despite their different combinations of k and ω . Let us consider two different systems that have combinations of k and ω that lead to the same ϕ value. If the two systems have a ϕ value that is equal to the ϕ value labeled point A in the graph in Figure 3.7, then both systems would heat up in the same manner (in terms of t/τ_b) and both systems would look like image A in Figure 3.7 at $t = \tau_b/2$. The fact that different combinations of agitation rate and conductivity with the same ϕ led to similar heating regimes strengthens confidence in the dimensionless scaling.

Next, we draw a correlation between ϕ and the Peclet number, which is a more traditionally accepted dimensionless group for studies associated with heat transfer. The Peclet number for a granular flow describes the ratio of granular convection to granular conduction [98]:

$$Pe = \frac{\text{Convection}}{\text{Conduction}} = \frac{u^* L^*}{\alpha} \quad (3.9)$$

where $\alpha = \frac{k}{\rho C_p}$ is the thermal diffusivity, u^* is a characteristic velocity, and L^* is a characteristic length. One can write $u^* L^* = \frac{A^*}{t^*}$, where A^* and t^* are a characteristic area and time:

$$Pe = \frac{u^* L^*}{\left(\frac{k}{\rho C_p}\right)} = \frac{\left(u^* \frac{A^*}{t^*}\right)}{\left(\frac{k}{\rho C_p}\right)} \quad (3.10)$$

Since granular convection corresponds to the distribution of heat through particle movement within the bed, it can be assumed that the characteristic time scale for convection t^* is related to the mixing rate of particles. We can therefore define $t^* = \frac{1}{\omega}$ for

our system, where ω is the agitation rate of the impeller. Similarly, we can consider A^* as an effective area available for heat transfer and assume $A^* = \frac{V}{d} = \frac{V}{2a}$, where V is the particle volume, and d is the contact diameter (or double the contact radius a). Substituting these relations for t^* and A^* into Equation 3.10 gives:

$$Pe = \frac{\rho C_p V \omega}{2ka} = \phi \quad (3.11)$$

Through these assumptions we observe that our dimensionless scaling parameter ϕ is closely allied to the particle Peclet number for granular systems. The fact that we are able to determine a relationship between ϕ and an established dimensionless group like the Peclet number strengthens confidence in our scaling analysis.

Since the current scaling yielded some scatter in the data (Figure 3.7), we considered an alternative way to plot the results. As discussed above, we applied the Buckingham π theorem with the goal of obtaining different dimensionless groups, yet we obtained the same scaling. Rognon *et al.* [87], who studied the interplay between conduction and convection in a sheared plate using DEM simulations, also came up with a dimensionless scaling to collapse their data. Their scaling resembles ours except for the fact that they also incorporate an inertial number. Figueroa *et al.* [98] simulated granular conduction and granular convection due to mixing for rotating tumblers with different geometries and materials. They found scaling relationships involving the Nusselt number which enabled them to draw correlations across different equipment geometries but not different granular materials. They suggested that encompassing properties of the granular materials and their microstructure in their scaling could have helped them reconcile their results for different materials. We remain unsure as to what the exact cause of the scatter in the data could be, but it could reflect the assumptions made in the model. Scatter could

have been induced by differences in bed dilation from the different agitation rates, or the fact that the contact time τ_c has been approximated to only depend on the agitation rate. In the end, we are able to fairly effectively collapse results that vary by large orders of magnitudes onto a single line, so we feel that the scaling is still useful. At least, it serves as a step towards providing an estimate of heating times for heat transfer experiments in a bladed mixer system.

Most of the results shown in Figure 3.7 are for simulated materials with conductivities ≥ 1 W/mK due to the extremely long computational time required for running simulations with very low thermal conductivities. However, because some APIs tend to have thermal conductivities in the lower range of the studied values, we simulated a case where $k = 0.1$ W/mK to ensure that the scaling would still apply. Figure 3.7 demonstrate that this result also lies on the fitted line, making us confident that the scaling could be extrapolated to materials with lower conductivities.

3.4 Effect on the Bed Uniformity

In the pharmaceutical industry, obtaining a uniform temperature distribution is often a common objective during drying. Even more, for temperature-sensitive APIs, the drying protocol must be designed in a way that minimizes the risks of hot-spots during the process. Predicting the width of the temperature distribution based on the thermal properties of the bed, as well as on the operating conditions, could provide useful information when constructing a drying protocol. The results presented thus far focused on analyzing the mean temperature of the bed as a response, but one of the considerable advantages of DEM modeling is that it also allows the tracking of individual particles. As

an example, Figure 3.8a compares the temperature evolution of a single particle with the mean temperature of the bed. In Figure 3.8b, a similar plot was generated for all particles in the system to enable visualization of the deviation from the mean. These plots were derived from the simulation for the conditions $k = 50 \text{ W/mK}$ and $\omega = 100 \text{ rpm}$.

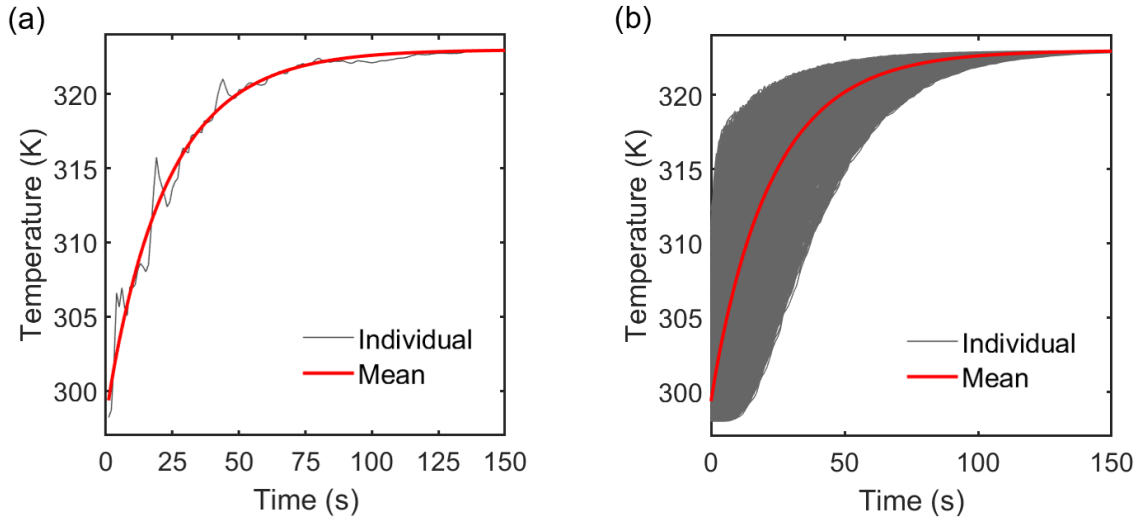


Figure 3.8: (a) Temperature evolution of an individual particle (gray) compared to the mean temperature (red). (b) Temperature evolution of all particles (gray) compared to the mean (red).

The temperature deviation from the mean can be further quantified by determining the frequency distributions of the temperature of the particles at a given time. Figure 3.9 shows that the distribution of particle temperature at a time when $\bar{T}_b = (T_w - T_0)/2$ is related to the dimensionless parameter ϕ .

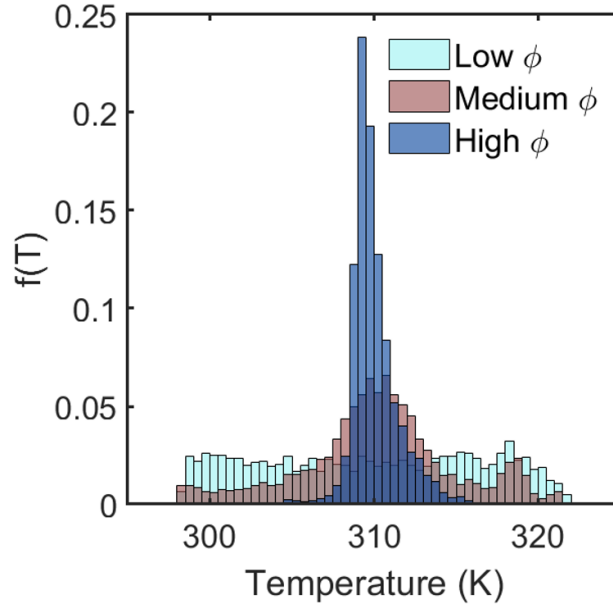


Figure 3.9: Frequency distribution of particles in the bed for low ϕ (0.5 rpm, 100 W/mK), medium ϕ (25 rpm, 50 W/mK), and high ϕ (100 rpm, 1 W/mK) at the time when $\bar{T}_b = \frac{(T_w - T_o)}{2}$.

Processing conditions with a higher ϕ induce a narrower temperature distribution than those with a low ϕ . This confirms the different heating regimes observed in Figure 3.7. This result can also be broken down and understood in terms of the effect of conductivity and agitation rate on the distribution of temperatures. In terms of the effect of conductivity, the results indicate that a low conductivity leads to narrower frequency distributions. The same trend was seen by Nguyen *et al.* [99] when they simulated heat transfer in a rotary drum and also noticed that a poorly conductive bed heated more slowly but more uniformly than a highly conductive bed. In summary, slow heating allows for more time for the temperature to equilibrate within the bed and leads to better uniformity. In terms of the effect of agitation rate, faster agitation leads to a more uniform distribution

of temperatures compared to slowly agitating the bed. This is expected as the agitation rate correlates with better mixing and therefore better uniformity within the bed.

Operating in a high- ϕ regime would ensure a more uniform temperature distribution across the bed and help prevent pockets of API from overheating. For a material with given thermal properties, one way of increasing ϕ would be to increase the agitation rate. However, while that would improve the temperature uniformity, agitating rapidly can also lead to particle breakage, which is typically an undesirable phenomenon [100]. In a real experiment, there may therefore be a balance between agitating rapidly enough to enhance heat transfer and to obtain good temperature uniformity while minimizing the risk for attrition.

Predicting the width of the temperature distribution could prove to be a useful tool for creating an optimal drying protocol. In the next portion of the analysis, we model the standard deviation, σ_T of the temperature distribution as an exponential decay and relate it to the thermal properties and operating conditions of the system. Figure 3.10a and 3.10b illustrates the normalized standard deviation, $\sigma_T^* = \frac{\sigma_T}{(T_w - T_0)}$, of the temperature distribution over time for a poorly and highly conductive material.

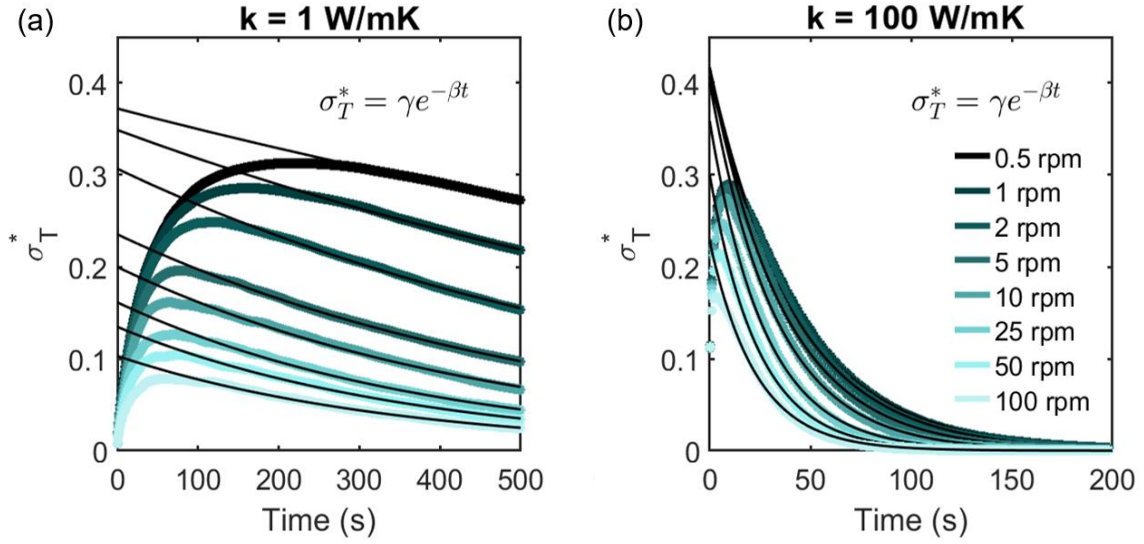


Figure 3.10: Normalized standard deviation over time for a material with (a) low conductivity ($k = 1 \text{ W/mK}$) and (b) high conductivity (100 W/mK) for varying agitation rates. Data are fitted to an exponential decay equation with coefficients γ and β (black solid line). The legend in Figure 3.10b is applicable to Figure 3.10a.

It shows that the standard deviation of the bed has two distinct periods: a rising phase and a descending phase. In the rising period, particles start heating from a uniform temperature T_0 until the temperature gradient increases and the standard deviation reach a maximum. During the descending period, the temperature gradient decreases as particle temperatures gradually reach an asymptote towards the wall temperature T_w . Since the system spends most of the time in the descending phase as it slowly approaches the target temperature, predicting the features of this phase was the focus of our analysis. The descending phase can be characterized by an exponential decay function with the form:

$$\sigma_T^* = \gamma e^{-\beta t} \quad (3.12)$$

where γ and β are fitting coefficients. γ regulates the vertical stretch of the exponential decay, which relates to the maximum of the standard deviation. β controls the slope of

the exponential decay, which corresponds to how quickly the bed temperature approaches uniformity. Yohannes *et al.* [80] found that the standard deviation of temperatures for particles in a rotating drum could be described by an exponential decay equation with a single fitting coefficient. We found that for a bladed mixer, we need 2 fitting coefficients (γ and β) to appropriately model the standard deviation of the temperatures. We presume that the need for a second fitting coefficient has to do with the different flows and mixing behaviors between these geometries.

Next, we related the fitting coefficients γ and β to the thermal properties and operating conditions of the system by making use of the scaling parameters developed previously. Figure 3.11a demonstrates the value of the fitting coefficient γ as a function of the dimensionless parameter ϕ . The data were codified into symbols according to their corresponding thermal conductivity to allow for a more thorough analysis. We find that the relationship between γ and ϕ is rather complex.

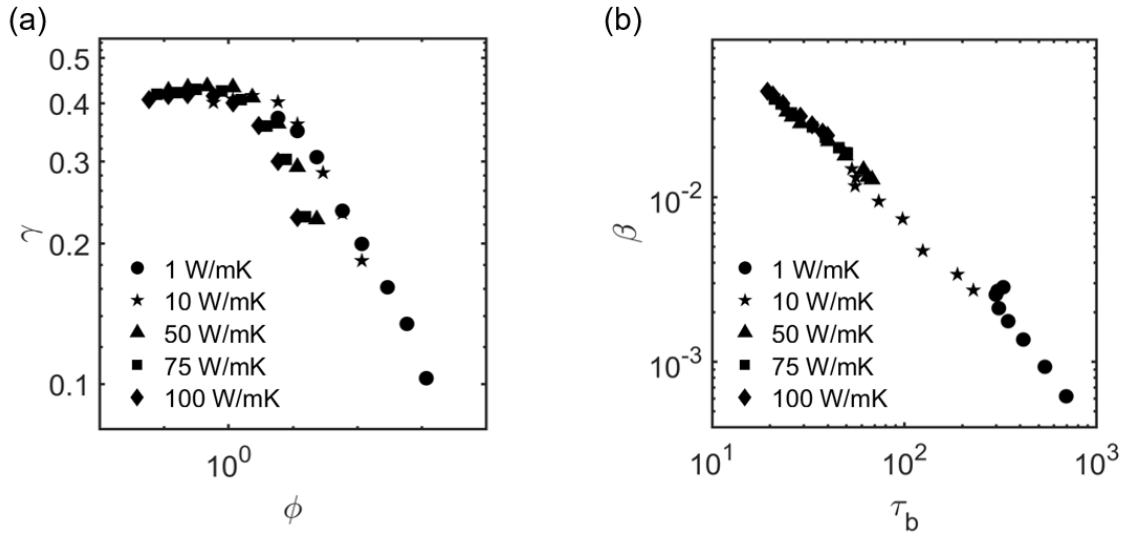


Figure 3.11: Coefficients (a) γ and (b) β of the exponential decay as a function of ϕ and τ_b respectively. The data have been codified into symbols according to thermal conductivity.

The value of γ appears to be relatively constant for low ϕ (slow agitation rates, high k), and then drops rapidly for increasing ϕ (fast agitation rates, low k). For the thermal conductivity $k = 1$ W/mK, the relationship between γ and ϕ becomes nearly linear as ϕ increases. Figure 3.11b shows the relationship between β and the bed heating timescale τ_b , which appears to follow a simple linear model. The trend suggests that the longer a bed needs to heat based on its thermal properties and operating conditions, the slower the temperature gradient decays. Since we can calculate ϕ and τ_b from our previous work on the mean temperature, this analysis allows for an approximative prediction of the expected standard deviation.

Despite the numerous differences between the bladed mixer system described in this work and the rotary drum system simulated by Emady *et al.* [43] and Yohannes *et al.* [80], we found it interesting that a similar scaling approach could be successfully applied. The physical geometry and dimensions are notable differences in themselves but more importantly, the flow and mixing behavior in each equipment greatly differ. Additionally, Emady *et al.* [43] and Yohannes *et al.* [80] modeled a 2D system while the work presented here is in 3D. The fact that the scaling works relatively well for both geometries begs the question of whether it could be a universal scaling that could potentially work for other geometries and different flows.

3.5 Conclusions About the Effect of Thermal Properties and Agitation Rate on Heat Transfer

Drying influences the Critical Quality Attributes (CQAs) of an API in several respects and must therefore be conducted carefully. It is a complex unit operation, and proper design of the drying protocol must be implemented based on the API's thermal properties such that the product's CQAs can be met and risks such as degradation, incomplete and nonuniform drying, agglomeration, and attrition can be minimized. For procedures that make use of a bladed mixer, optimizing the agitation rate of the impeller can play a key role in mitigating these challenges. This work studied the effect of agitation rate and thermal conductivity on heat transfer in a bladed mixer. The extent to which the agitation rate improved heating was found to depend on the bed's conductivity. For a poorly conductive material, slowly agitating the bed improved the heat transfer coefficient significantly but further increasing the speed of the impeller led to a negligible improvement. This is because poorly conductive materials heated uniformly with a small amount of mixing. Further mixing an already uniform bed did not provide a benefit in terms of heat transfer. For highly conductive materials, the bed was found to heat up rapidly but nonuniformly. A fast agitation rate provided a considerable improvement to the rate of heat transfer, as it enabled particles of different temperatures to come into contact. Interestingly, slowly agitating a highly conductive bed was found to slightly hinder heat transfer compared to no agitation. This phenomenon was explained by the sharp drop in coordination number that occurred when slowly agitating the bed, leading to a decrease in conduction in the bed and not enough granular convection to overcome the decrease in heat transfer.

The analysis was further expanded by identifying dimensionless groups for the system and nondimensionalizing the results. Three heating regimes were observed: a conduction-dominated regime where the bed heated rapidly but with a large temperature gradient, a convection-dominated regime where the bed heated slowly but uniformly, and an intermediate regime where conduction and granular convection contributed relatively equally. The identified dimensionless parameters were used to obtain a mathematical relationship between agitation rate, conductivity, and heat transfer, thereby enabling prediction of the mean temperature of the bed. The equation could be used to estimate the time needed to heat a bed given its thermal properties and would allow the agitation rate to be optimized such that it provides a fast rate of heat transfer while minimizing the risk of attrition. Additionally, the discrete aspect of DEM modeling was leveraged to study the temperature distribution of the bed. The standard deviation of the particle temperatures was fitted to an exponential decay equation and the fitting coefficients were studied in terms of the scaling parameters. Together, the results allowed for an approximate prediction of the mean temperature of the bed as well as the standard deviation of the distribution.

4. INFRARED TEMPERATURE EXPERIMENTS AND VALIDATION OF DEM SIMULATIONS

In this chapter, we conducted heat transfer experiments using a laboratory-scale agitated dryer and an infrared camera to measure the temperature of the surface of a particle bed over time. The experiments were carried out using glass beads as a model material. The temperature data collected by the thermal camera were used to compute the heat transfer coefficient for the system as well as the temperature standard deviation, giving information about both the mean temperature of the bed and its temperature uniformity. Using this methodology, we investigated how the impeller rotation rate influences heat transfer. We present a comparison between the experimental results and the results from discrete element method (DEM) simulations. The model makes use of a particle-particle and particle-wall conductive heat transfer model to describe the system, as described in Chapter 2.

4.1 Heat Transfer Experiments

As discussed in Chapter 2, the height of the blades was 15mm and the clearance of the blades from the bottom of the vessel was 10mm. The vessel was filled with material to a height of 35mm (corresponding to 10mm above the top of the blades). During agitation, the surface of the bed moved with the blade passes and it could be seen that there was mixing between the surface and the bulk of the bed. Heating experiments were conducted for five different impeller agitation rates: 0 rpm (no agitation), 5 rpm, 10 rpm, 25 rpm, and 100 rpm. Three replicates were done for each agitation rate. Figure 4.1 shows typical thermal images obtained from the infrared camera during an experiment.

The experiment presented in Figure 4.1 is for a case where the impeller was agitated with a rate of 5 rpm. At the beginning of the experiments, all the beads start with an initial temperature of T_0 (i.e.: room temperature). At $t = 1$ min, Figure 4.1 indicates that the bed had started heating but that the temperature of the bed surface was still relatively close to T_0 . Over time, the temperature of the bed surface rose until gradually approaching T_w (i.e.: the temperature of the wall) at $t = 25$ min.

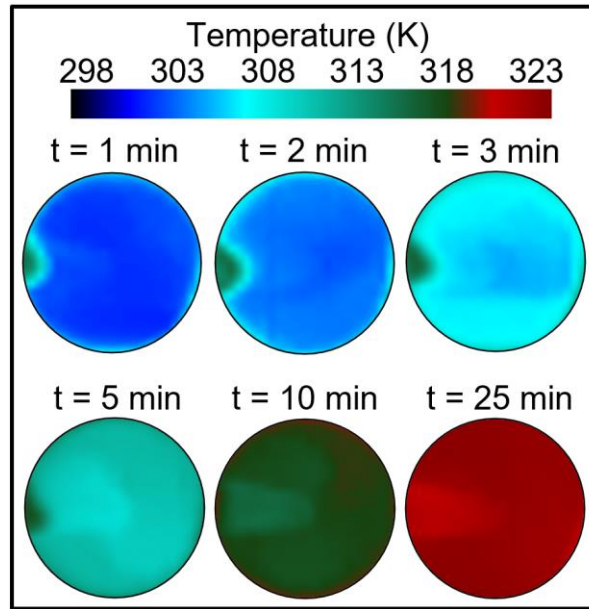


Figure 4.1: Thermal images for glass beads over time. The impeller agitation rate was set to 5 rpm.

Figure 4.2 depicts the thermal images obtained for experiments where the impeller agitation rates were set to 0 rpm, 5 rpm, 10 rpm, 25 rpm, and 100 rpm. For each agitation rate, the temperature of the bed surface started out around room temperature and increased until it approached the temperature of the heating jacket. The images in Figure 4.2 provide visual information about how the impeller speed influenced the rate of heat transfer in the bed as well as the temperature uniformity. For example, as expected, we see that the case without agitation (0 rpm) led to slower and less uniform heating than the

cases with rapid agitation. For the case with 0 rpm agitation, the bed surface had an average temperature around 315 K at $t = 10$ min and exhibited significant nonuniformity. The material near the edge of the vessel heated up first while the material at the core of the surface was noticeable colder. For the case with 100 rpm agitation, the bed surface had an average temperature around 322 K at $t = 10$ min and demonstrated significantly better heating uniformity.

Another observation that can be made about Figure 4.2 is the presence of the impeller. For example, the shaft of the impeller is particularly visible in the thermal images for 10 rpm, 25 rpm, and 100 rpm after 5 minutes of heating. This is because the impeller had a different thermal conductivity than the glass beads and therefore did not heat up at the same rate as the particle bed. In this work, we were only interested in measuring the temperature of the bed surface, so the impeller shaft was excluded from the images to prevent its influence on the results. The procedure to remove the impeller from the images is discussed in Chapter 2. Interestingly, the shape of the two impeller blades is also noticeable in some cases (e.g.: 5 rpm at $t = 5$ and 10 min, 10 rpm at $t = 5$ and 10 min). The impeller blades were submerged by the glass beads so here, the shape outline does not represent the blades themselves but rather the temperature gradients created by the blades moving through the bed. This phenomenon was also observed and discussed in the simulations presented in Chapter 3 (see Figure 3.2). Hot particles heated by the bottom wall were pushed up to the surface by the blades. At the same time, the colder particles at the surface of the bed slid down to fill the void left behind the blades. This created a temperature vortex in the bed and led to the temperature gradients exhibited at the surface of the bed.

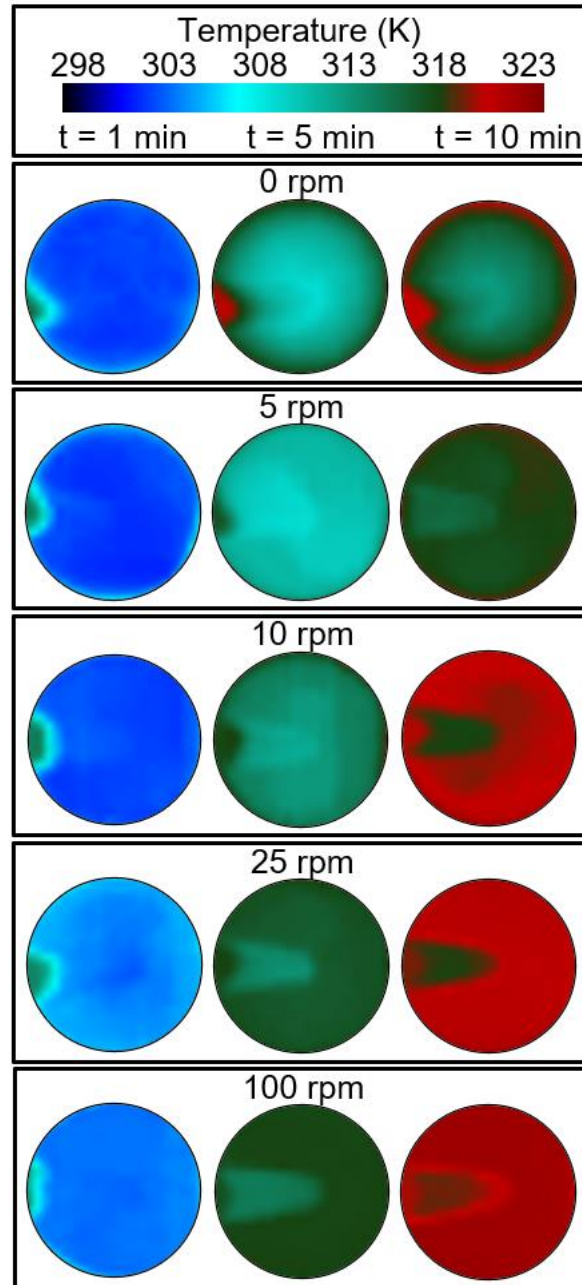


Figure 4.2: Thermal images of the bed surface over time for different agitation rates.

Next, temperature data were extracted from each image and the mean temperature of the bed surface was calculated over time for each experiment. Figure 4.3a illustrates the mean temperature of the bed surface over time for the three replicates for the case

with 5 rpm agitation rate. Overall, Figure 4.3a demonstrates that good reproducibility was achieved between the replicates throughout the heating process. However, one significant difference is the starting temperature of the material. For example, the starting temperature of trial 2 is higher than that of trial 1 and 3. This was due to day-to-day variability in the temperature of the laboratory. One way of accounting for disparities in the starting temperature of each experiment is to normalize the temperature of the bed by the initial temperature difference between the material and the jacket. Figure 4.3b implements this procedure and plots the normalized temperature T^* over times for each trial. The dimensionless temperature is computed from Equation 4.1:

$$T^*(t) = \frac{T_w - T(t)}{T_w - T_0} \quad (4.1)$$

where T_w is the wall temperature, T is the temperature of the bed surface at time t , and T_0 is the starting temperature of the material. The heating time of the bed surface τ_s and the effective heat transfer coefficient between the wall and the bed surface h_{eff} can be computed from the slope of the graph in Figure 4.3b. This procedure is described in greater detail in Chapter 2.

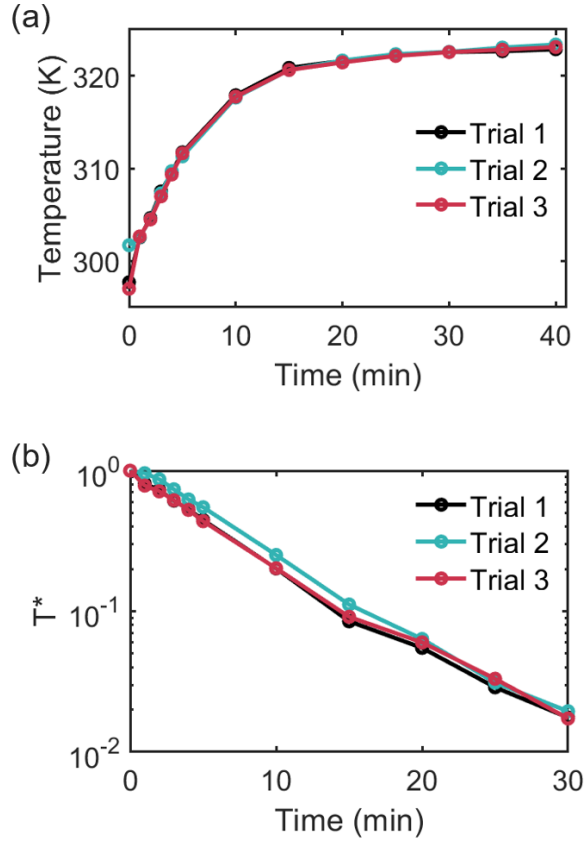


Figure 4.3: (a) Temperature of the bed surface versus time for 5 rpm agitation rate. The plot shows the reproducibility of the experiment over 3 trials. (b) Dimensionless temperature versus time for 5 rpm agitation rate.

Figure 4.4 shows results for the different agitation rates that were investigated in this work. Figure 4.4a depicts how the agitation rate influences the mean temperature of the bed over time. As expected, the results indicate that without agitation, the bed temperature takes longer to approach that of the heating jacket, compared to the cases with agitation. Overall, the faster the agitation rate the faster the temperature increase of the bed surface. The trends in Figure 4.4a are even more discernable in Figure 4.4b, where each temperature profile is summarized into a single value denoted as τ_s , which is the heating time for the bed surface. Figure 4.4b leverages the data from Figure 4.4a to illustrate the relationship between the agitation rate of the impeller and the heating time.

Figure 4.4b shows that agitating the bed decreases the heating time of the bed but that the relationship is not linear. For example, going from no agitation to 5 rpm agitation led to a ~ 25% decrease in heating time, while going from 25 rpm to 100 rpm led to a ~9% decrease in heating time. Similarly, Figure 4.4c shows the relationship between the agitation rate and the heat transfer coefficient h_{eff} , which is a measure of how quickly heat is transferred between the jacket and the bed. Overall Figure 4.4c illustrates a similar message: increasing the agitation rate can significantly improve heat transfer but agitating very rapidly does not necessarily equate to a large improvement in the heat transfer coefficient. These results have potentially important implications for pharmaceutical materials. In agitated drying processes of APIs, preserving the particle size distribution of the material is often critical but can be difficult to achieve if API particles are susceptible to attrition. In these cases, selecting an agitation rate that improves heat transfer but maintains low shear forces in the bed can be essential. The results in Figure 4.4 suggest that in terms of heat transfer, a little bit of agitation goes a long way, while agitating very rapidly would provide limited benefit but increase the risk of particle breakage.

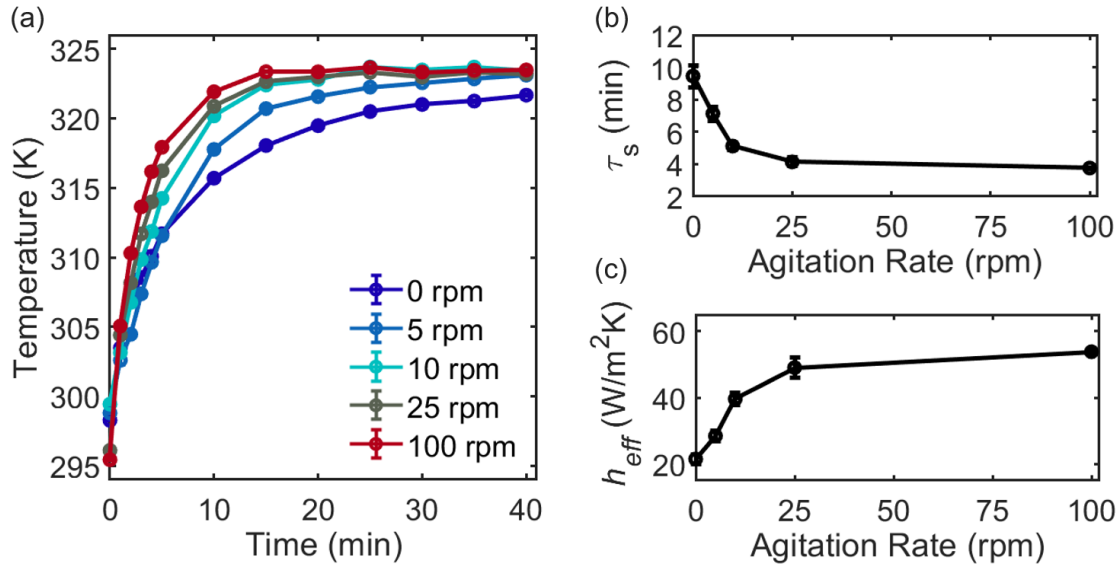


Figure 4.4: (a) Mean temperature of the bed surface over time for different agitation rates. (b) Heating time of the bed surface for different agitation rates. (c) Effective heat transfer coefficient of the bed surface for different agitation rates.

The next portion of our analysis involves analyzing the influence of the agitation rate on the temperature distribution of the bed surface. Figures 4.5a, 4.5b, 4.5c, and 4.5d depict the temperature distribution at different time points over the course of the experiment for 0 rpm, 5 rpm, 10 rpm, and 100 rpm, respectively. Figure 4.5a shows that for the case without agitation, the distribution starts out narrow (the particles all start at room temperature), becomes very wide (the particles near the jacket heat up first while the center of the bed remains cold), and then eventually becomes more narrow towards the end as the bed approaches the jacket temperature. For 100rpm, the temperature distribution remains very narrow throughout the heating process as the bed is agitated rapidly and particles all have a temperature close to the mean temperature of the bed at any time. The distributions for 5rpm and 10rpm indicate behaviors between 0rpm and 100rpm.

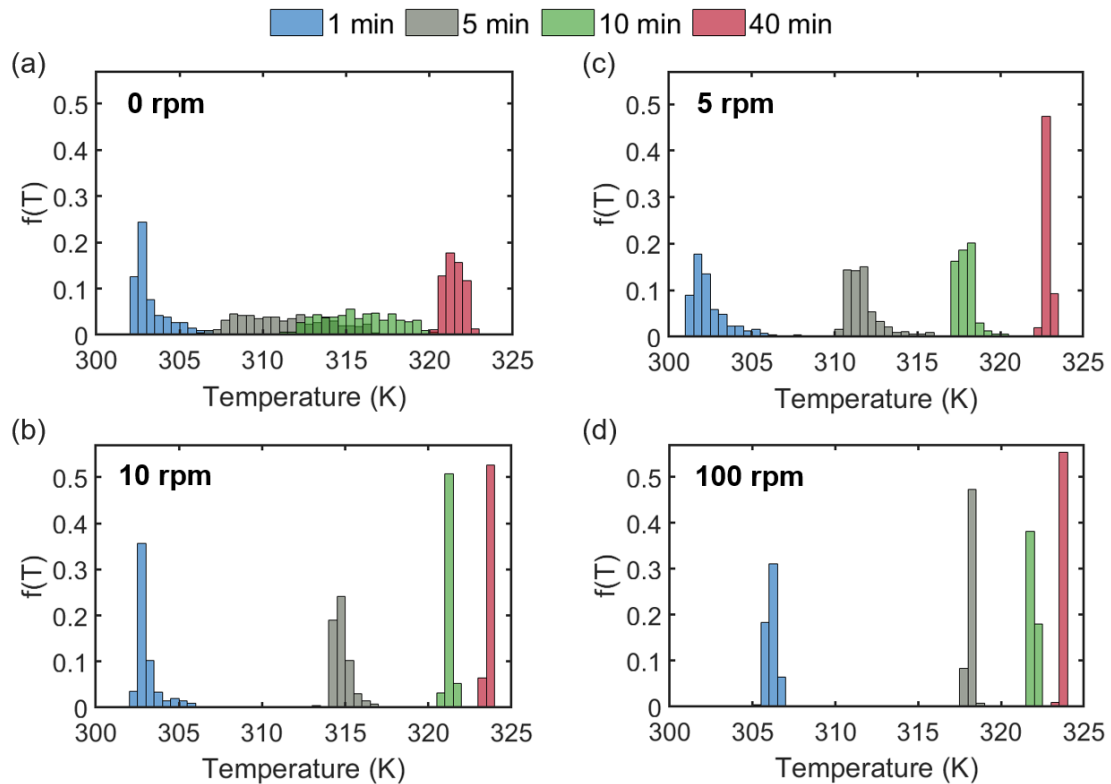


Figure 4.5: Histograms showing the temperature distribution of the bed surface after $t = 1$ min, 5 min, 10 min, and 40 min of heating for an impeller agitation rate of (a) 0 rpm, (b) 5 rpm, (c) 10 rpm, (d) 100 rpm.

Figure 4.6 overlays some of the results shown in Figure 4.5 and demonstrates how the agitation rate affected the temperature distribution of the bed surface after 5 minutes of heating. The temperature uniformity of the bed is often an important consideration when designing an operating protocol for an agitated drying process. Ideally, the bed should heat up uniformly to prevent hot spots or cold regions in the bed. It is therefore important to not only look at how the agitation rate influences the mean temperature of the bed, but also how it affects the temperature uniformity. Figure 4.6 shows that after 5 minutes of heating, the cases with no agitation not only had the lowest average

temperature but also had the widest distribution. Increasing the agitation rate to 5pm significantly narrowed the temperature distribution, suggesting that even a little bit of agitation may be enough to improve the heating uniformity of the bed considerably.

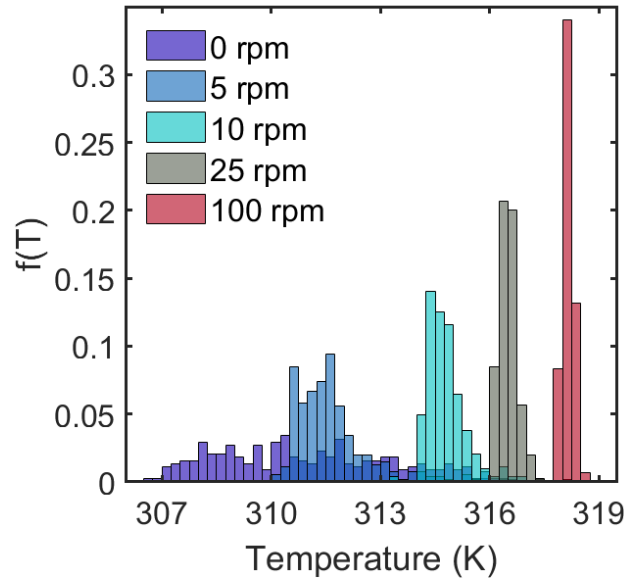


Figure 4.6: Temperature distribution of the bed surface after $t = 5$ min of heating for different impeller agitation rates.

Next, the information in Figures 4.5 and 4.6 was used to calculate the standard deviation of the bed surface temperature. Figure 4.7a shows the temperature standard deviation for the case with 5 rpm agitation for three different experiments, labeled “Trial 1”, “Trial 2”, and “Trial 3”. Overall, the results in Figure 4.7a indicate that the temperature uniformity of the bed surface was fairly reproducible, as similar results were obtained for each trial. At the start of the experiment ($t = 0$ min), the temperature standard deviation is 0 because all the beads started at room temperature. Around $t = 3$ min, the temperature standard deviation peaked, meaning that the bed was the least uniform at this point due to the high temperature gradient between the warmer beads located near the hot walls and the colder beads located in the colder core of the bed. Over

time, the temperature standard deviation decreased as the bed temperature uniformly approached that of the jacket. In theory, as $t \rightarrow \infty$, the temperature standard deviation should decrease to 0. The reason the results in Figure 4.7a and Figure 4.7b do not quite reach 0 may be due to experimental error or the sensitivity of the infrared camera.

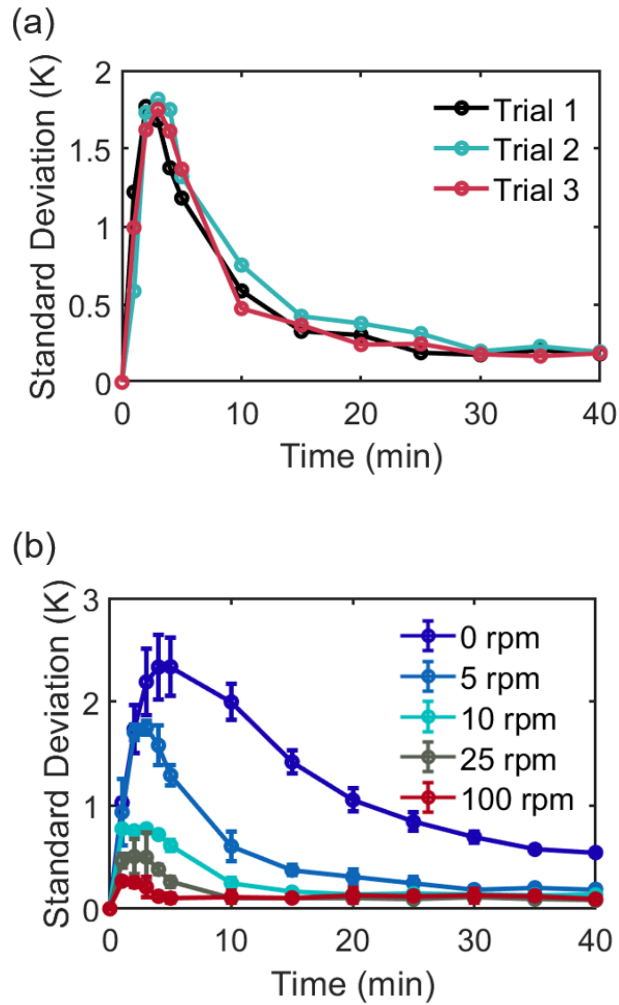


Figure 4.7: (a) Temperature standard deviation of the bed surface over time for 5 rpm agitation rate. The plot shows the reproducibility of the experiment over 3 trials. (b) Temperature standard deviation of the bed surface for different impeller agitation rates. The error bars represent 3 replicates for each agitation rate.

Figure 4.7b shows the temperature standard deviation of the bed surface over time for the different agitation rates tested. The error bars represent the three replicates conducted for each case. Overall, the error bars are relatively small for all agitation rates, meaning that the bed temperature uniformity was fairly consistent between each replicate. The profiles exhibited similar trends: the standard deviation profiles started at zero, peaked after a few minutes, and then gradually decayed. Interestingly, the standard deviation peaked at different time points for each agitation rate. More specifically, we found that the faster the agitation rate, the earlier the standard deviation peaked. The peak times were approximately 5 min, 3 min, 3 min, 2 min, 1 min for 0 rpm, 5 rpm, 10 rpm, 25 rpm, and 100 rpm, respectively. The dependence of the peak time on the agitation rate is likely because agitating enhances the bed uniformity and therefore reduces the standard deviation more rapidly. These results provide valuable quantitative information about how much agitation is needed to reach a desired temperature uniformity and how much time it takes. For example, for this setup, to reach a temperature standard deviation of 1 K, one could wait ~ 22 min without agitation, one could agitate at 5 rpm for ~ 7 min, or one could agitate at 10 rpm for less than 1 min. If a maximum temperature standard deviation of 1 K is acceptable, then the results in Figure 4.7b suggest that there is no advantage to agitating faster than 10 rpm in terms of heat transfer. This kind of information may be particularly important for deciding an agitating protocol for brittle APIs. A risk-benefit analysis could be done where the improvement in cycle time achieved by a certain agitation rate could be weighed against the attrition potential of the material.

4.2 Comparison with Heat Transfer Simulations

Figure 4.8 depicts the heated bladed mixer used in the experiments and the model representation used in the DEM simulations. A notable difference between the experimental and the simulation setup is the presence of the heating jacket. In the experimental setup (Figure 4.8a), the bladed mixer had a heating jacket around the side and bottom walls with hot water flowing inside continuously. A circulator regulated the temperature of the water such that it had a relatively constant temperature of T_w . In the simulation setup (Figure 4.8b), we assumed that any heat loss within the heating jacket was minimal, and we thus did not model the heating jacket and the water. Instead, the temperature of the side walls and the bottom walls of the vessel were directly assigned a temperature of T_w . The dimensions of the simulated vessel were adjusted to match those of the experimental vessel. For the impeller, a CAD drawing was created to replicate the experimental dimensions of the shaft and blades and was integrated into the DEM software. The dimensions of the setups were previously discussed in Section 2.2.1.

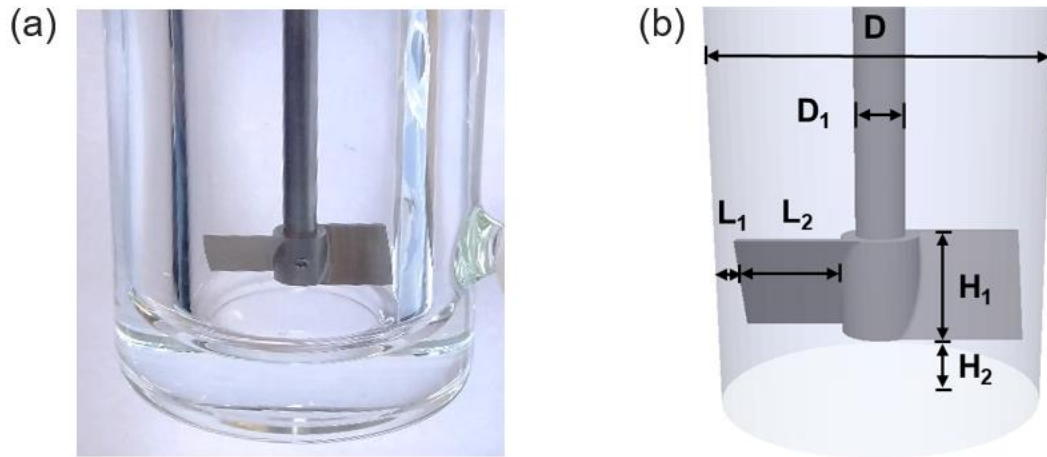


Figure 4.8: (a) Close-up of the agitated dryer system. (b) Model representation of the system used in the DEM simulations.

It is important to note that there were a few differences between the simulations and the experiments. Modeling the exact material properties of the glass beads was not feasible as it would have led to prohibitively long computational times. The simulated particles had an average diameter of 2 mm, while the glass beads used in the experiment had a diameter of 100 μm . The simulated particle size was chosen to be large enough to simulate fewer particles and decrease the computational time but small enough to still be representative of a bed of particles. Another difference was that the simulated particles were softer than the true material. The simulated elastic modulus was 6.5×10^6 Pa, while the true elastic modulus for the glass beads was around 6.9×10^{10} Pa. The reason for this was again to decrease the computational time for each simulation. We expect that both the particle size and the softness of the particles would affect heat transfer in the bed. In the experiment, the bed had small particles, leading to smaller voids in the bed, more contacts, and therefore potentially better heat transfer. At the same time, the particles in the experiment were stiffer, leading to smaller contact areas between the particles, and therefore potentially worse heat transfer. Finally, the experiment had heating through the interstitial gas, while the heat transfer model did not account for this phenomenon.

When considering these effects together, it was not obvious to us how modeling large soft particles without an interstitial gas would compare to the scenario case with small stiff particles and an interstitial gas. We hypothesized that the effects of these differences could be lumped together and that we could capture them in our model by inputting an “effective” thermal conductivity into the simulations. The input value of the thermal conductivity k for our simulations was calibrated from one experiment (25 rpm) by using the dimensionless scaling developed previously in Chapter 3 (see Figure 3.7).

Figure 4.9a and Figure 4.9b illustrates the procedure to calibrate k . Previously, in Chapter 3, we had found that by plotting $\frac{\tau_b}{\tau_c}$ versus $\frac{\tau_p}{\tau_c}$ we were able to collapse the simulation data together and obtain an equation relating the heating time of the bed τ_b , the agitation rate, and the thermal properties of the material. Similarly, Figures 4.9a and 4.9b plot $\frac{\tau_s}{\tau_c}$ versus $\frac{\tau_p}{\tau_c}$, where τ_s is the heating time of the surface instead of the bed, to collapse the data together. In Figure 4.9a, we first ran simulations without knowing the thermal conductivity and used $k = 5.0$ W/mK as an input (i.e.: the “Uncalibrated Simulations”). Figure 4.9a also overlays the experimental result for the 25 rpm case and we can see that it does not match the uncalibrated simulations well. Next, we fitted a line to the uncalibrated simulations to obtain an equation between the surface heating time, the agitation rate, and the thermal properties of the material: $\frac{\tau_s}{\tau_c} = 9.9 \left(\frac{\tau_p}{\tau_c} \right)^{0.9}$. We plugged the value of τ_s measured from the experiments for 25 rpm into the equation and solved for k . We obtained $k = 2.5$ W/mK as the calibrated thermal conductivity for the model. Figure 4.9b describes the new set of simulations using $k = 2.5$ W/mK and shows that relatively good agreement was achieved with the experiments. The implications of Figure 4.9 are significant because they indicate that we can use one experiment to calculate the thermal properties of the material and approximately predict the heating time of the bed surface for other agitation rates.

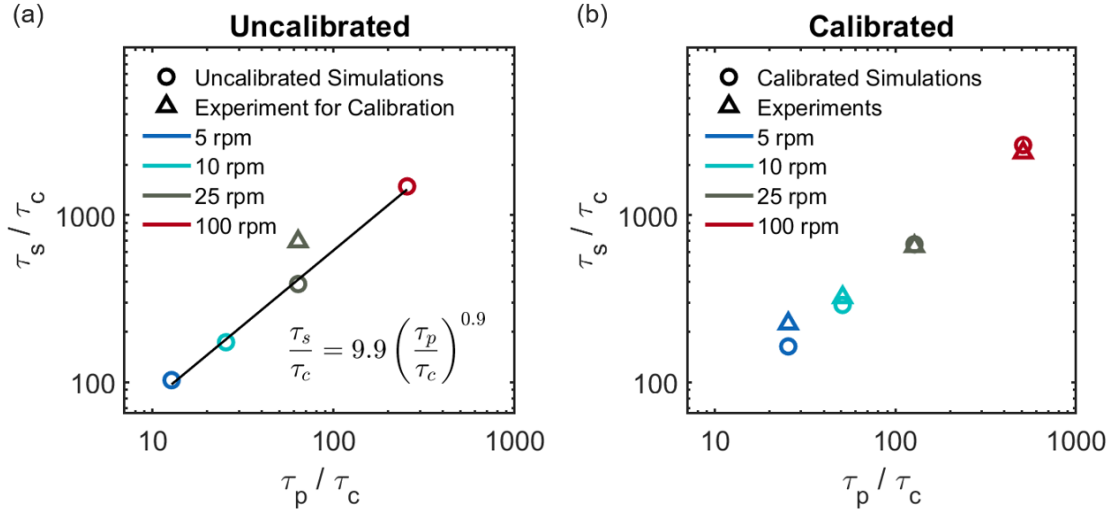


Figure 4.9: Using the dimensionless scaling to calibrate k . (a) Uncalibrated simulations ($k = 5$ W/mK), the fitting equation, and the experiment used for the calibration (25 rpm). (b) Calibrated simulations ($k = 2.5$ W/mK) and the experiments for 5 rpm, 10 rpm, 25 rpm, and 100 rpm.

Figure 4.10 shows visuals of the experiments and the simulations at times $t = 1$ min, 5 min, and 10 min for 0 rpm, 5 rpm, 10 rpm, 25 rpm, and 100 rpm. The simulations in this figure and subsequent figures are for the calibrated thermal conductivity of $k = 2.5$ W/mK. The thermal images for the experiments are the same as in Figure 4.2 but have been reproduced here to allow for easy comparison with the simulations. The particles in the simulations are color coded according to temperature and use the same legend as the experiments. Overall, Figure 4.10 shows fairly good visual agreement between the experiments and the simulations for agitation rates of 5 rpm and above. We see that in both cases, the faster the rate of agitation, the hotter and the more uniform the bed surface is after a few minutes of heating. Visually, the simulation results for 5 rpm show much better uniformity and greater temperatures than the case without agitation. The cases for 25 rpm and 100 rpm look very similar in terms of both the average temperature and the

uniformity of the bed. This validates the experimental results and confirms that a little bit of agitation goes a long way, and that very fast agitation is not necessarily beneficial to the heating process.

Figure 4.10 also indicates that the model is not able to fully capture the experimental results for the case with 0 rpm. Both the simulation and the experiments show a similar heating pattern where the temperature gradient in the bed displays concentric rings of varying temperatures. However, we notice that the mean temperature of the bed surface is much lower in the simulation than the experiments. We hypothesize that the reason for this is due to the value of the thermal conductivity k we input into the model. The value for k was calibrated using experiments for an agitated bed (see Figure 4.9). Static beds have different thermal properties than agitated beds due to differences in particle contacts and particle overlaps. Shallow agitated beds such as the ones in this work tend to undergo dilation and contain more voids than a static bed, leading to a lower effective thermal conductivity. By contrast, we would expect a static bed to be denser and to therefore have a slightly greater effective thermal conductivity than an agitated bed. This suggests that the model needs to be calibrated differently for a static bed and that the value for k for the static bed in our simulations should be greater than $k = 2.5 \text{ W/mK}$.

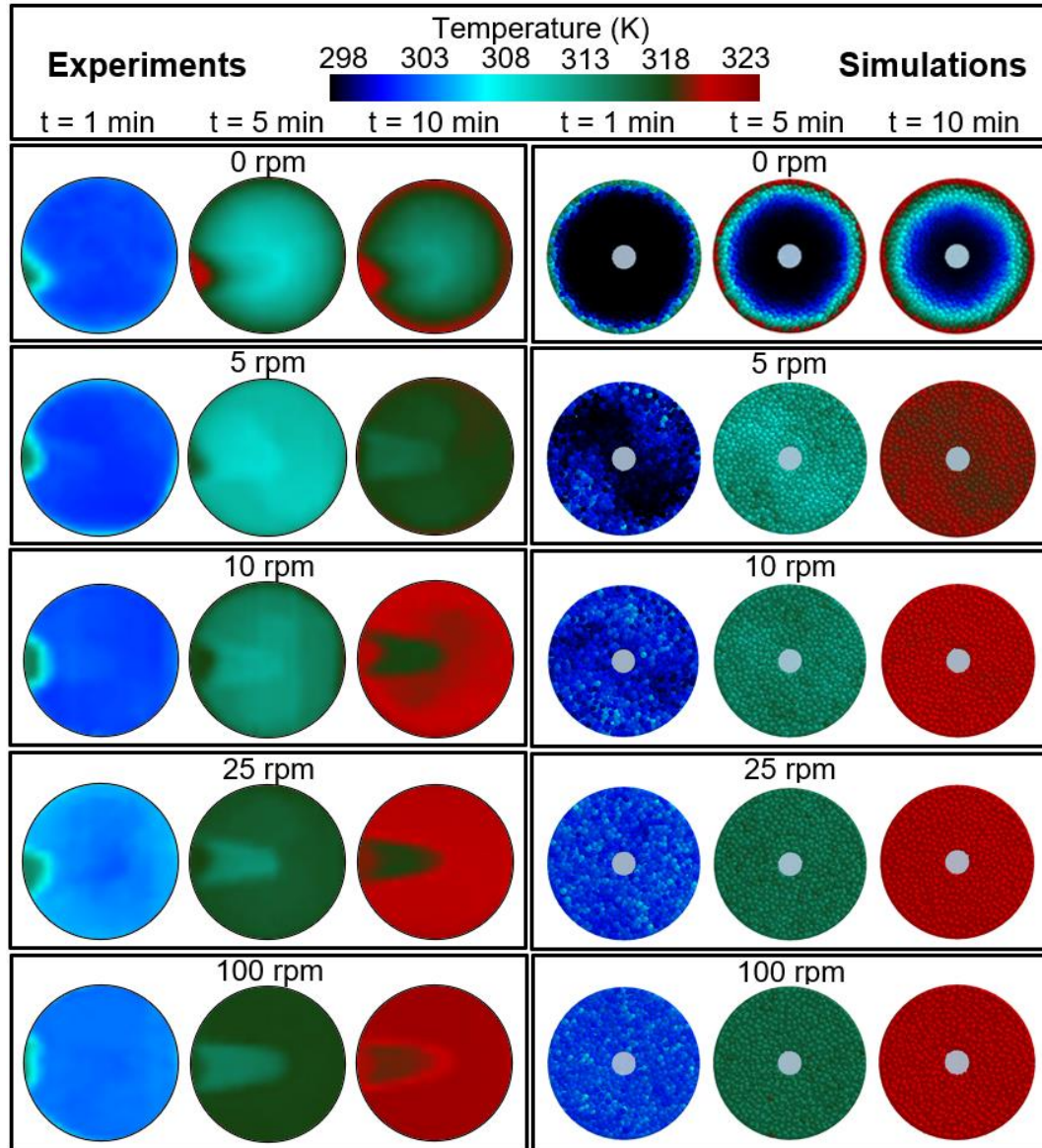


Figure 4.10: Comparison of the experimental thermal images (left) and the DEM simulations (right) for different agitation rates after 1, 5, and 10 minutes.

Figure 4.11 expands on the findings illustrated in Figure 4.10 by providing a quantitative comparison of the experimental and modeling results. Figures 4.11a and 4.11b show the mean temperature of the bed surface for the experiments and the simulations, respectively. Overall, the experiments and the simulations agree fairly well for the cases with 5 rpm, 10 rpm, 25 rpm, and 100 rpm agitation. The case for 0 rpm,

however, shows that the experiment heated up considerably faster than the prediction from the simulation. This confirms the results previously discussed in Figure 4.10 and further suggests that the model may need to be calibrated separately for a static bed. Another difference between Figure 4.11a and 4.11b is that the simulation always started with $T_0 = 298$ K, while the experimental initial temperature varied from experiment-to-experiment due to daily fluctuations in the laboratory temperature. To this end, it is useful to carry out a comparison of the results where the temperature is normalized. Figures 4.11c and 4.11d achieve this by plotting the dimensionless temperature over time for the experiments and the simulations, respectively. Once again, we observe that the modeling and experimental results agree fairly well for the agitated cases, but that the case for 0 rpm differs significantly. Finally, Figures 4.11e and 4.11f leverage these results to compute the heating time of the bed surface and the heat transfer coefficient, respectively. Once again, we see good agreement between the experiment and the simulation for agitated beds but inaccurate predictions for the static bed. More specifically, we found that the error between the modeling and the experimental heat transfer coefficient was 69.2%, 36.9%, 11.0%, 2.6%, 9.9% for 0 rpm, 5 rpm, 10 rpm, 25 rpm, and 100 rpm, respectively.

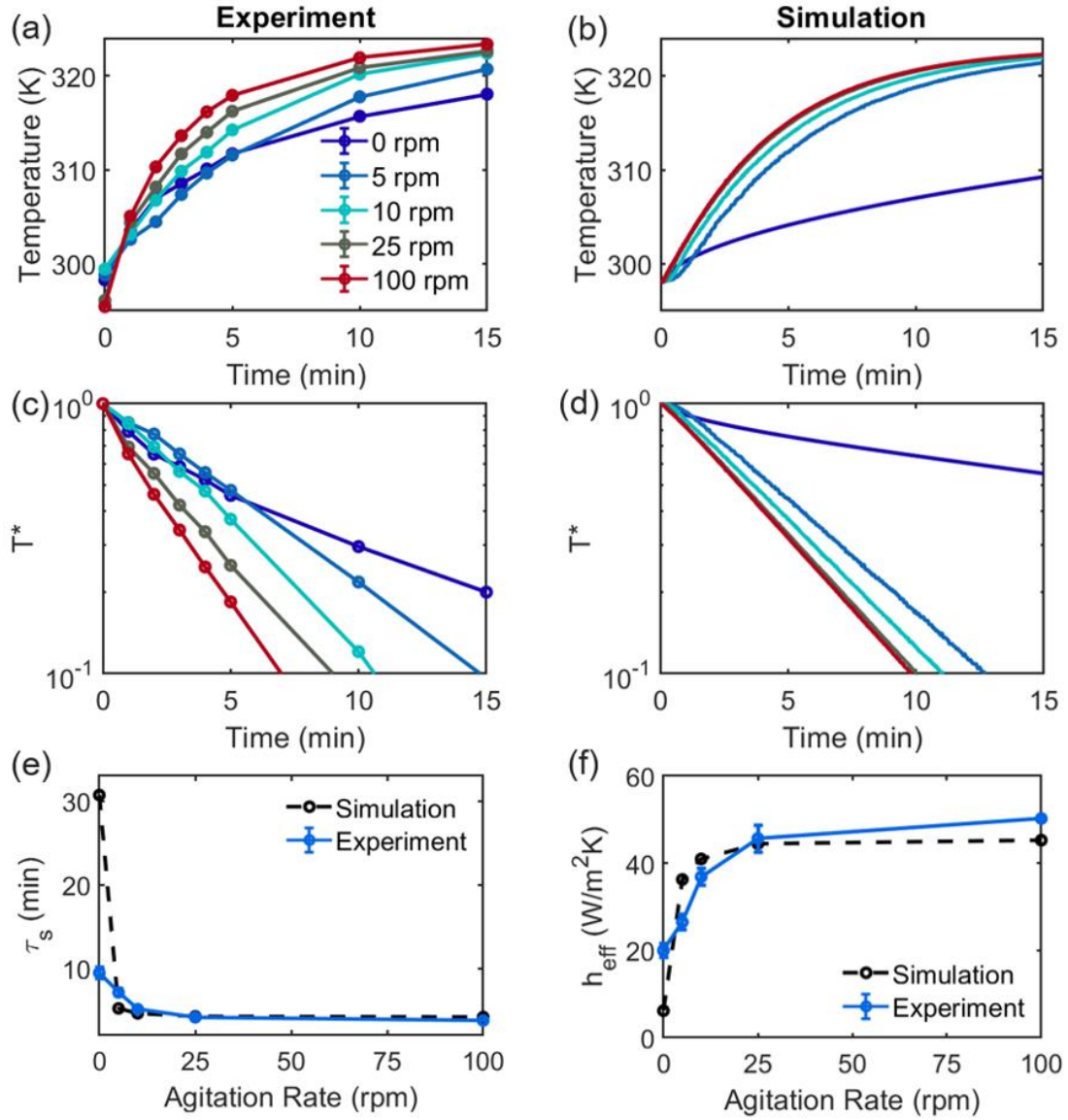


Figure 4.11: Comparison of the experimental and simulated results for different agitation rates: (a), (b) Mean temperature of the bed surface over time. (c), (d) Dimensionless temperature of the bed surface over time. (e) Heating time of the bed surface. (d) Heat transfer coefficient of the bed surface.

Next, we carry out a comparison of the heating uniformity. Figure 4.12 describes the standard deviation of the surface temperature over time for simulations and experiments with different agitation rates. Visually, the results for an agitated bed show similar

qualitative trends. For example, in both the simulations and the experiments, we notice that the standard deviation started at zero, rose and peaked after a few minutes, and then gradually decreased. The simulation for the case for 5 rpm agrees nearly perfectly with the experimental results: the standard deviation reaches approximately the same maximum, peaks at the same time, and decays at the same rate. The simulations for 10 rpm, 25 rpm, and 100 rpm tended to overpredict the temperature standard deviation compared to the experiment. The simulations also suggested that agitating at 100 rpm yields nearly the same heating uniformity as agitating at 25 rpm, whereas the experiment showed that agitating at 100 rpm would slightly decrease the temperature standard deviation. Overall, we feel that these results are still very encouraging. Despite these differences, for agitated beds, the model is able to predict the standard deviation within one 1 K. The temperature standard deviation for the case without agitation was so much larger than the cases for agitated beds that the data did not easily fit in Figure 4.12. The standard deviation for 0 rpm is therefore shown in Appendix A.2.

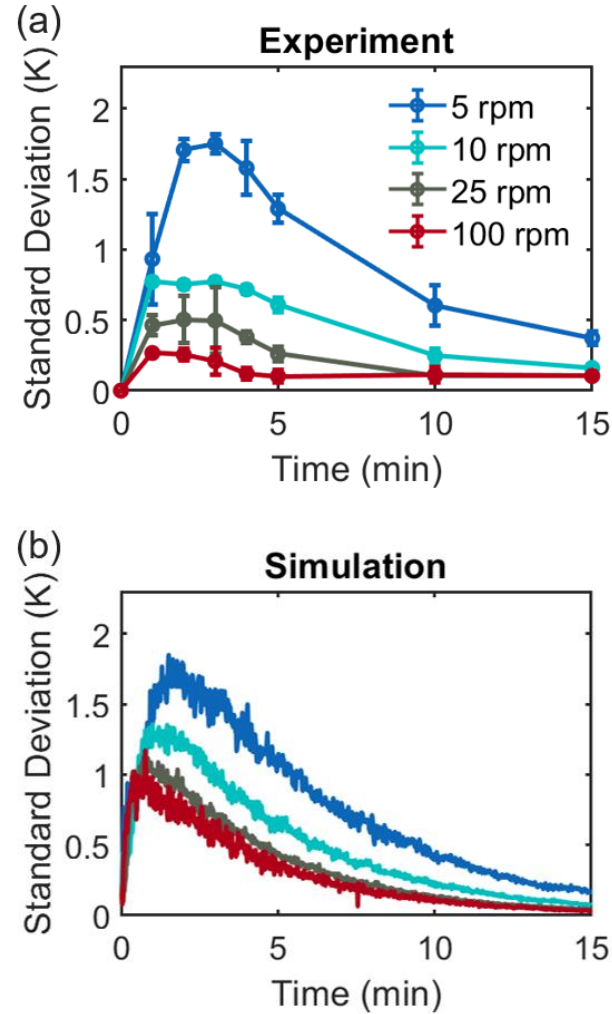


Figure 4.12: (a) Experimental standard deviation of the bed surface temperature over time for different agitation rates. (b) Simulated standard deviation of the bed surface temperature over time for different agitation rates.

4.3 Conclusions About Infrared Temperature Experiments and Validation of DEM Simulations

In this work, we carried out heating experiments using an infrared camera, glass beads, and a laboratory-scale agitated dryer. The goal of this work was to investigate the effect of the impeller agitation rate on the rate of heat transfer in the particle bed and the heating uniformity. In the pharmaceutical industry, agitated drying is known to cause

manufacturing challenges such as long cycle times as well as nonuniform drying. Better understanding how heat transfer occurs in a bladed mixer and how it is affected by the agitation rate could help optimize agitation protocols and improve both the cycle time and uniformity of the bed. Another aspect of this work was to carry out heat transfer DEM simulations and to compare the findings with the experiments. Simulations provide considerable benefits in that they are inexpensive, can provide data that may be difficult to obtain experimentally, and can shed valuable insights on the fundamentals of heat transfer in this geometry. The thermal properties in the model were calibrated according to the dimensionless scaling developed in Chapter 3. We then evaluated the effect of the agitation rate both visually and quantitatively. We computed the mean temperature of the bed surface, the heating time, the heat transfer coefficient, and the temperature standard deviation for 5 different agitation rates. A comparison of these results was then carried out to assess the validity of the model.

Despite the simplicity of our heat transfer model, we found fairly good agreement between the simulations and the experiments for the cases where the bed was agitated. The error between the experimental and simulation heat transfer coefficients was between 2% and 37% for all the agitated beds. The model was also able to predict the standard deviation of the bed surface within 1 K for all the agitated beds. However, the model did not perform as well for the static bed. We hypothesize that the reason for this is because static beds have a significantly different thermal conductivity than agitated beds. Overall, the flow behaviors for the cases between 5 rpm and 100 rpm are representative of the quasi-static regime, so we expect that the thermal conductivity between these beds does not vary as much. The results suggest that the thermal properties of the model may need to be

calibrated separately for a static bed. Overall, this work demonstrates that the model can serve as a good starting point towards better understanding how the rate of heat transfer and the temperature uniformity of a particle bed can be optimized in an agitated dryer.

This work also demonstrates how infrared imaging could be used as a PAT for measuring temperature in agitated drying processes. To our knowledge, the pharmaceutical industry typically relies solely on thermocouples to quantify temperature in their systems. Infrared imaging provides considerable advantages in that it is a nonintrusive method and it captures temperature data for an entire region, as opposed to a single point.

5. SCALE UP OF HEAT TRANSFER

Heated bladed mixers are commonly used to process and manufacture granular materials for a wide range of applications. Yet, despite their ubiquity, many unanswered questions remain regarding how heat is transferred through granular material in this geometry, particularly when scaling up the process. In this chapter, the discrete element method (DEM) is coupled with a heat transfer model to investigate how the fill level of the material and the size of the mixer influence the heating time of the particle bed. More specifically, the H/D and D/d ratios are varied to analyze the influence on the rate of heat transfer in the bed. The H/D ratio refers to the material fill height in the bed H versus the diameter of the vessel D . The D/d ratio represents the diameter of the vessel versus the average particle diameter d . These ratios are common metrics when considering the scale up of a process in a cylindrical vessel [78].

First, simulations are presented where the fill height of the material in the mixer is varied while keeping all other parameters constant. The results analyze how the fill height influences the heating time of the bed as well as other relevant factors such as the heating surface area of the mixer relative to the amount of material heated, the compression of the bed, and the rate of particle mixing. Next, simulations are presented where the size of the mixer is scaled up. Similarly, the results investigate the influence of the mixer diameter on the heating time of the bed, the heating surface area of the mixer relative to the amount of material heated, the compression of the bed, and the rate of particle mixing. Overall, the goal of this work is to enhance fundamental understanding of the elements at play during the scale up of granular processes in heated bladed mixers.

5.1 The Effect of the H/D Ratio

In this section, we demonstrate the influence of the H/D ratio on heat transfer in the mixer. The H/D ratio was studied by testing different fill levels in a laboratory-scale mixer with a set diameter. Figure 5.1 illustrates screenshots of particle beds with different H/D ratios at time = 100 s using an oblique view (Figure 5.1a) and a vertical cross-section view (Figure 5.1b). Figure 5.1a shows that for all bed fill levels, the warmest regions of the bed were near the side walls and bottom of the vessel, which was expected because heat was supplied by the walls, while the core of the bed near the shaft of the impeller was the coldest region. Overall, the size of the cold core increased with the H/D ratio. For $H/D = 0.42$ (shallow bed), after 100 seconds of heating, most particles at the surface of the bed heated up relatively uniformly and had temperatures approaching T_w . For $H/D = 2.23$ (deep bed), after 100 seconds of heating, most of the particles at the surface of the bed still had temperatures around T_0 . Particles located at the surface heated up in a pattern of concentric rings with different temperatures and demonstrated a strong temperature gradient in the radial direction. Beds with H/D ranging between 0.42 and 2.23 showed a gradual progression from one extreme to the other.

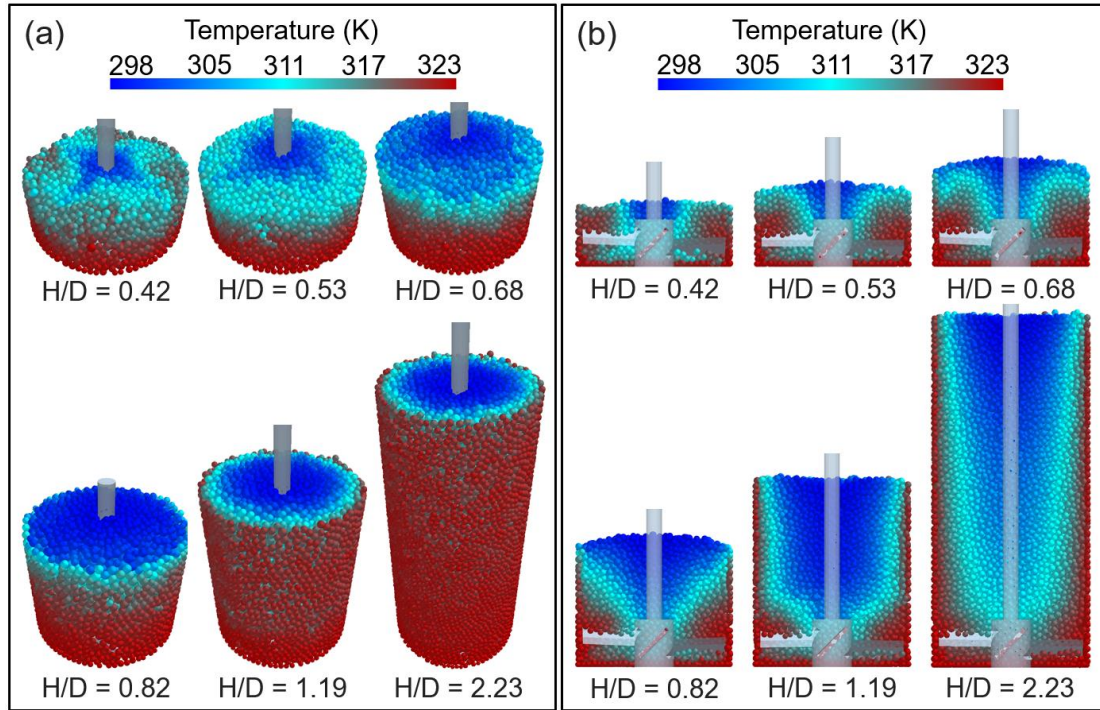


Figure 5.1: (a) Oblique view and (b) side cross-section view of particle beds with different H/D at time = 100 s.

Figure 5.1b adds another layer of information by enabling us to visualize how heat transfer occurs inside the beds. Once again, we observed that particles located near the side walls and the bottom of the vessel were warmer overall, while particles located near the center and the surface of the bed were relatively colder. An interesting feature shown by the cross-section view is the shape of the temperature gradient inside the beds. For the shallowest bed ($H/D = 0.42$), we notice that the impeller blades induced a recirculation pattern that was visible in the temperature of the particles. This is because the impeller blades have an obtuse angle and as the blades rotated through the bed, they lifted hot particles from the bottom and brought them to the surface. The displacement of particles left a void behind the blades and allowed cold particles from the surface to slide down towards the bottom of the bed in order to fill that void. Literature reports that

recirculation patterns are a well-known phenomenon in bladed mixers [75, 101], however, we demonstrate here how the recirculation affects heat transfer in the bed. Interestingly, we observed that the shape of the temperature gradient changed with the H/D ratio. In this geometry, as the H/D ratio increased, the temperature gradient went progressively from circular vortices to a V-shape and to a U-shape. Remy *et al.* [78] report that the size and intensity of the recirculation in front of the blades depends on the mixer fill height. They found that shallow beds have more prominent recirculation patterns due to the formation of large heap and valleys at the surface. By contrast, they found that heap formation decreases for higher fill levels and that deeper beds therefore exhibit diminished recirculation patterns. We hypothesize that the temperature patterns observed in Figure 5.1b reflect the changes in recirculation occurring as a function of the fill level.

The images shown in Figure 5.1 not only provide an interesting visualization of how heat transfer occurs in a bladed mixer but could also help guide experimental setup. For example, an important takeaway from Figure 5.1 is that the beds do not heat up uniformly, and that the degree of uniformity is influenced by the fill height. This means that if one were to measure temperature in a heated bladed mixer using a thermocouple, they would need to be careful with how the probe is positioned in the bed. Figure 5.1 shows that the beds have strong temperature gradients both in the radial and vertical directions, so positioning the probe slightly closer to the center or slightly higher in the bed could significantly affect the temperature reading. One way of assessing the uniformity of the bed could be to use an array of thermocouples placed at different radial

and vertical positions in the bed, and to potentially use Figure 5.1b as a guide for deciding those locations.

Next, we quantify the results in Figure 5.1. Figure 5.2a shows the mean temperature profile of the beds over time for different fill levels. As expected, the mean temperature of the shallowest bed ($H/D = 0.42$) approached the wall temperature the fastest. For beds with a H/D ratio ranging from 0.76 to 1.19, the results indicate that higher fill levels made the mean temperature of the beds increase more slowly. Surprisingly, Figure 5.2a suggests that for very deep beds ($H/D > 1.19$), adding more material led to faster heat transfer. For example, the mean temperature of the bed with $H/D = 2.23$ approached the wall temperature more rapidly than the bed with $H/D = 1.19$. This phenomenon can also be seen in the simulation screenshots depicted in Figure 5.1b. In Figure 5.1b, we see that the bed with $H/D = 2.23$ had overall higher particle temperatures (mostly light blue particles) than the bed with $H/D = 1.19$ (mostly dark blue particles) after 100 s. This result was not intuitive to us, and thus, we conducted a more thorough analysis (Figures 5.2b to Figure 5.6) to better understand this unexpected trend. It is important to note that most industries typically use shallow or intermediate H/D ratios in their processes and would therefore rarely deal with a case with a H/D ratio above 1.19. However, upon noticing the surprising trends in heat transfer for beds with high H/D ratios, we chose to expand our study and include a few very deep beds for educational purposes.

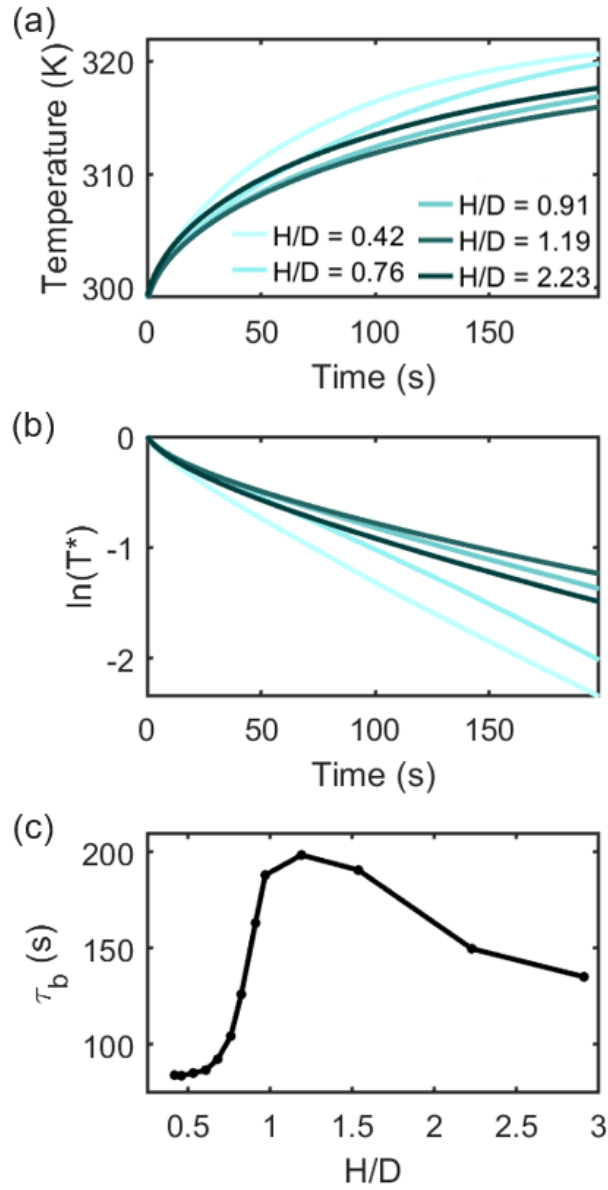


Figure 5.2: (a) Mean temperature over time for beds with different H/D. (b) Dimensionless temperature over time for beds with different H/D. The legend in Figure 5.2a also applies to Figure 5.2b. (c) Relationship between the heating time τ_b and H/D.

An alternative method of quantifying the results in Figure 5.2a is to calculate the heating time of the bed, which we define as τ_b . Depending on the application, the heating time of the bed can be a critical parameter for the manufacturing process. For example, in

agitated drying of pharmaceuticals, processing times can sometimes be up to an order of magnitude longer than other operations in the sequence which can cause a bottleneck [63]. Computing the heating time for each bed allows us to easily compare simulation conditions and their effect on heat transfer. A long τ_b time means that the bed requires a long time to heat up to the wall temperature, while a short τ_b means that the bed heats up rapidly. As in Chapter 3, the heating time is calculated using Equation 5.1 [43]:

$$\ln(T^*) = -\frac{h_{eff}A}{MC_p}t = -\frac{t}{\tau_b}, \text{ where } T^* = \frac{T_w - \bar{T}_b}{T_w - \bar{T}_{b,0}} \quad (5.1)$$

where T^* is the dimensionless temperature, T_w is the wall temperature, \bar{T}_b is the mean bed temperature, $\bar{T}_{b,0}$ is the initial mean bed temperature, h_{eff} is the effective heat transfer coefficient between the vessel and the bed, A is the heated surface area of the vessel in contact with the bed (which includes the side walls and the base), M is the mass of the bed, C_p is the specific heat capacity of the bed, and t is time. τ_b is therefore a lumped parameter that serves as an approximation for the heating time of the bed. More specifically, it is the time required for the difference between T_w and \bar{T}_b to drop by 63.2% of the initial difference $(T_w - \bar{T}_{b,0})$. τ_b is calculated by plotting the natural logarithm of the dimensionless temperature versus time, as shown in Figure 5.2b, and taking the negative inverse of the slope of the line. Figure 5.2c depicts the heating time of the bed τ_b as a function of H/D. The results provide valuable information that quantifies how selecting the fill height of the material can influence the heating time of the bed. For the parameters studied, we find that doubling the fill height from H/D = 0.4 to 0.8 led to an approximately 30% longer heating time. Increasing the fill height from H/D = 0.8 to 1.2 led to an approximately 85% longer heating time. This kind of information could be beneficial when

designing a drying protocol and determining how much material to put in the mixer to optimize the heating time.

Figure 5.2c also confirms the unexpected finding in Figure 5.2a, where very deep beds ($H/D > 1.19$) were found to have a decrease in heating times. While this phenomenon seems counterintuitive, Figures 5.3-5.6 show that the relationship between fill height and heat transfer for these parameters in this geometry is not trivial. As the fill height is varied, multiple variables change simultaneously and influence the rate of heat transfer. Notably, we identified three important factors: (1) the heating surface area of the vessel relative to the mass of material being heated, (2) the bed compression, and (3) the mixing rate.

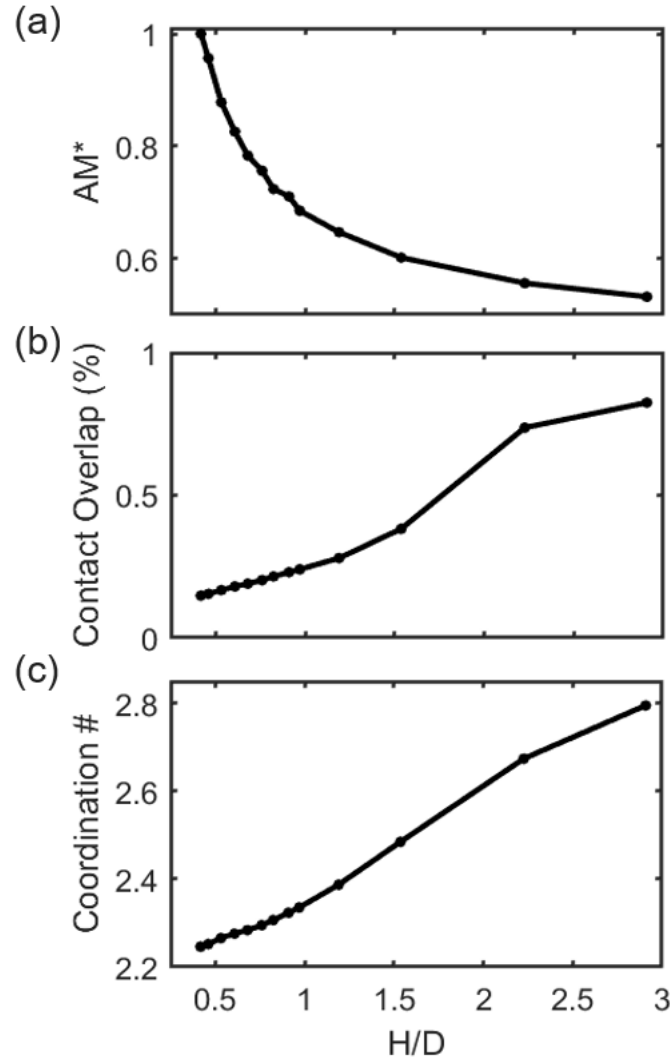


Figure 5.3: Relationship between H/D and (a) AM^* ratio of the heated surface area A of the vessel to the mass M of material normalized over the area A_{shallow} and mass M_{shallow} for a shallow bed, (b) normalized mean % contact overlap between particles in the bed, (c) mean coordination number in the bed.

First, we discuss the influence of the surface area to mass ratio. As the fill level is varied, both the amount of material M and the surface area A in contact between vessel and the bed change. Equation 5.1, described previously, suggests that these two factors have opposite effects on the rate of heat transfer: increasing the heating surface area

decreases the heating time, while increasing the mass of material increases the heating time. It is therefore important to consider the ratios of these two factors and see how they change with respect to H/D. To do so, we define a normalized dimensionless ratio AM^* using Equation 5.2:

$$AM^* = \frac{A/M}{A_{shallow}/M_{shallow}} \quad (5.2)$$

where A is the heating surface area in contact between the vessel and the bed, M is the bed mass, $A_{shallow}$ is heating surface area of the shallowest bed ($H/D = 0.42$), $M_{shallow}$ is the mass of the shallowest bed ($H/D = 0.42$). Figure 5.3a shows that AM^* decreases with increasing H/D. This means that even though we have a larger heating surface area when we increase the fill level, the resulting increase in material mass is more significant. If considered as a factor on its own, the results in Figure 5.3a suggest that heat transfer should decrease with increasing H/D.

Next, we discuss the influence of the compression of the bed. Increasing the fill height of the material increases the hydrostatic pressure in the bed [69]. Deeper beds have greater hydrostatic pressure due to the extra weight of material and therefore tend to be overall more compressed than shallow beds. One of the metrics that can be used to quantify compression in the bed is the contact overlap between particles, which is the theoretical deformation that occurs when two soft spherical particles are pressed together [92]. Equation 2.14 from Chapter 2 states that the heat conductance between particles is proportional to the contact overlap such that greater compression in the bed should result in faster heat transfer. Figure 5.3b depicts the relationship between the mean normalized % contact overlap in the bed and the H/D ratio. The mean normalized % contact overlap was obtained by computing the average particle contact overlap in the bed and dividing it

by the mean particle diameter. As expected, Figure 5.3b shows that increasing the fill height increased the mean contact overlap between particles. If considered as a factor on its own, the trend in Figure 5.3b suggests that heat transfer should increase with increasing H/D .

As is often the case in DEM simulations, the input value for the Young's modulus used in these simulations was softer than that of real glass beads to reduce the computational cost [94]. Since the Young's modulus affects the contact overlap, and the heat conductance between the particles (Equation 2.16), we expect that this may affect the results. We therefore conducted additional simulations where we varied the particle stiffness (see Appendix A.3). We found that the rate of heat transfer is faster for softer particles (as would be expected) but that the overall trends between the heating time of the bed and the H/D ratio are similar for the different material stiffnesses studied.

Another factor that changes due to the compression of the bed is the number of particle contacts in the bed. Equation 2.18 from Chapter 2 indicates that the number of particle contacts N in the bed is an important factor for heat transfer in a granular material. Heat conduction occurs when particles with different temperatures come into contact and exchange thermal energy. If more of these contacts happen, the heating time decreases. One way of comparing the number of contacts in different beds involves calculating the coordination number, which is the number of touching neighbors for an individual particle. Figure 5.3c shows that the average coordination number in the bed increased with increasing H/D . This is important in heat transfer because conduction is the sum of heat exchanged by all particles in contacts, so beds with higher coordination numbers will have greater conductivity. If this factor was considered on its own, the trend

in Figure 5.3c suggests that heat transfer should increase with increasing H/D . When considered together, the results in Figures 5.3a, 5.3b, and 5.3c demonstrate that several factors contribute to heat transfer in this geometry and that the relationship with H/D is not trivial. The factors compete to improve or hinder the rate of heat transfer and start to explain the unexpected trends illustrated by Figure 5.2c.

Figures 5.3b and 5.3c showed that beds with higher fill heights not only had greater mean particle overlaps, but also had higher mean coordination number. Next, we illustrate how these effects influenced the particle temperatures visually. In Figure 5.4, cross-sectional horizontal slices of the bed were taken right above the impeller blades to show the influence of H/D on particle temperatures after 100 seconds of heating. We observed that overall, the average temperature of the particles in the slice right above the impeller blades increased with the H/D ratio. For example, for a shallow bed ($H/D = 0.53$), the particles located in the slice above the blades had temperatures ranging from 298 K to 318 K at that time point. For a deep bed ($H/D = 1.54$), the corresponding particles had temperatures ranging from 301 K to 323 K due to the increased contact overlaps and number of contacts in the bed. This result suggests that the greater compression in deep beds improves heat transfer in the region particularly near the impeller blades.

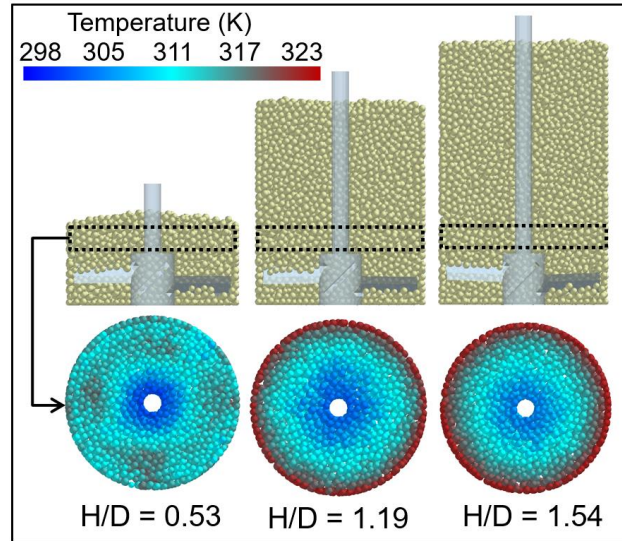


Figure 5.4: Horizontal slides of the bed right above the blades ($H = 3.0$ cm) at time = 100 s. Slices are shown for a shallow bed, an intermediate bed, and a deep bed.

Finally, another important factor that changes with H/D is the rate and extent of mixing. Mixing improves uniformity of the bed, which is important when considering heat transfer because it allows for hot particles located near the side walls and bottom of the vessel to move throughout the bed and distribute their thermal energy by exchanging heat with colder particles. Figure 5.5 illustrates visually how mixing changes with fill height. The rows of the figure display a shallow bed ($H/D = 0.53$), an intermediate bed ($H/D = 1.19$), and a deep bed ($H/D = 1.54$). The columns of the figure depict the respective beds after a certain number of impeller revolutions (0.5, 2, and 10 revolutions). At time = 0 (or 0 revolutions), the beds were divided into two vertical sections and the particles were color-coded either red or gray depending on their position. The results indicate that the shallow bed ($H/D = 0.53$) was mixed relatively rapidly and became mostly uniform after 10 impeller revolutions. For beds with $H/D = 1.19$ and $H/D = 1.54$, we observed two prominent regions: a well-mixed zone near the span of the impeller blades and a mixing dead zone at the top of the bed where the particles remained static.

For the parameters simulated, we found that the boundary between the mixing zone and the static region occurred around $H/D = 0.82$.

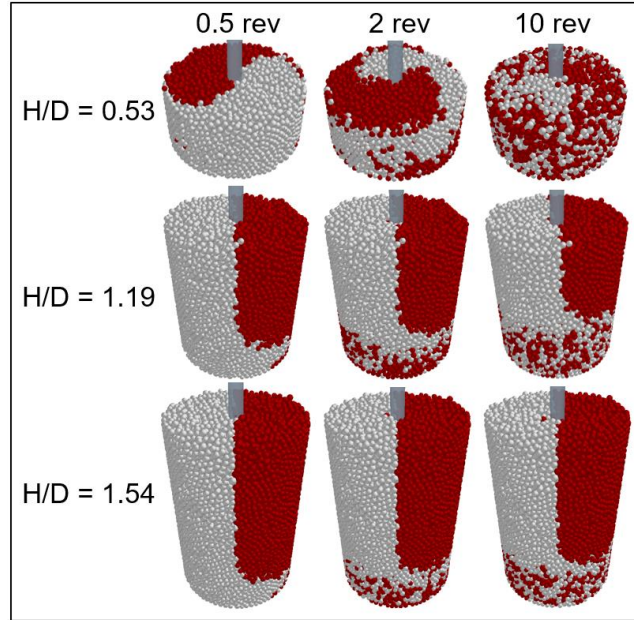


Figure 5.5: Visuals for beds with $H/D = 0.53$, 1.19 , and 1.54 after 0.5 , 2 , and 10 revolutions. Particles are color-coded dark red and gray at time = 0 s to show particle mixing over time.

Next, we computed the relative standard deviation in the bed and used it as a metric to quantify mixing as a function of the number of impeller revolutions for different fill levels. The relative standard deviation (RSD) was calculated using Equation 5.3 [78, 102]:

$$RSD = \frac{\sigma_{conc}}{\mu_{conc}} \quad (5.3)$$

where σ_{conc} is the standard deviation of the red particles over all the sampled grid cells, and μ_{conc} is the mean concentration of red particles. An RSD value equal to one means that the bed is perfectly segregated, while a low RSD value means that the bed is well mixed. The grid was based on cartesian coordinates. The sample grid was determined by

testing different cell sizes until the RSD value was found to be independent of sampling grid. The grid size was based on the work of Remy *et al.* [78]. Figure 5.6 enables quantification of the results displayed by Figure 5.5 and provides an insight into both the rate of mixing and the extent of mixing for beds with different fill heights. Initially, the gray and red particles are segregated in all the beds ($RSD = 1$). As time progressed and the impeller blades moved through the material, the particles were displaced and mixed such that the relative standard deviation decreased, and the beds gradually became more uniform. Interestingly, the RSD for all beds appeared to decrease linearly for the first 1.5 impeller revolutions. After that, the rate of mixing appeared to slow down, particularly for the deeper beds. For beds with $H/D = 1.19$ and 1.54 , we observed that the RSD seemed to approach a plateau over time. We presume that the reason for the plateau is because the upper portion of the bed was too far from the span of the impeller blades and therefore remained relatively stagnant. Interestingly, we found that beds with H/D ratios between 0.46 and 0.82 had similar mixing rates and that the mixing rates are slower for beds with $H/D > 0.82$. Visually, we noticed in the simulations that particles above $H/D = 0.82$ were in a mixing dead zone. Similarly, Figure 5.2c showed that the heating time drastically increases around $H/D = 0.82$. This seems to indicate that the location of the boundary between the well-mixed and stagnant region is an important factor in determining the heating time of the bed. Overall, Figure 5.6 corroborates the results found in Figure 5.5 and confirms that shallow beds mix more rapidly than deeper beds. Since mixing helps improve heat transfer by promoting temperature uniformity in the bed, the results in Figures 5.5 and 5.6 suggest that heat transfer should decrease with H/D if considered as a factor on its own.

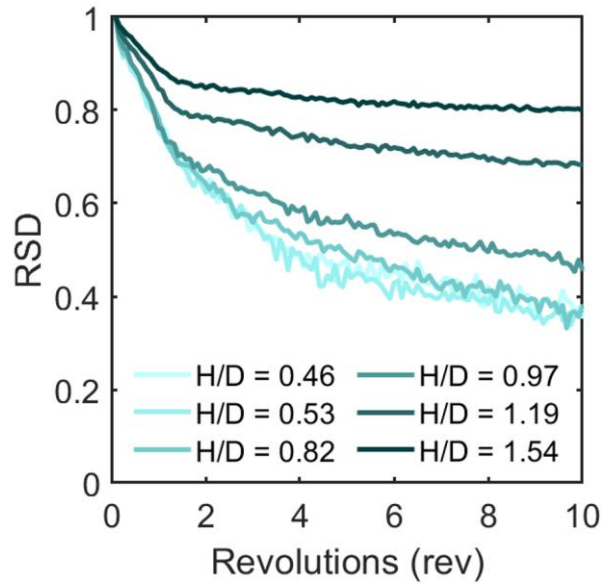


Figure 5.6: Relative standard deviation as a function of impeller revolutions for different bed heights.

When considered together, the results shown in Figures 5.2 through 5.6 demonstrate the complexity of the relationship between the H/D ratio and the rate of heat transfer and show that numerous factors play a role. In our system, varying the fill height led to changes in heating surface area relative to material mass (Figure 5.3a), bed compression (Figures 5.3b, 5.3c, 5.4), and mixing (Figure 5.5, 5.6), all of which compete to influence heat transfer in the bed. Some factors improved heat transfer (i.e.: greater bed compression), while others decreased heat transfer (i.e.: poor mixing, less heating surface area relative to mass of material). Together, they provide an explanation for the complicated relationship between the H/D ratio and the heating time τ_b shown in Figure 5.2c. For the tested parameters and geometry, it appears that the contribution from the mixing and surface area factors dominate for shallow beds ($H/D < 1.19$), while the contribution from the compression factor dominates for deeper beds ($H/D > 1.19$). Most industries typically operate using shallow or intermediate H/D ratios in their processes so

the results for very deep beds result may not be representative of real applications but remain an interesting phenomenon.

5.2 The Effect of the D/d Ratio

In this section, we investigate the effect of the D/d ratio on heat transfer through dry granular material in a vertical cylindrical bladed mixer. The D/d ratio was studied by varying the vessel diameter D while keeping the particle diameter d constant. The vessel dimensions listed in Table 2.1 in Chapter 2 represent the smallest vessel we tested, which describe a laboratory-scale vessel with a D/d ratio of 25.0. The larger vessels we simulated were linear scale ups of the laboratory-scale vessel. More specifically, the dimensions of the vessels with D/d = 37.5, 50.0 and 62.5 had 1.5x, 2.0x, and 2.5x times the dimensions of the small vessel in Table 2.1. The only dimension parameter that was kept constant across the different vessels was the size of the gap below the impeller blades. This method of studying scale up using the D/d ratio in a bladed mixer is consistent with previous work carried out by Remy *et al.* [78].

Figure 5.7a and 5.7b depict images of beds with four different D/d ratios at time = 100 s using an oblique view and a side cross-section view, respectively. The particles were color-coded according to their temperature. Figure 5.7a shows that overall, the particles in the smallest bed (D/d = 25.0) heated up rather quickly and uniformly. After 100 s of heating, most of the particles in that bed had temperatures approaching T_w , while a small core of cold particles remained in the center of the bed near the impeller shaft. By contrast, the particles in the largest bed (D/d = 62.5) heated up the slowest and with poor uniformity. After 100 s of heating, approximately half of the particles in the bed still had

temperatures near T_0 , while only a few particles had particles approaching T_w . The intermediate particle beds ($D/d = 37.5, 50.0$) had heating behaviors in between the smallest and the largest bed. Overall, the visuals indicate that the size of the cold core of particles near the center of the bed increased with the vessel diameter.

Another prominent observation is the shape of a cross-like pattern at the surface of the bed. This was also observed in some of the beds in Figure 5.1a. The pattern is due to shape of the impeller blades. The impeller blades have an obtuse angle and as they pass through the bed, they lift hot particles from the bottom of the vessel towards the surface. Cold particles at the surface then flow down the void left behind each blade, creating an interesting temperature pattern at the surface of the bed. We conducted preliminary work (not shown) using a different number of impeller blades to confirm this hypothesis. Indeed, we observed that the number of “branches” at the surface reflects the number of impeller blades (i.e.: a 4-bladed impeller created a pattern with 4 branches; a 2-bladed impeller created a pattern with 2 branches). This temperature pattern may be important to know when conducting an experiment. For example, if one were to measure the surface temperature of a bed by using a thermocouple, the radial placement of the probe may influence the data collected. One must therefore be careful before assuming that the surface of the bed has a uniform temperature.

Figure 5.7b shows a side cross-section view of each bed at time = 100 s. Once again, we notice that the larger beds had a greater number of cold particles near the impeller shaft, compared to the smaller beds. If this were observed experimentally, it could make a strong case for using a heated impeller in larger vessels to improve heat transfer in the center of the bed. We also notice another interesting temperature pattern

due to the recirculation of particles occurring around the impeller blades. The recirculation pattern was previously addressed in the discussion of Figure 5.1b.

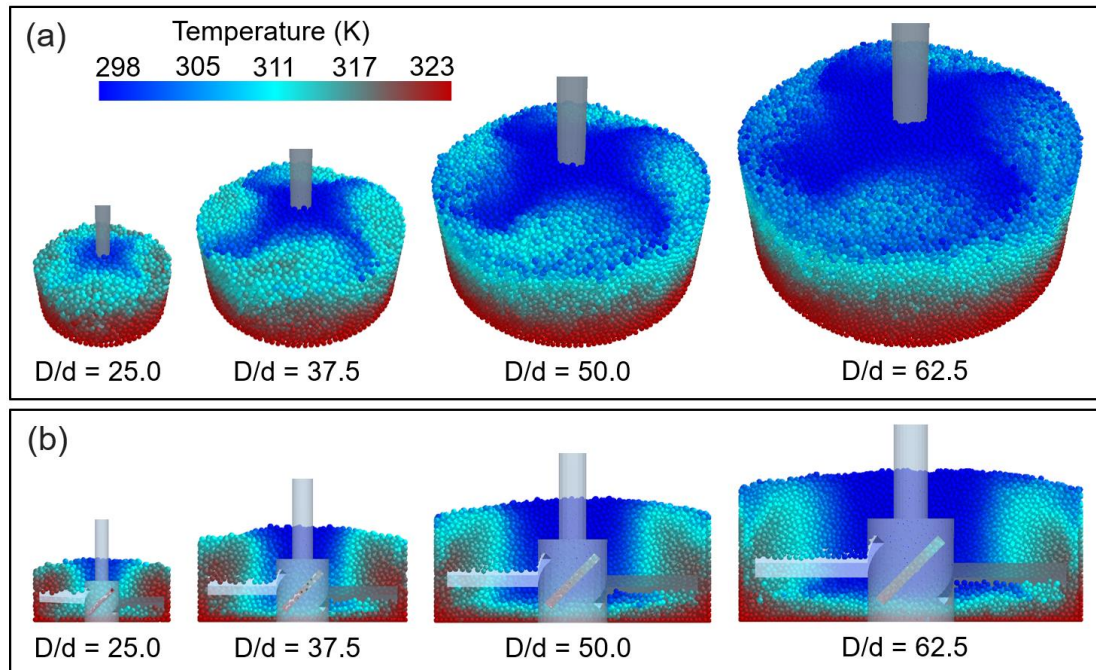


Figure 5.7: (a) Oblique view and (b) Side cross-section of beds with different D/d at time = 100 s. The legend in Figure 5.7a is also applicable to Figure 5.7b.

Next, we sought to quantify the results depicted by Figure 5.7. Figure 5.8a shows the mean temperature over time for beds with different D/d ratios. Additionally, the plot illustrates the influence of no agitation (dashed lines) compared to an agitation rate of 5 rpm (solid lines). For both agitation rates, the mean temperature of the beds increased more slowly for beds with greater D/d ratios. Figure 5.8b further supports this result by showing the relationship between the heating time τ_b of each bed and the D/d ratio (refer to Section 5.1 for a description of how τ_b was calculated). Overall, Figure 5.8b shows three significant findings: (1) the heating time of the bed is proportional to the D/d ratio, (2) the constant of proportionality constant has an order of magnitude of one, and (3) the constant of proportionality depends on the agitation rate of the impeller. For linear scale

up (i.e., D and H increase proportionally), we find that the heating time τ_b scales linearly with the vessel diameter D , such that we can obtain an equation relating the heating time and the vessel diameter: $\tau_b = cD$, where c is the constant of proportionality.

Interestingly, we find that for the parameters studied, the value of c has an order of magnitude of 1 and is a function of the agitation rate. This kind of analysis can provide valuable information for estimating the heating time during scale up of the process. For example, for the case with 5 rpm agitation rate, we find that if we double the mixer diameter, the heating time approximately doubles. For the case with 0 rpm, we find that if we double the mixer diameter, the heating time approximately triples.

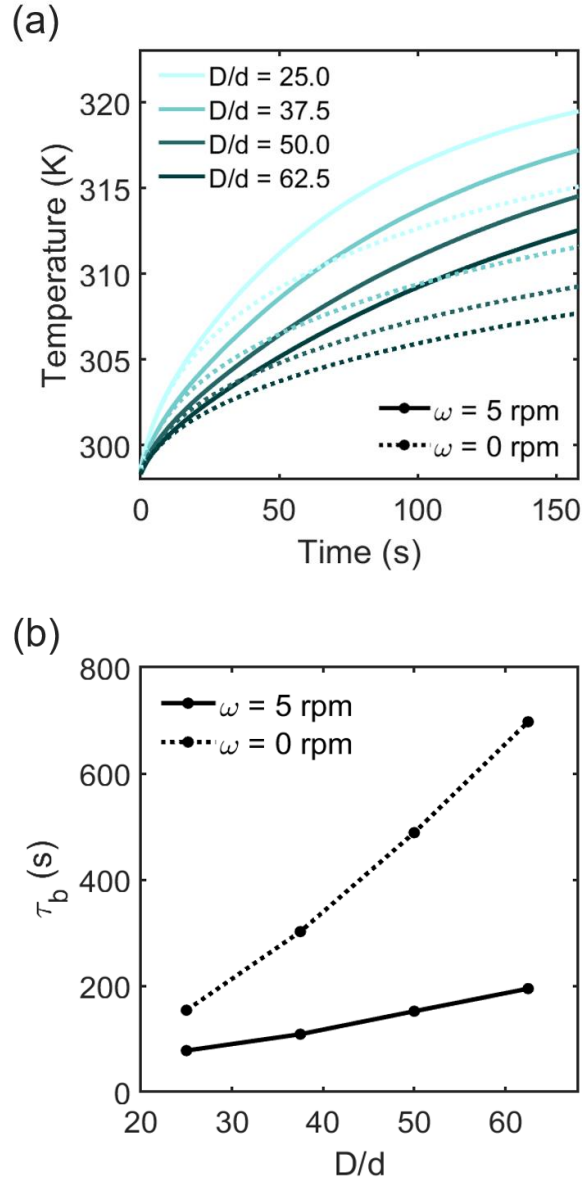


Figure 5.8: (a) Mean temperature over time for beds with different D/d (colors) and different agitation rates (solid or dotted line). (b) Heating time as a function of D/d for two different agitation rates.

Given that the relationship between heat transfer and the H/D ratio was rather complex, it was not obvious to us that the relationship between the heating time and the D/d ratio would be straight-forward. We therefore conducted a similar analysis to Section 5.1 and investigated the how D/d ratio affects the AM^* ratio, the mean % contact overlap,

the mean coordination number, and the RSD. The AM^* ratio was previously introduced by Equation 5.5 and describes the heating surface area of the vessel relative to the bed mass. As we scale up the process, we change both the vessel size (and therefore the heating surface area) as well as the mass of material that needs to be heated. Equation 5.1 suggests that both parameters influence heat transfer, so it is important to understand how they change during scale up. Figure 5.9a shows that the AM^* ratio decreases sharply with the D/d ratio, meaning that the increase in heating area resulting from scaling up is not as large as the resulting increase in the mass of material. If considered as a factor on its own, the result in Figure 5.9a suggests that increasing the D/d ratio leads to a decrease in heat transfer.

Figure 5.9b and Figure 5.9c illustrate the relationship between the D/d ratio and the mean normalized % contact overlap in the bed and the mean coordination number in the bed, respectively. The method used to compute these variables has been previously described in the discussion for Figure 5.3b and 5.3c. Figures 5.9b and 5.9c show that both the % contact overlap and the coordination number increase slightly with increasing D/d . This is because the H/D ratio was set to 0.44 for all the D/d cases studies, so the fill height of the larger vessel was higher than that of the small vessel. However, when looking at the range of the y-axis, one notices that the increase in % contact overlap and coordination number is relatively small.

Next, we evaluated the influence of the D/d ratio on mixing by computing the RSD of each bed using Equation 5.3. Figure 5.9d shows that the beds had similar RSD values over time, suggesting that the rate of mixing was fairly independent of the D/d ratio. These findings corroborate the results found in Remy *et al.* [78]. Finally, Figure

5.10 shows screenshots of beds with different D/d ratios after 0.5, 2, and 10 impeller revolutions. The visuals agree with the results in Figure 5.9d, confirming that changing the D/d ratio did not lead to a substantial change in mixing of the particles.

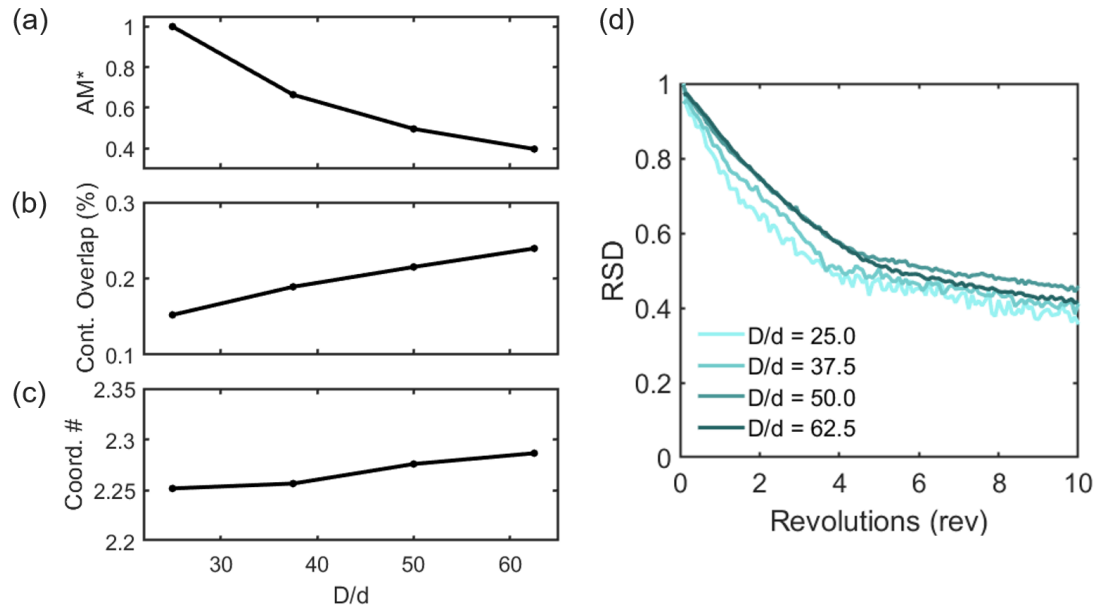


Figure 5.9: Relationship between the D/d ratio and: (a) AM^* ratio of the heated surface area A of the vessel to the mass M of material normalized over the area $A_{shallow}$ and mass $M_{shallow}$ for a shallow bed, (b) normalized mean % contact overlap between particles in the bed, (c) mean coordination number in the bed, (d) relative standard deviation as a function of impeller revolutions.

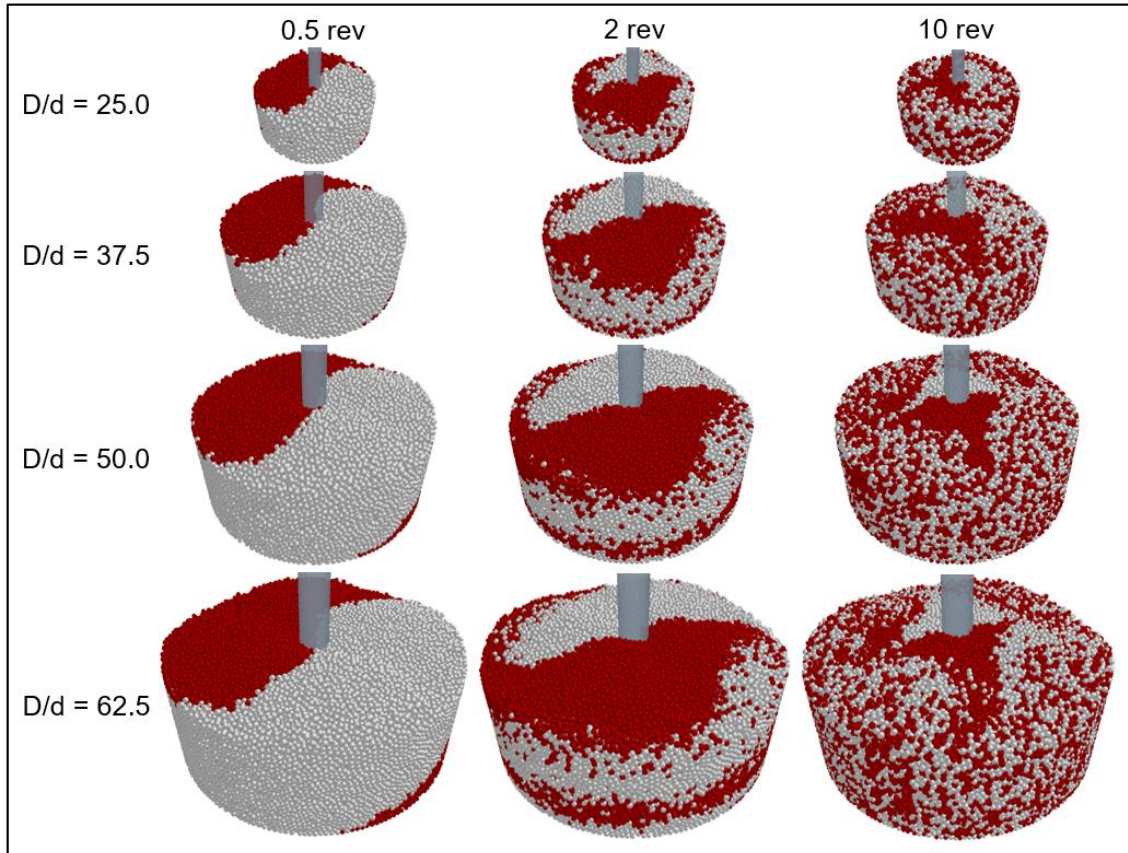


Figure 5.10: Visuals for beds with $D/d = 25.0$, 37.5 , 50.0 , and 62.5 after 0.5, 2, and 10 revolutions. Particles are color-coded dark red and gray at time = 0 s to show particle mixing over time.

Overall, for the range of D/d studied, the results suggest that scale up of the process did not influence the mean % contact overlap, the mean coordination number, or the mixing enough to significantly affect the rate of heat transfer. We therefore conclude that the increase in heating time with respect to D/d was largely due to the sharp decrease in the AM^* ratio as we scaled up. We also obtain the same conclusion if we rewrite Equation 5.1 and substitute the parameters for the surface area and the mass:

$$\tau_b = \frac{M * C_p}{A * h_{eff}} = \frac{\left(\pi \left(\frac{D}{2}\right)^2 H * \rho\right) * C_p}{\left(\pi \left(\frac{D}{2}\right)^2 + 2\pi \left(\frac{D}{2}\right) H\right) * h_{eff}} \quad (5.4)$$

For linear scaling, $H = bD$, where “ b ” is a constant. When substituting H in Equation 5.4, we get $\tau_b \sim D$. This supports the finding that heat transfer scales linearly with the diameter of the vessel ($\tau_b = cD$).

5.3 Conclusions About Scale Up of Heat Transfer

In this study, we coupled DEM modeling with a particle-to-particle heat transfer model to acquire a deeper fundamental understanding of how heat transfer scales in a bladed mixer for dry cohesionless granular material. Heated bladed mixers are widely implemented across numerous industries, so improving knowledge of scale up of the process could significantly aid in creating robust operating protocols driven by scientific principles. Scale up was modeled by varying the H/D ratio and the D/d ratio, which are common industrial variables considered in operating protocols. In the simulations investigating beds with different H/D ratios, we found that the relationship with heat transfer was nontrivial, due to the numerous competing factors that contributed to heat transfer. More specifically, we observed that the AM^* ratio decreased with increasing H/D , meaning that the relative increase in heating surface area due to the higher fill heights was less significant than the resulting increase in the mass of material that needed to be heated. When considered on its own, the trend suggested that adding more material should lead to longer heating times. Similarly, the rate of mixing was found to decrease with increasing H/D , due to the formation of a mixing dead zone for deep beds. Since mixing promotes temperature uniformity in the bed, the results also indicated that

increasing the fill height should lead to longer heating times. In contrast, however, it was observed that the mean normalized % contact overlap between the particles and the mean coordination number in the bed increased with increasing H/D and led to faster heating in deeper beds, particularly near the span of the impeller blades. Together, the results indicated a complicated trend between the H/D ratio and the rate of heat transfer.

The simulations analyzing different vessel sizes showed a simpler trend between the D/d ratio and heat transfer. The results suggested that the heating time and the D/d ratio had a positive and linear correlation. An analysis of the parameters relevant to heat transfer was conducted, investigating the mean normalized % contact overlap, the mean coordination number, the RSD, and the AM^* ratio. It was found that the % contact overlap and the coordination number changed slightly as a result of the slight increase in fill level but that this increase was not enough to significantly influence heat transfer. Similarly, the RSD revealed that there was no substantial change in mixing. The AM^* ratio was therefore found to be the main driving factor influencing heat transfer. As the D/d ratio was scaled up, the AM^* ratio decreased considerably, leading to remarkably longer heating times. Overall, we found that the heating time of the bed is proportional to the diameter of the vessel, that the proportionality constant is order one, and that the value of the constant is a function of the impeller agitation rate.

6. CONDUCTION AND GRANULAR CONVECTION

A useful aspect of simulations is that they allow us to can look at quantities that would be difficult or impossible to examine experimentally. In this chapter, we dive deeper into the theory of heat transfer through granular material. More specifically, we carried out DEM simulations to better understand how conduction and granular convection occur in a bladed mixer. Conduction and convection were computed as vector quantities, which provided insight into the directional component of heat transfer in this geometry. We also studied how different material properties and operating conditions affected each mode of heat transfer. The analysis allowed us to investigate how much of the heating came from particle contacts and how much was contributed by the mixing.

6.1 Heat Transfer Through Conduction

Thermal conduction is the process by which solids with different temperatures transmit heat through an area of contact. In this section, we sought to better understand the micromechanics of heat transfer through particle contacts in a bladed mixer by calculating the conductive flux in the different vector directions (R, θ, Z). The particle-to-particle conduction flux is given by Equation 6.1 [87]:

$$\vec{Q}_{cond} = \frac{1}{\Omega} \sum_{ij}^{N_c} \Phi_{ij} \vec{r}_{ij} \quad (6.1)$$

where \vec{Q}_{cond} is the conductive flux density, Ω is the bed volume, N_c is the total number of contacts, Φ_{ij} is the heat flux for the contact between particles i and j , and \vec{r}_{ij} is the center-to-center contact vector for the contact between particles i and j . The center-to-

center contact vector for the radial, theta, and vertical direction are given by Equations 6.2a, 6.2b, and 6.2c, respectively.

$$r_{ij,R} = \sqrt{(R_i - R_j)^2} \quad (6.2a)$$

$$r_{ij,\theta} = \sqrt{2R_i R_j * (1 - \cos(\theta_i - \theta_j))} \quad (6.2b)$$

$$r_{ij,Z} = \sqrt{(Z_i - Z_j)^2} \quad (6.2c)$$

where R_i and R_j is the radial position of particles i and j , respectively. θ_i and θ_j is the theta position of particles i and j . Z_i and Z_j is the vertical position of particles i and j . Φ_{ij} for each contact was calculated using Equation 6.3 [87]:

$$\Phi_{ij} = 2ka(T_j - T_i) \quad (6.3)$$

where k is the particle thermal conductivity, a is the contact radius, and T_j and T_i are the temperatures of particle i and j , respectively.

Figure 6.1 depicts the conduction flux over time in the radial, theta, and vertical direction for a shallow bed ($H/D = 0.46$) with an impeller agitation rate of 5 rpm and a particle conductivity of 10 W/mK. Additionally, three screenshots provide a visual of the bed temperature at different time points. At time $t = 0$ s, the bed was uniform with an initial temperature T_0 . Since there was no temperature gradient in the bed, the conductive flux was zero. Around time $t = 10$ s, the particles located near the walls of the vessel started heating up while the core of the bed remained relatively cold. The temperature gradient within the bed was strong, leading the conduction flux to increase and reach a maximum. Over time, the bed continued to heat up and became more uniform in temperature as all the particles approached the temperature of the wall T_w . The

conduction flux gradually approached zero ($t = 200$ s). Similar trends were observed for conduction in the radial, theta, and axial directions. Overall, the conduction flux in the radial and axial directions were the largest because the heating source came from the side walls and the bottom walls of the vessel, so the temperature gradients were the greatest in the radial and vertical directions, respectively. Heating in the theta direction occurred to a lesser extent and was the result of localized temperature gradients due to random particle mixing.

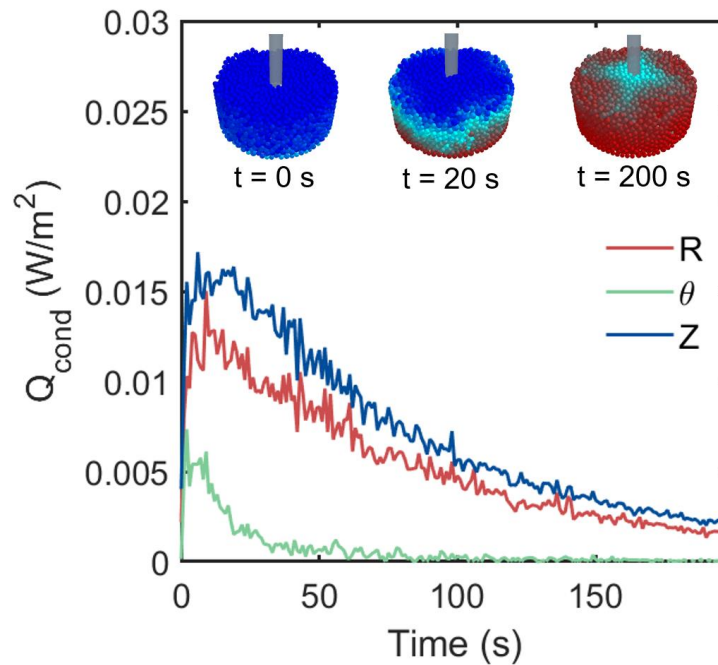


Figure 6.1: Evolution of the conductive flux over time in the radial (R), theta (θ), and axial (Z) direction for a shallow bed with $H/D = 0.46$.

Next, we computed the particle-to-particle conductive flux for beds with different fill levels. The simulations used for this analysis are the ones presented previously in Chapter 5. Figure 6.2a shows the conductive flux in the radial direction as a function of time for beds with different H/D ratios. For all the tested fill heights, the shape of the conductive flux over time followed similar trends as in Figure 6.1 for a shallow bed: the

conductive flux initially started at zero, rose until reaching a maximum, and then decreased over time. Overall, the higher the bed fill height, the greater the conductive flux. Figure 6.2b shows the time-average of the radial conductive flux as a function of H/D . Each data point represents a simulation where the conductive flux was averaged over 200 seconds. The figure outlines a clear positive correlation between H/D and conductive heat transfer. Although not shown, similar results were observed for conductive fluxes in the theta and vertical direction. Previously, Figure 5.3b, Figure 5.3c, and Figure 5.4 from Chapter 5 had demonstrated that large H/D ratios led to more compression in the bed, with greater contact overlaps and more contacts. Since conduction is a function of the contact overlap and the number of contacts (Equations 6.1 and 6.3), we hypothesize that the positive relationship between the conduction flux and the H/D ratio stems from the increase in compression for deep beds.

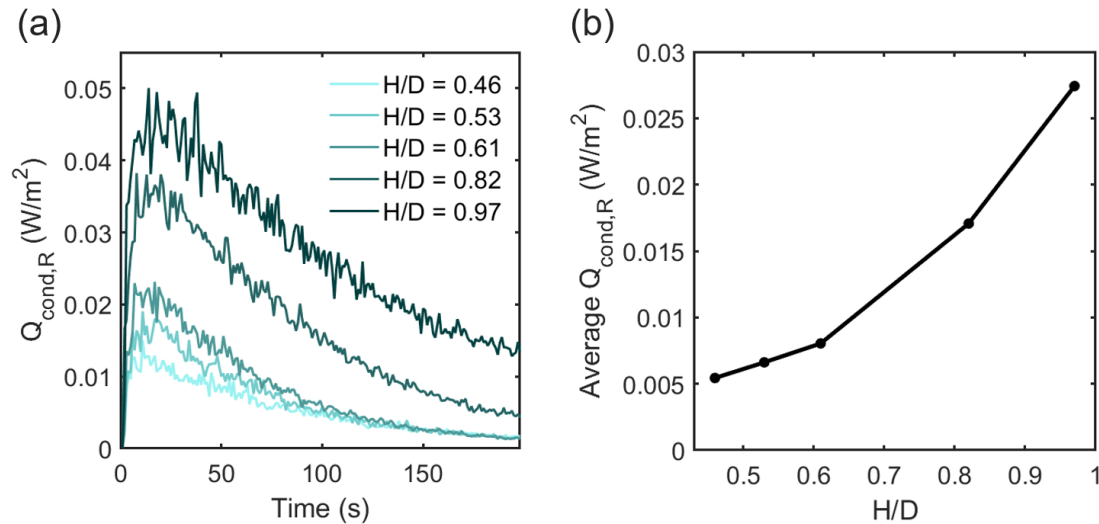


Figure 6.2: (a) Radial conductive flux over time for beds with different H/D . (b)

Radial conductive flux averaged over time versus H/D .

6.2 Explaining Unexpected Trends from Chapter 3 Using Conduction at the Wall

Conductive heat transfer between the wall and the particles touching the wall can be computed by adapting Equation 6.1, Equation 6.2, and Equation 6.3. We obtain analogous equations as seen below:

$$\bar{Q}_{cond,wall} = \frac{1}{\Omega} \sum_{iw}^{N_w} \Phi_{iw} \vec{r}_{iw} \quad (6.4)$$

where $\bar{Q}_{cond,wall}$ is the particle-to-wall conductive flux density, Ω is the bed volume, N_w is the total number of particle contacts with the wall, Φ_{iw} is the heat flux for the contact between particles i and the wall, and \vec{r}_{iw} is the center-to-center contact vector for the contact between particles i and the wall. The center-to-center contact vector for the radial, theta, and vertical direction are given by Equations 6.5a, 6.5b, and 6.5c, respectively.

$$r_{iw,R} = \sqrt{(R_i - R_{wall})^2} \quad (6.5a)$$

$$r_{iw,\theta} = \sqrt{2R_i R_{wall} * (1 - \cos(\theta_i - \theta_{wall}))} \quad (6.5b)$$

$$r_{iw,Z} = \sqrt{(Z_i - Z_{wall})^2} \quad (6.5c)$$

where R_i and R_{wall} is the radial position of particles i and the wall, respectively. θ_i and θ_{wall} is the theta position of particles i and the wall. Z_i and Z_{wall} is the vertical position of particles i and the wall. Φ_{iw} for each contact was calculated using Equation 6.6:

$$\Phi_{iw} = \frac{4a(T_w - T_i)}{\frac{1}{k_i} + \frac{1}{k_w}} \quad (6.6)$$

where k_i and k_w is the thermal conductivity of the particle and the wall, respectively, a is the contact radius, and T_i and T_w are the temperatures of particle i and the wall, respectively.

We looked at how the thermal conductivity of the material and the impeller agitation rate affected heat transfer via conduction to better understand two unexpected trends observed in Figure 3.5b of Chapter 3. The plots in Figure 3.5b of Chapter 3 are reproduced below as Figure 6.3a and Figure 6.3b. The first unexpected result was that for material with a high thermal conductivity, we noticed that very slow agitation rates led to a dip in the effective heat transfer coefficient (Figure 6.3a). This was counterintuitive, as we expected that any agitation should have improved the effective heat transfer coefficient. Instead, the results in Figure 6.3a show that the rate of heat transfer was faster for a case without agitation than a case with an agitation rate of 0.5 rpm. For agitation rates greater than 0.5 rpm, we saw that the heat transfer coefficient increased, as expected. The second unexpected trend is that for a material with low thermal conductivity, we observed that high agitation rates led to a decline in the effective heat transfer coefficient (Figure 6.3b). Again, we expected that more agitation would improve heat transfer, so this result was counterintuitive.

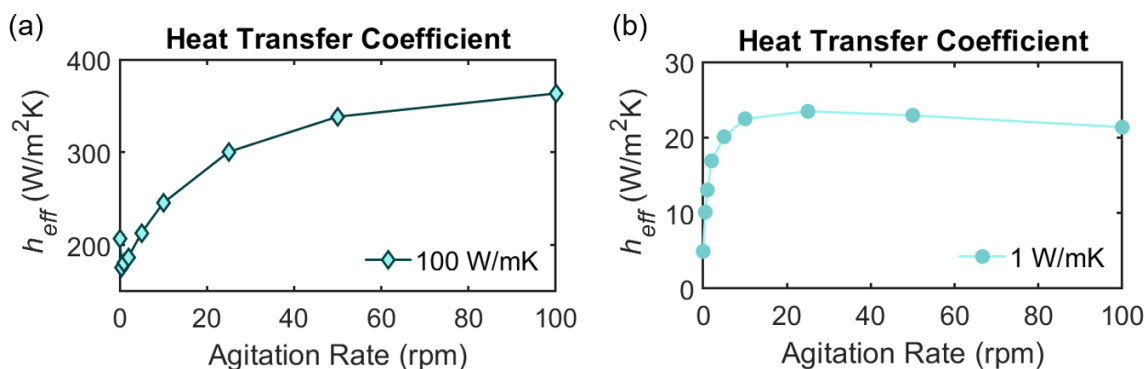


Figure 6.3: Heat transfer coefficient for a material with a thermal conductivity of (a) 100 W/mK and (b) 1 W/mK.

We sought to better understand the decrease in heat transfer occurring at slow agitation rates in Figure 6.3a and at high agitation rates in Figure 6.3b. To do so, we

analyzed different factors that could be important for heat transfer through conduction. More specifically, we hypothesized that there are three factors that can affect heat transfer between the vessel wall and the particle bed:

- Factor 1: Bringing cold particles in contact with the hot wall (i.e.: changing the temperature gradient $T_i - T_w$)
- Factor 2: Changing the contact overlap (i.e.: changing a)
- Factor 3: Changing the number of particles in contact with the wall (i.e.: total number of particles at the wall)

The driving force for conductive heat transfer between two objects is related to the temperature difference between them (Equation 6.6). According to Equation 6.6, the larger the temperature gradient, the faster the rate of heat transfer. Factor 1 suggests that the temperature gradient can be improved in a bladed mixer by bringing cold particles to the hot wall. Figure 6.4a and 4b illustrate how the impeller agitation rate influences Factor 1 for particles touching the wall for a poorly and a highly conductive material, respectively. For all agitation rates, the temperature gradient starts at a maximum value because the particles all have an initial temperature T_0 , while the wall has a temperature T_w . Over time, the mean temperature gradient decreases until it approaches 0 as all the particles at the wall approach T_w . Overall, the temperature gradient decreases faster for the case with $k = 100$ W/mK (Figure 6.4a) than $k = 1$ W/mK (Figure 6.4b) because particles heat up faster in a more conductive bed.

The agitation rate affects how often and how rapidly cold particles are moved from the center of the bed to the wall. Interestingly, Figure 6.4 shows that the effect of the agitation rate on the mean temperature gradient is not the same for a highly conductive

material (Figure 6.4a) and a poorly conductive material (Figure 6.4b). In Figure 6.4a, the smallest temperature gradient occurred for the case without agitation (i.e.: 0 rpm in Figure 6.4) because particles were stagnant. We see that agitating at 0.5 rpm or 1 rpm led to temperature gradients similar to the case with 0 rpm agitation, meaning that slow agitation was not enough to significantly enhance the temperature gradient in this case. The simulation with 25 rpm agitation showed a noticeable improvement in the temperature gradient. Finally, the case with 100 rpm agitation shows the greatest temperature gradient. If Factor 1 was considered on its own, the results in Figure 6.4a suggest that for a highly conductive material ($k = 100 \text{ W/mK}$ in this case), agitation rates greater than 1 rpm are needed to improve the temperature gradient and enhance heat transfer. In Figure 6.4b, we observe that any increase in agitation rate led to significantly larger mean temperature gradients between the wall and the particles at the wall. If Factor 1 was considered on its own, the results in Figure 6.4b suggest that for a poorly conductive material ($k = 1 \text{ W/mK}$ in this case), the faster the agitation rate, the larger the temperature gradient and the better the heat transfer.

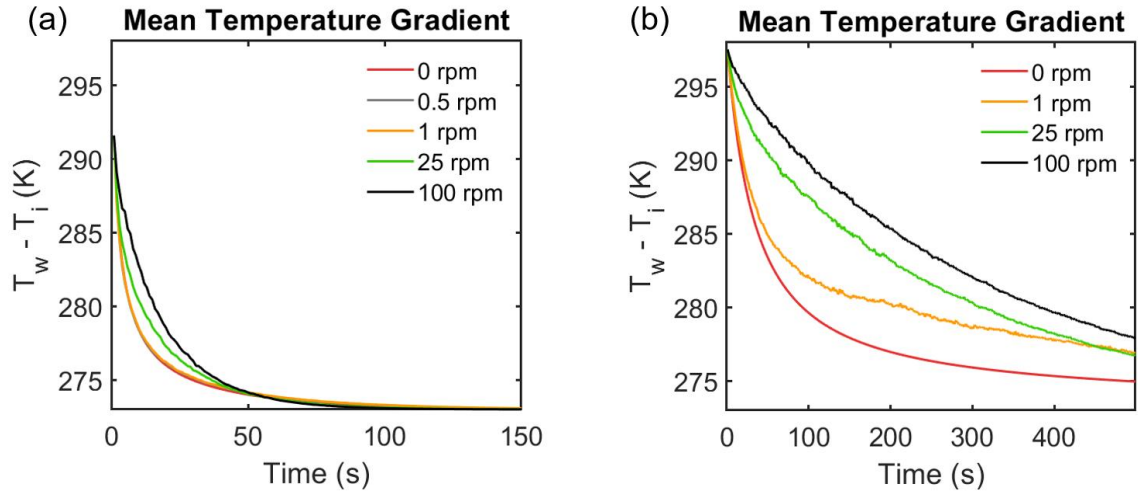


Figure 6.4: Mean temperature difference between the wall temperature and the temperature of the particles touching the wall over time for different agitation rates. The simulations are for materials with a thermal conductivity of (a) $k = 100$ W/mK and (b) $k = 1$ W/mK.

Next, we investigated how the material thermal conductivity and the agitation rate influence Factor 2. Factor 2 is related to the contact radius, which is another important parameter for heat transfer (Equation 6.6). Equation 6.6 states that the larger the contact overlap between a particle and the wall, the greater the conduction flux between them. Figure 6.5 shows the mean contact overlap as a function of agitation rate for a highly and a poorly conductive material. As expected, Figure 6.5 shows that the thermal conductivity did not affect the contacts, since the results in Figure 6.5a and Figure 6.5b look nearly identical. Minute differences between them are likely due to randomness in particle packing. Figure 6.5 shows that the average contact overlap is strongly dependent on the agitation rate. Going from no agitation to very slow agitation led to a drastic increase in contact overlaps. After that, further increasing the agitation rate further increased the mean contact overlap, albeit less drastically. If considered on its own,

Factor 2 suggests that adding a little bit of agitation should increase heat transfer significantly, and that increasing the impeller speed past that would continue to increase heat transfer but less significantly.

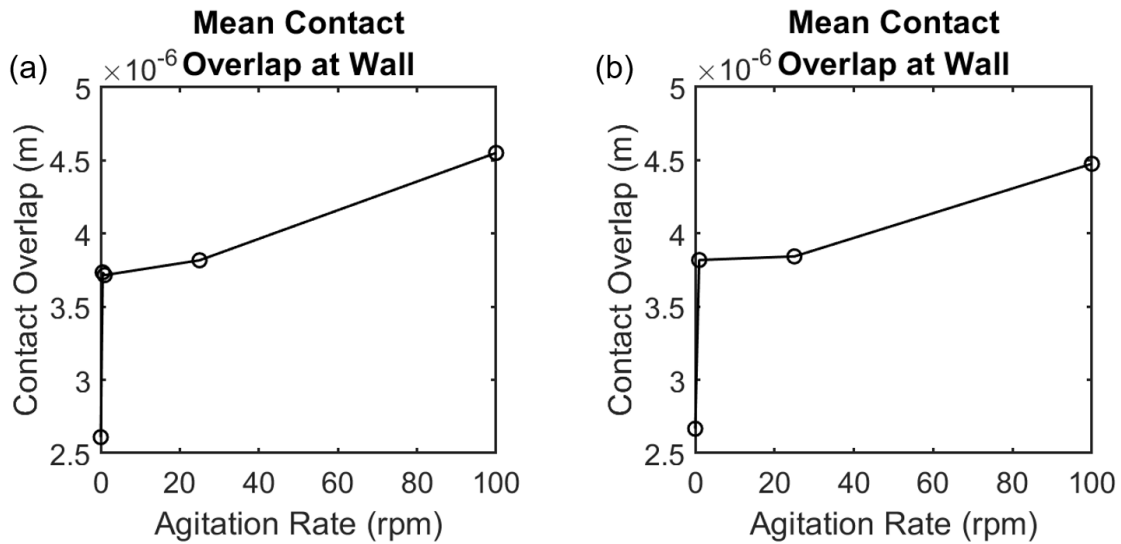


Figure 6.5: Mean contact overlap between the wall and particles at the wall for materials with a thermal conductivity of (a) 100 W/mK and (b) 1 W/mK.

Finally, we studied the influence of the thermal conductivity and the agitation rate on Factor 3, which refers to the number of particles touching the wall. Equation 6.4 implies that the higher the number of particles touching the wall, the greater the rate of conductive heat transfer between the wall and the particles. As with Figure 6.5, Figure 6.6 shows that the material thermal conductivity did not affect the total number of contacts at the wall, since Figure 6.6a and Figure 6.6b are nearly identical. However, we observe a strong dependence between the number of contacts and the agitation rate. More specifically, going from no agitation to a slow agitation rate led to a significant drop in the number of particle contacts. Agitating faster continued to decrease the number of particle contacts but less drastically. The negative correlation between the number of contacts and the agitation rate is due to bed dilation. As the impeller blades pass through

the bed, they lift particles up, creating more voidage in the bed and reducing the number of particle contacts. If considered on its own, Factor 3 suggests that increasing the agitation rate from 0 rpm to slow impeller speeds should significantly decrease heat transfer, and that further increasing it would continue to decrease heat transfer through conduction.

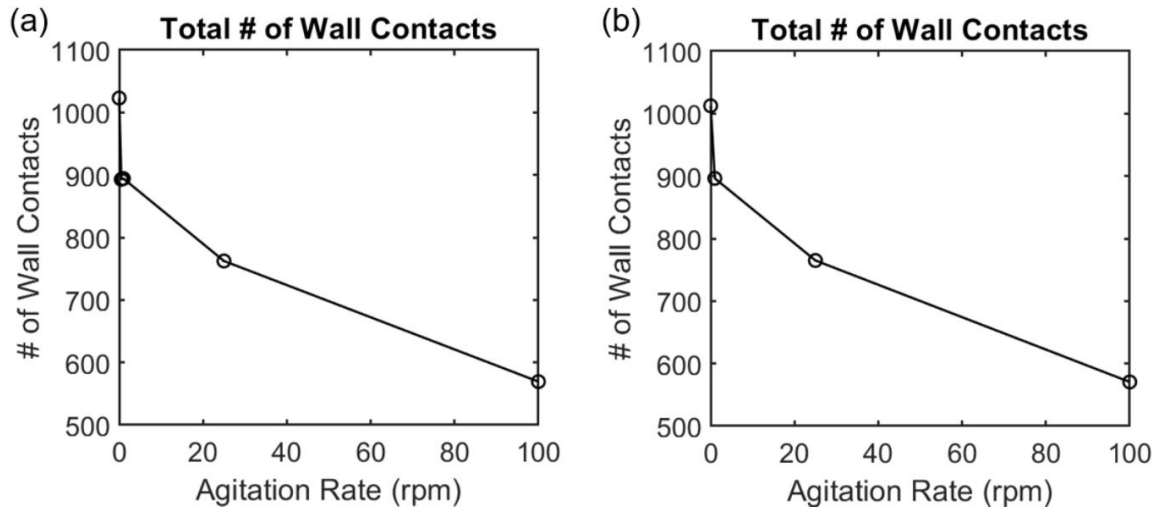


Figure 6.6: Total number of wall contacts for materials with a thermal conductivity of (a) 100 W/mK and (b) 1 W/mK.

Next, we demonstrate the combined effects of Factors 1, 2, and 3 on the conduction flux between the wall and the particles touching the wall. Figure 6.7 shows the relationship between the agitation rate and the wall conduction flux for a highly conductive material (Figure 6.7a) and a poorly conductive material (Figure 6.7b). The wall conduction flux was summed over 200 s for the case with $k = 100$ W/mK and was summed over 500 s for the case with $k = 1$ W/mK. Overall, Figure 6.7a shows that, for a highly conductive material, fast agitation rates led to greater wall conduction fluxes. This is consistent with Figure 6.3a, where we observed that fast agitation rates led to high effective heat transfer coefficients. Interestingly, the dip that we observed in heat transfer

coefficient at slow agitation rates in Figure 6.3a also appears in Figure 6.7a. Together, Figure 6.4a, Figure 6.5a, and Figure 6.6a provide a potential explanation for this pattern. Slow agitation rates led to a negligible improvement in the temperature gradient (Figure 6.4a, i.e.: Factor 1), an increase in the mean contact overlap (Figure 6.5a, i.e.: Factor 2), and a decrease in the total number of wall contacts (Figure 6.6a, i.e.: Factor 3). For a highly conductive material, we conclude that Factor 3 dominates over Factor 1 and Factor 2 at slow agitation rates and that Factor 1 and Factor 2 dominate over Factor 3 at fast agitation rates.

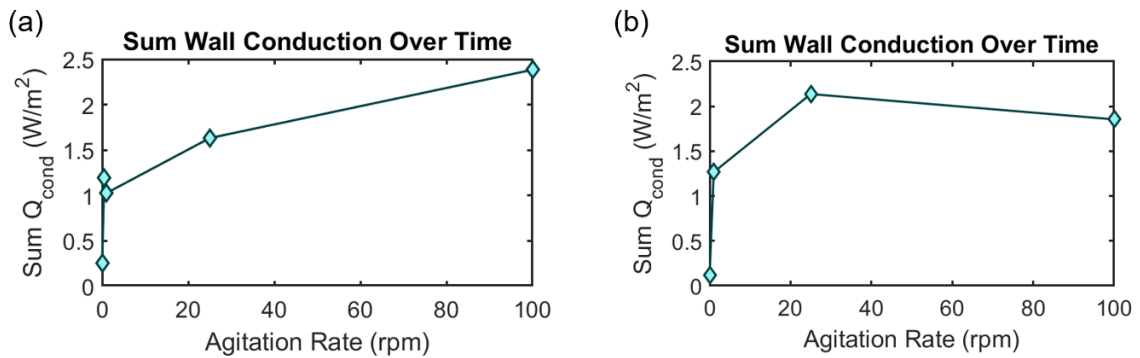


Figure 6.7: Wall conduction flux summed over time as a function of agitation rate of a material with a thermal conductivity of (a) 100 W/mK and (b) 1 W/mK.

Figure 6.7b shows that, for a poorly conductive material, agitation rates between 0 and 25 rpm led to an improvement in the conduction flux, which is consistent with the results exhibited by Figure 6.3b. Similarly, Figure 6.7b shows that agitation rates faster than 25 rpm led to a decrease in the conduction flux, which is also consistent with Figure 6.3b. Figure 6.4b, Figure 6.5b, and Figure 6.6b explain this unexpected trend. Agitation rates between 0 and 25 rpm led to significant improvement in the temperature gradient (Figure 6.4b, i.e.: Factor 1), an increase in the mean contact overlap (Figure 6.5b, i.e.: Factor 2), and a decrease in the total number of wall contacts (Figure 6.6b, i.e.: Factor 3).

For a poorly conductive material, the results suggest that Factor 1 and Factor 2 dominate over Factor 3 for agitation rates between 0 and 25 rpm, and that Factor 3 dominates over Factor 1 and Factor 2 at agitation rates above 25 rpm.

6.3 Heat Transfer Through Granular Convection

In addition to conduction, heat transfer through particles in a bladed mixer also occurs via granular convection. Granular convection does not refer to convection between particles and an interstitial gas, since fluids were neglected in this model, but rather describes heat transferred from particles exchanging their thermal energy as they move through the bed. Granular convection was calculated using Equation 6.7:

$$\vec{Q}_{conv} = \frac{1}{\Omega} \sum_i m_i C_p T_i \vec{v}_i \quad (6.7)$$

where \vec{Q}_{conv} is the convection flux density, Ω is the volume of the particle bed, i is the particle index, m_i is the mass of particle i , C_p is the specific heat capacity of the material, T_i is the temperature of particle i , and \vec{v}_i is the velocity of particle i . \vec{Q}_{conv} is a vector quantity, which enables us to evaluate granular convection in the radial, theta, and vertical directions in the bed. Figure 6.8 illustrates the convection flux density over time for the different directions. The case simulated was for a shallow bed with a thermal conductivity of $k = 10$ W/mK and an agitation rate of 5 rpm. We notice that granular convection in the radial and vertical directions oscillate around zero, while there is a large amount of convection in the theta direction. This is because the geometry of the bladed mixer is symmetric and there is no net movement in the radial and vertical directions. When there is agitation, convection in the theta direction is large because the impeller

blades move counterclockwise, so the particles have velocities with large theta components. The fluctuations are likely due to randomness in particle movement through the bed. Overall, $Q_{conv,R}$ and $Q_{conv,Z}$ show no significant change with time. $Q_{conv,\theta}$ slightly increases with time due to the increase in particle temperature over time. The large convective flux in the theta direction is somewhat counterintuitive because there is no obvious temperature gradient in the theta direction. The heat source in the bladed mixer comes from the side walls and the base of the vessel, so the temperature gradients stem mainly from the radial and vertical directions, respectively. At the same time, we are examining the average convection in the system and there is net movement of particles in the theta direction and when these particles move, they take their associated energy with them so this leads to bulk convection of heat. This is analogous to flow of a fluid or particles at a given temperature through a pipe. The flow of the particles or fluid leads to a convective flux despite the temperature in the pipe being a constant. If an imaginary person stood in the pipe as cold fluid flowed past them, then the velocity of the fluid would affect the convective flux and the rate of cooling of the person, in the same way that a cold windy day will cool someone faster than a cold still day.

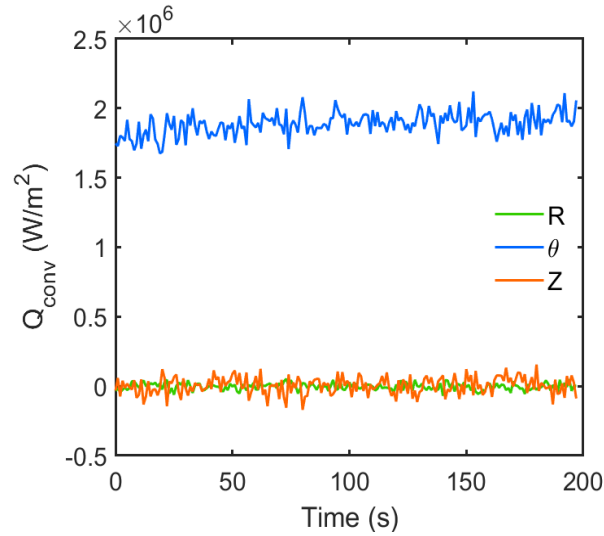


Figure 6.8: Granular convection flux density over time in the radial R , theta θ , and vertical Z directions.

Next, we investigated the effect of the impeller agitation rate on granular convection. Figures 6.9a, 6.9b, and 6.9c show the granular convection over time for different impeller speeds in the radial, theta, and vertical directions, respectively. As expected, we observed a strong correlation between the impeller speed and the convection flux. This is because granular convection is based on particles moving through the bed and exchanging heat with other particles. The faster the agitation rate, the greater the particle velocities, and the faster they encounter other particles to transfer energy. This is reflected in Figure 6.9, where we notice that higher agitation rates led to better heat transfer through granular convection in the theta direction. Overall, we find that the magnitude of $Q_{conv,\theta}$ scaled proportionally with the agitation rate. Figure 6.9 also shows that the agitation rate influenced the magnitude of the fluctuations in the convection flux. We hypothesize that higher agitation rates led to more variability in the average particle velocities and therefore increased the magnitude of the fluctuations.

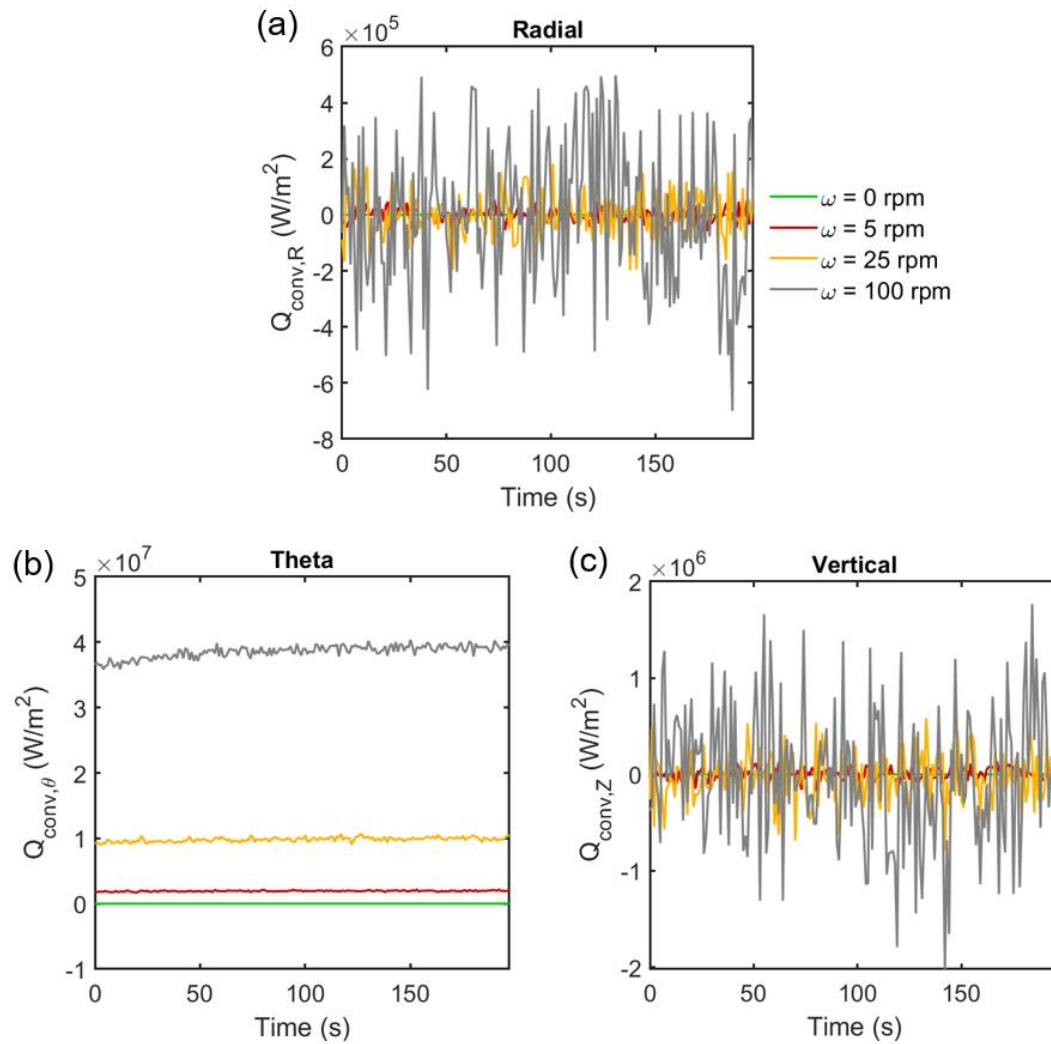


Figure 6.9: Granular convection over time in the radial, theta, and vertical direction for different agitation rates.

6.4 Conclusions About Conduction and Granular Convection

In this chapter, we took a more theoretical approach to studying heat transfer through granular material in a bladed mixer by computing the conduction and convection fluxes for different scenarios. Our analysis on conduction yielded new insights on the unexpected trends we had observed previously in Chapter 3. We found that 3 main

factors influenced conduction: the average temperature gradient in the bed, the average contact overlap between particles and the wall, and the average number of contacts at the wall. The agitation rate of the impeller affects each one of these factors, but interestingly, the extent to which it influences them depends on the thermal conductivity of the material. For example, we found that for a highly conductive material, the conduction flux was mainly affected by the number of contacts at slow agitation rates, and by the temperature gradients and contact overlaps at fast agitation rates. By contrast, for a poorly conductive material, the conduction flux was mainly affected by the temperature gradients and the contact overlaps at slow agitations rates, and by the number of contacts at high agitation rates.

Our analysis on convection showed that the convection flux dominated in the theta direction, while the net convection fluxes in the radial and vertical directions were zero. We found that this was due to the strong dependence on the average particle velocities in the bed. Overall, while particles may have local movements in the radial and vertical directions, the bed as a whole had no net velocity in the radial and vertical directions. By contrast, we observed very large convection fluxes in the theta direction because the impeller blades rotate through the bed with an angular motion and make the particles have velocities with large theta components. We found that the magnitude of the convection flux in the theta direction scaled proportionally with the agitation rate. The results from our analysis on convection were surprising because they suggested most of the heat transfer occurred in the theta direction. This was not intuitive to us because there is no net temperature gradient in the theta direction.

7. CONCLUSIONS AND FUTURE WORK

Heated bladed mixers are a relevant equipment for a variety of industries. In pharmaceutical manufacturing processes, bladed mixers are often used for agitated drying of APIs. However, despite their ubiquity, many unanswered questions remain about the behavior of granular materials in this equipment and scale up of the process is often a challenging task. The work presented here focuses on elucidating the heat transfer aspect of agitated drying. We leverage a combination of computational and experimental techniques to investigate how material properties, operating conditions, and scale up of the system influence heat transfer in a granular bed. Ultimately, the objective of this research was to enhance fundamental understanding of agitated drying processes and to help improve the design of operating protocols.

7.1 Conclusions

One of the questions we sought to answer with this research was how the thermal properties of a material and the operating parameters affect heat transfer in a bladed mixer. In the pharmaceutical industry, APIs have varying thermal and flow properties which makes it virtually impossible to implement the same drying protocol for all APIs. The extent to which material thermal properties influence the heating process had not been thoroughly investigated prior to this work. Another crucial parameter in the process is the rotation speed of the impeller. Optimizing the agitation rate is often a careful consideration during the design of protocols because it can both benefit and hinder the process. The advantage of agitating the bed is that it can help enhance heat transfer by bringing cold particles in contact with hot particles. Selecting the proper speed of rotation

can be crucial, however, as agitating too slowly can lead to very slow and nonuniform heating, while agitating too rapidly can lead to particle breakage.

We conducted numerical simulations to study how varying material thermal conductivities and agitation rates affected both the rate of heat transfer and the uniformity of the bed. The computational tool consisted of the discrete element method coupled with a heat transfer model. The geometry was a laboratory-scale agitated dryer, which was approximated as a cylindrical vessel with a bladed impeller in the model. Our results indicated that the extent to which the agitation rate improved heating depended on the bed's thermal conductivity. For a poorly conductive material, we found that slowly agitating the bed improved heat transfer substantially but further increasing the speed of the impeller led to a negligible improvement. We observed that the reason for this was because poorly conductive materials tend to heat up uniformly with a small amount of mixing, so further mixing an already uniform bed did not increase the rate of heat transfer. Overall, for highly conductive materials, we found that the bed heated up rapidly but nonuniformly. A fast agitation rate considerably improved heat transfer in the bed, as it allowed for particles with different temperatures to come into contact and exchange thermal energy. Unexpectedly, slowly agitating a highly conductive bed slightly hindered heat transfer compared to the case without agitation. We noticed that this was due to the sharp drop in coordination number that occurred when slowly agitating the bed, leading to a decrease in conduction in the bed and not enough mixing to overcome the decrease in heat transfer.

An important finding from this work is that there appears to be a critical agitation rate beyond which the improvement in heat transfer due to faster agitation becomes less

substantial. The critical agitation rate was found to depend on the material's thermal conductivity. For poorly conductive materials, like most APIs, the results indicated that the critical agitation rate is fairly slow (around 10 rpm). We found that agitating the bed more rapidly was not necessarily beneficial in terms of heat transfer. The implications of these results are significant, as they can help guide the selection of agitation rates for drying protocols. For example, if an API is prone to attrition, it could be helpful to ensure that the impeller speed does not exceed the critical agitation rate for that material.

The analysis of these simulations was further expanded by identifying dimensionless groups for the system and nondimensionalizing the results. We identified three heating regimes: a conduction-dominated regime where the bed heated rapidly but with a large temperature gradient, a convection-dominated regime where the bed heated slowly but uniformly, and an intermediate regime where conduction and granular convection contributed relatively equally. The dimensionless groups enabled us to collapse our results together and obtain a mathematical expression relating the agitation rate, the conductivity, and heat transfer. Additionally, we found that the temperature standard deviation of the bed could be related to these scaling parameters. Together, the analysis allowed for an approximate prediction of both the mean temperature of the bed and the standard deviation of the temperature distribution.

Next, we sought to confirm the results found in the numerical simulations by carrying out experiments. We conducted heat transfer experiments in a laboratory-scale bladed mixer with glass beads and an infrared camera. To our knowledge, the use of infrared imaging to measure bed temperatures in an agitated drying process had not been presented in the literature prior to this research. We conducted a series of experiments

where we varied the agitation rate and recorded the temperature of the bed surface over the course of the heating process. We then computed heat transfer coefficients for each scenario and analyzed the uniformity of the bed by calculating the temperature standard deviation over time. The experimental results suggest that thermal imaging can be used as a noninvasive PAT tool for quantifying heat transfer in a bladed mixer. Traditionally, agitated drying systems make use of thermocouples to collect temperature data. The main challenges with thermocouples are that they only provide data for a single location in the bed and they are intrusive (i.e.: the probe acts as a baffle during mixing). Infrared imaging collects temperature data for the entire bed surface, providing information about the mean temperature of the bed as well as the temperature uniformity. The camera can detect cold and hot spots in the bed in real-time and could potentially be used as a control tool to aid in the decision of when to agitate the bed.

We compared our computational results to the experiments and found good agreement, despite the simplicity of our heat transfer model. Visually, we were able to compare the temperature of the bed surface in the simulations to that of the experiment by color-coding the particles according to temperature. We observed that the evolution of the bed surface temperature over time showed good qualitative agreement between the simulation and the experiment. We also carried out a quantitative comparison of the modeling and the experimental results by looking at the mean temperature, the dimensionless temperature, the heating time, the heat transfer coefficient, and the temperature standard deviation of the bed surface. Overall, the modeling and the experimental results showed very similar trends for the different agitation rates evaluated but the case without agitation showed some differences. Our model underpredicted the

rate of heating for a case without agitation. However, in both cases we found that no agitation led to the slowest heat transfer and that even a little bit of agitation led to a considerably faster heat transfer. Past a critical agitation rate, we found that the increase in heat transfer due to faster agitation became less significant. The results on temperature uniformity of the bed also indicated good qualitative agreement between the model and the experiments. Temperature standard deviation started at zero when all of the particles started at room temperature, rose to a maximum as the temperature gradient in the bed increased, and decayed exponentially as the material approached the wall temperature of the vessel. We were also able to quantify the effect of agitation on the temperature uniformity of the bed for both the simulations and the experiments. Overall, the simulations slightly overestimated the nonuniformity of the bed compared to the experiments for all the agitation rates studied. However, the results showed similar qualitative trends. The bed without agitation was the least uniform throughout the heating process and exhibited a heating behavior that resembled that of a solid body. The temperature gradient at the surface showed a concentric ring pattern, where particles along the edge of the vessel wall were the warmest, and particles in the center of the bed were the coldest. The cases with slow agitation showed considerable improvement in the heating uniformity, meaning that even a little bit of agitation was enough to bring cold and hot particles together and enhance the heating uniformity of the bed. The cases with fast agitation also improved the heating uniformity, albeit less drastically. The validation of the computational results suggests that the equations in our model are a reasonable approximation to the physics of the system, and that these simulations can be leveraged to acquire a deeper and more fundamental understanding of the process.

Next, we applied the discrete element method and the heat transfer model to study scale up of the process. More specifically, we carried out simulations where we varied the fill height and the size of the mixer and quantified the influence of these parameters on the rate of heat transfer in the bed. The results indicated that the effect of fill height on heat transfer was nontrivial because numerous competing factors contributed to heat transfer. More specifically, we found that increasing the fill height decreased the AM^* ratio, which relates the heating surface area to the bed mass, decreased the overall rate of mixing in the bed, increased the mean normalized % contact overlap between the particles, and increased the mean coordination number in the bed. These factors have opposing effects in terms of heat transfer and therefore compete to influence the process. Overall, we found that shallow beds had the fastest heat transfer due to their high AM^* ratio and fast mixing. Intermediate beds had the slowest heat transfer due to their low AM^* ratio and slow mixing. Interestingly, very deep beds were found to have slightly faster heat transfer than intermediate beds due to the increase in bed compression.

We also carried out simulations to study how heat transfer occurs in vessels of different sizes. These simulations represented a geometric scale up, where the fill height and the diameter of the vessel were scaled linearly. The results revealed that the heating time and the vessel size were linearly and positively correlated. We found that the % contact overlap and the coordination number changed slightly due to the increase in fill level but that this increase was not enough to influence heat transfer significantly. Similarly, increasing the vessel size did not substantially affect the rate of mixing. We found that the AM^* ratio was the main driving factor influencing heat transfer. As the D/d ratio was scaled up, the AM^* ratio drastically decreased and therefore led to longer

heating times. Overall, the results suggested that the heating time of the bed is proportional to the diameter of the vessel, that the proportionality constant is order one, and that the value of the constant depends on the agitation rate.

Finally, we sought to explore heat transfer for granular material in a bladed mixer on a more theoretical level by computing the conduction and convection fluxes for cases with varying thermal conductivities and agitation rates. Our analysis showed that heat transfer via conduction depended on both the agitation rate and the thermal conductivity of the material. The relevant parameters in the conduction equation were the average temperature gradient in the bed, the average contact overlap between particles and the wall, and the number of contacts at the wall. For a highly conductive material, we found that the conduction flux was mainly influenced by the number of contacts at slow agitation rates, and by the temperature gradients and contact overlaps at fast agitation rates. However, for a poorly conductive material, we found that the conduction flux mainly depended on the temperature gradients and the contact overlaps at slow agitations rates, and by the number of contacts at fast agitation rates.

Our analysis on the convection flux indicated that the agitation rate was a very influential parameter. Rotating the impeller induced rapid particle tangential velocities which led to very large convection fluxes in the theta direction. By contrast, particles had no net velocity in the radial and vertical directions, so the radial and vertical convection flux oscillated around zero. Overall, the magnitude of the convection flux in the theta direction scaled proportionally with the impeller agitation rate.

7.2 Future Work

The results presented in this dissertation enhance fundamental understanding of how heat transfer occurs in a bladed mixer and provide insights into how material thermal properties and operating conditions influence the process at both small and larger scales. These findings complement previous experimental and computational work carried out to study the particle flow behaviors in this geometry. This work adds a level of complexity by incorporating the heat transfer element to these studies. At the same time, the results are for a specific geometry and parameter set. Additional work is needed to confirm that the findings hold for bladed mixers with other dimensions and other parameter values.

For the simulations, it would be beneficial to incorporate moisture into the model and see how the conclusions hold, given the transient interplay between heat transfer, evaporation, and mass transfer during drying. Such a model could help elucidate whether agitated drying processes are typically mass-transfer limited or heat-transfer limited and dictate how the drying protocol should be designed given this information. Another complication of adding moisture is that the moisture itself affects the flow behavior and packing of the bed. Thus, as the bed dries the flow behaviors change which in turn affects the heat transfer and mass transfer. In principle, one can carry out such simulations but with so many coupled processes it can be challenging to isolate the influence of each parameter and obtain a thorough understanding of the process. There are few DEM studies that use a coupled heat-and-mass transfer model to simulate agitated drying applications [11, 103]. Additional work is needed to expand on these studies. For example, it would be interesting to track the moisture content for each particle in the bed over time. This kind of simulation would enable us to not only quantify the uniformity of

the bed temperature, as we have presented in this work, but also to assess the moisture uniformity of the bed.

In addition to the agitation rate of the impeller, another critical process parameter during drying is the temperature of the heating jacket. It is important to realize that some APIs are temperature-sensitive and that the drying protocol may need to set constraints for the heating temperature. It would be interesting to carry out simulations and experiments to investigate how different wall temperatures influence the heating behavior and to see whether this parameter could be integrated into the dimensionless scaling presented in this work. Other granular parameters that affect heat transfer and could be interesting to incorporate into a future parametric study include the particle size, the wall friction, and the coefficient of restitution. We chose to study thermal properties first as they are part of the heat transfer equation and are therefore known to affect heating directly. The challenge with studying parameters such as the coefficient of restitution, wall friction, and particle size is that they would also influence flow and mixing in the bed so it would be difficult to decouple heat transfer from flow effects. These simulations considered a limited set of material and process parameters so incorporating additional variables into the dimensional analysis could help improve scientific understanding of the system. Particle size is of particular importance since many pharmaceutical APIs will break during agitation so the particle size will decrease during the agitated drying process. It is of interest to examine how size influences the rate of heat transfer in a bladed mixer. Previous work has reported that particle size and polydispersity influence the effective thermal conductivity of a static packed bed [104]. Since particle size may also affect flow and mixing, simulations and experiments should be carried out for

different particle sizes to better understand how size influences heat transfer in an agitated bed.

It is also possible to include breakage into DEM models to eventually investigate how attrition occurs during agitated drying processes. For example, Guo *et al.* [105] implemented a bonded-particle model to study particle breakage of high aspect ratio particles in a bladed mixer. In their model, a needle-like particle, represented by a string of bonded spheres, breaks at the center of a bond when the shear or tensile stress exceeds the material strength. Incorporating the heat transfer equations into a DEM model with particle breakage could help inform the selection of an optimal agitation rate for agitated drying processes. A risk-benefit analysis could be conducted where the risk of attrition for a particular agitation rate is weighed against the increase in heat transfer provided by that agitation. It would be interesting to conduct this analysis for materials with different tensile or shear strength.

In terms of future work for the experiments, it would be interesting to carry out studies with more pharmaceutically relevant materials, such as citric acid and threonine for example. The experiments presented in this work used glass beads, which are a simplification of real pharmaceutical powders. Typical pharmaceutical materials can be porous, brittle, nonspherical, and can have varying particle size distributions with polydispersity. As a result, they often exhibit complex behaviors such as particle breakage, cohesion, agglomeration, and segregation. Investigating how heat transfer occurs in these materials in a bladed mixer could help improve process understanding and make this work even more relevant and applicable to industrial scenarios. It is also of interest to simulate such non-spherical systems. In EDEM®, small spheres can be bonded

together to create a composite particle or, alternatively, a CAD drawing can be inputted into the model to obtain an exact representation of the particle shape. These approaches have been used in previous work to investigate flow and mixing behaviors for non-spherical particles such as needles, L-shapes, as well as more complex shapes in a bladed mixer [77]. It would be of interest to incorporate heat transfer to these studies to see how the findings for spherical particles obtained in this work hold for other particle shapes.

Additionally, while this work presented numerical simulations of heat transfer for scale up applications, we were not able to conduct the experiments for a system larger than laboratory-scale. More experiments are needed to validate the simulation results on scale up and ensure that the model accurately portrays the system for larger scales. We have also only measured temperatures at the surface of the bed so it would be of interest to examine temperatures within the bed. This can be accomplished by inserting thermocouples into the bed. The challenge with thermocouples is that the probes can act as baffles and alter the mixing behavior in the bed. To circumvent this, the experiment can be halted at specific time intervals, and the thermocouples can be inserted while the bed is static. The mixing can then be restarted until the next temperature measurement.

In this work we have focused on constant agitation rates. However, in pharmaceutical applications, the drying protocol often involves periodic agitation where the bed is at rest for some time and then agitated for some time. It would be of interest to examine heat transfer and mass transfer for non-constant agitation protocols. This can initially be done for heat transfer both through DEM modeling and through experiments. For example, it would be interesting to see whether agitating at a constant rate for a specific number of impeller revolutions (e.g.: 10 revolutions where we agitate constantly

at 10 rpm for 1 minute) leads to similar heating times as agitating intermittently at double the agitation rate (e.g.: 10 revolutions where we agitate at 20 rpm for 30 seconds and 0 rpm for 30 seconds). Additionally, the temperature standard deviation of the bed could be used to determine when to agitate and when to let the bed rest. For example, in the experiments presented in this work, we found that the temperature standard deviation peaks and starts to decay after a set number of impeller revolutions based on the agitation rate. It would be interesting to simulate an intermittent agitation protocol where the time for the agitating period and the static period is a function of that number of impeller revolutions.

The model we used for heat transfer does not consider heat transfer from the particle to the gas to the particle. We therefore consider an “effective” thermal conductivity between particles. Previous work has examined heat transfer from the particle to the gas to the particle and incorporated this in DEM [38, 91, 106]. It is of interest to examine such “more sophisticated” models to see whether they better capture experimental results. In a real drying process, there is liquid, gas, and solid particles and heat transfer through all three phases should be considered. It is of interest to examine how adding liquid changes the heat transfer of a powder bed. The liquid adds significantly to the thermal mass but also can have a relatively high thermal conductivity. Depending on the particle and liquid thermal properties, one can imagine scenarios where having liquid increases the rate of heat transfer and cases where the liquid decreases the rate of heat transfer. Further work is needed both in simulations and experiments to see how liquid affects the heat transfer. Moreover, during drying of APIs a vacuum and gas sweeps are often employed. The effects of the vacuum and the gas sweep on heat transfer

and mass transfer should be examined since they can influence particle to gas heat transfer as well as the rate of solvent evaporation [107]. Experiments on beds with different vacuum pressures, different inert gases, and different gas velocities should be carried out to determine the impact on the drying performance.

APPENDIX

A.1 Appendix for Chapter 3

In Chapter 3, we presented a dimensionless scaling that enabled us to collapse the data together and establish a relationship between the agitation rate of the impeller, the thermal properties of the material, and the heating time of the bed. We used the Buckingham π Theorem to define the variables in our scaling and obtain the dimensionless groups. The methodology for our procedure is outlined below.

(1) Define the variables in the problem and calculate the expected number of dimensionless parameters

$$\tau_b = f(k, \rho, C_p, \omega, V, a)$$

$$n = 7 \text{ variables}$$

$$d = 4 \text{ dimensions (M, L, t, } \theta)$$

$$\text{Therefore } \pi = n - d = 3 \text{ dimensionless parameters}$$

(2) Define the dimensions of each variable and choose the repeating variables

Variable	Description	Dimensions
τ_b	Thermal time	T
k	Conductivity	$\text{MLt}^{-3}\theta^{-1}$
ρ	Density	ML^{-3}
C_p	Specific heat capacity	$\text{L}^2\text{t}^{-2}\theta^{-1}$
ω	Agitation rate	t^{-1}
V	Volume	L^3
a	Contact radius	L

Based on the dimensions in the table above, appropriate repeating variables are ρ , a , ω , and C_p .

(3) Calculate the 1st dimensionless parameter π_1

$$\pi_1 = \tau_b \rho^a a^b \omega^c C p^d$$

$$\{M^0 L^0 t^0 \theta^0\} = \left\{ (t) \left(\frac{M}{L^3} \right)^a (L)^b \left(\frac{1}{t} \right)^c \left(\frac{L^2}{t^2 \theta} \right)^d \right\}$$

Solve the balance and obtain the coefficients $a = 0, b = 0, c = 1, d = 0$

$$\pi_1 = \tau_b \omega$$

(4) Calculate the 2nd dimensionless parameter π_2

$$\pi_2 = k \rho^e a^f \omega^g C p^h$$

$$\{M^0 L^0 t^0 \theta^0\} = \left\{ \left(\frac{ML}{t^3 \theta} \right) \left(\frac{M}{L^3} \right)^e (L)^f \left(\frac{1}{t} \right)^g \left(\frac{L^2}{t^2 \theta} \right)^h \right\}$$

Solve the balance and obtain the coefficients $e = -1, f = -2, g = -1, h = -1$

$$\pi_2 = \frac{k}{\rho C_p a^2 \omega}$$

(5) Calculate the 3rd dimensionless parameter π_3

$$\pi_3 = V \rho^i a^j \omega^k C p^l$$

$$\{M^0 L^0 t^0 \theta^0\} = \left\{ (L^3) \left(\frac{M}{L^3} \right)^i (L)^j \left(\frac{1}{t} \right)^k \left(\frac{L^2}{t^2 \theta} \right)^l \right\}$$

Solve the balance and obtain the coefficients $i = 0, j = -3, k = 0, l = 0$

$$\pi_3 = \frac{V}{a^3}$$

(6) Write the final relationship

$$\tau_b \omega = f \left(\frac{\rho C_p a^2 \omega}{k}, \frac{V}{a^3} \right)$$

If $\pi_1 = f(\pi_2, \pi_3)$ is the function $\pi_1 = f(\pi_2 * \pi_3)$, then $\tau_b \omega = f \left(\frac{\rho C_p V \omega}{k a} \right)$

Substituting $\tau_c = \frac{1}{\omega}$ and $\tau_p = \frac{\rho C_p V}{k a}$ gives $\frac{\tau_b}{\tau_c} = f \left(\frac{\tau_p}{\tau_c} \right)$

A new dimensionless parameter ϕ can be defined and yield $\frac{\tau_b}{\tau_c} = f(\phi)$.

A.2 Appendix for Chapter 4

In Chapter 4, we showed the temperature standard deviation for the simulations and the experiments where the bed was agitated. The temperature standard deviation for the 0 rpm case was so much larger than the cases for 5 rpm, 10 rpm, 25 rpm, and 100 rpm, that the data did not easily fit in Figure 4.12. Thus, Figure A.2.1 shows the standard deviation results for all the agitation rates, including the case without agitation. Figures A.2.1a and A.2.1b illustrate the results for the experiments and the simulations, respectively. We observe that the model significantly overestimates the standard deviation for a static bed, compared to the experiment. The maximum temperature standard deviation for a static bed obtained from the simulation was three times larger than the experimental temperature standard deviation. Additionally, the standard deviation calculated from the model peaked much later than the experiment. Once again, we hypothesize that the disparity between the modeling and the experimental results for case without agitation is due to improper model calibration for a static bed. The simulations presented here have a thermal conductivity that was calibrated for an agitated bed, whereas we expect that the thermal properties of a static bed would be significantly different. The results suggest that the model may need to be calibrated separately for a static bed.

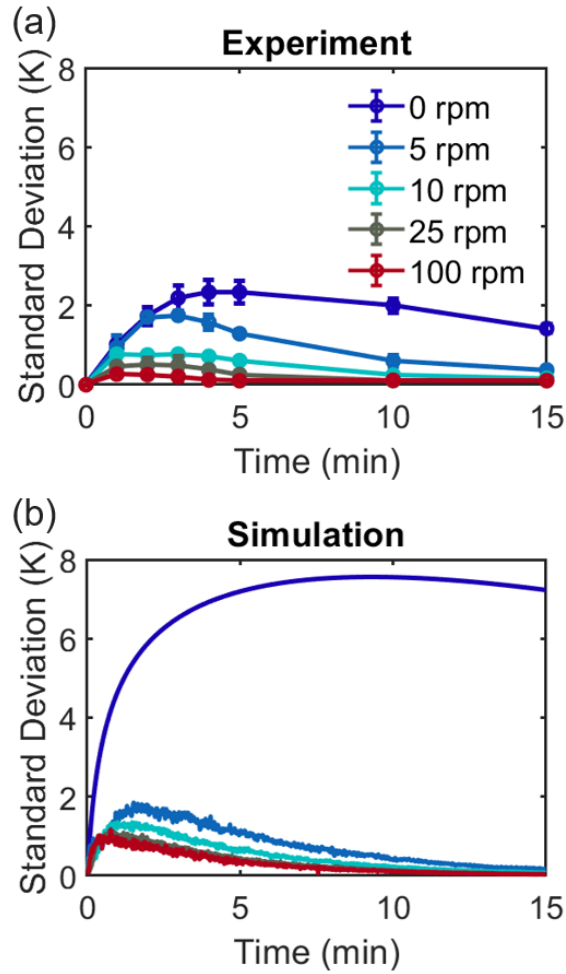


Figure A.2.1: (a) Experimental standard deviation of the bed surface temperature over time for different agitation rates. (b) Simulated standard deviation of the bed surface temperature over time for different agitation rates.

A.3 Appendix for Chapter 5

Since Equation 2.16 indicates that the heat conductance between two particles in contact depends on the softness of the material, we investigated how varying the stiffness of the material would influence heat transfer in the bed. Figure A.3.1a shows the relationship between the shear modulus and the heating time τ_b for beds with different fill levels (H/D). As expected, the results suggest that increasing the shear modulus (i.e.:

stiffer particles) increased the time needed to heat the bed, while decreasing the shear modulus (i.e.: softer particles) led to faster heating times. This is expected because softer particles tend to have larger contact overlaps between them, leading to a larger channel for thermal conduction. In terms of the relationship with the H/D ratio, we observe that, for the range of shear modulus studied, the heating time is short for shallow beds, relatively large for beds with H/D ratios between 1.0 and 1.5, and decreases for very deep beds.

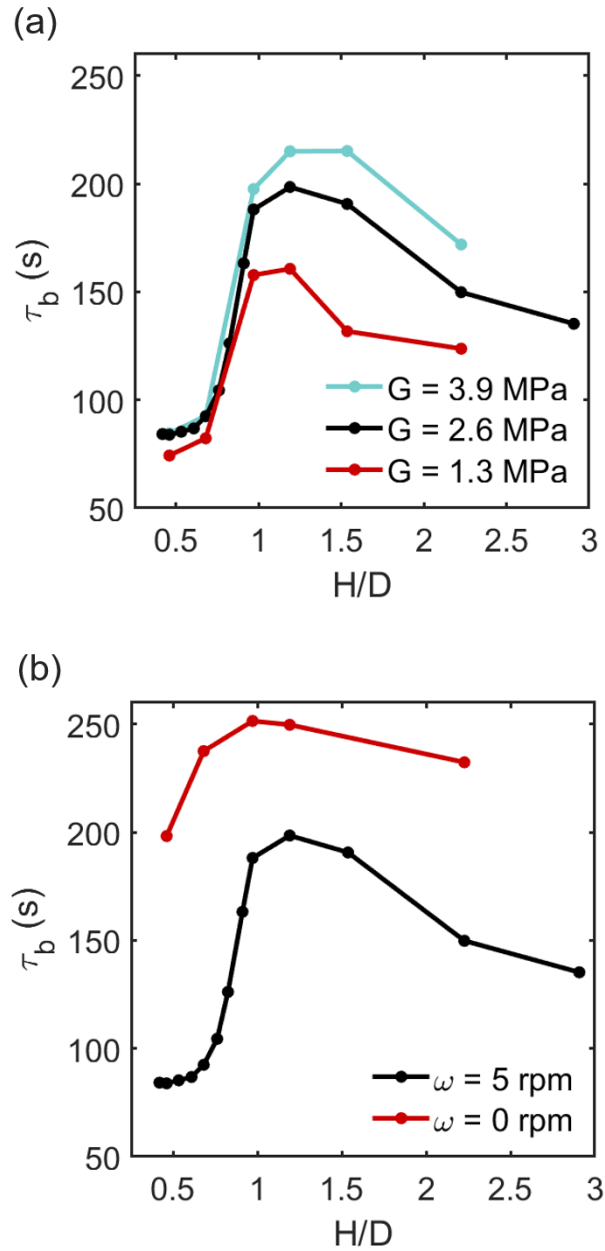


Figure A.3.1: (a) Effect of varying the shear modulus on the heating time for beds with different fill heights. (b) Effect of no agitation and 5 rpm agitation rate on the heating time for beds with different fill heights.

Figure A.3.1b illustrates the effect of the impeller agitation rate on the heating time for beds with different fill heights. We observe that the heating time was significantly longer for the case without agitation for beds with all fill heights. This result

was expected because mixing helps bring hot particles and cold particles from different locations in the bed together and therefore improves heat transfer, thereby decreasing the heating time. For the conditions tested in these simulations, we found that the relationship between the heating time and the H/D ratio followed similar trends for both 0 rpm and 5 rpm agitation. More specifically, we found that the heating time was shortest for shallow beds, then increased for beds with H/D ratios ranging from 0.8 to 1.5 and decreased for very deep beds.

NOTATION

List of Variables

a_{ij}	Contact radius between two particles (m)
A_b	Surface area of the bed available for heat transfer (m ²)
$A_{shallow}$	Surface area of the bed available for heat transfer of the shallowest bed (m ²)
A^*	Characteristic area (-)
AM^*	Ratio of the heated surface area to the vessel mass normalized by the area and mass of the shallowest bed (-)
C_p	Specific heat capacity of particles (J/kg K)
d	Diameter of particles (m)
D	Diameter of the mixer (m)
D/d	Mixer diameter to particle diameter ratio (-)
e	Coefficient of restitution (-)
E	Young's modulus (Pa)
E_i	Young's modulus of particle i (Pa)
E_{ij}	Effective Young's modulus (Pa)
F_{Nij}	Normal force resulting from the contact of particle i with particle j (N)
F_{Tij}	Tangential force resulting from the contact of particle i with particle j (N)
g	Gravitational acceleration (m/s ²)
G	Shear modulus (Pa)
h_{eff}	Effective heat transfer coefficient between the wall and the bed (W/m ² K)
H	Fill height of particle bed (m)

H/D	Material fill height to mixer diameter ratio (-)
H_{cij}	Heat conductance between two particles (W/mK)
I_i	Moment of inertia of particle i ($\text{kg}\cdot\text{m}^2$)
k	Particle thermal conductivity (W/mK)
k_i	Thermal conductivity of particle i (W/mK)
k_{ij}	Effective thermal conductivity (W/mK)
k_w	Wall thermal conductivity (W/mK)
\tilde{k}_n	Normal stiffness coefficient (-)
\tilde{k}_t	Tangential stiffness coefficient (-)
L	Length of blades (m)
L^*	Characteristic length (m)
M_b	Mass of particle bed (kg)
m_i	Mass of particle i (kg)
$M_{shallow}$	Mass of the shallowest bed (m^2)
N	Number of particles in the simulation (-)
N_c	Total number of contacts in the bed (-)
N_i	Number of touching neighboring particles (-)
N_w	Total number of contacts at the wall (-)
Pe	Péclet number (-)
Q_{ij}	Heat flux exchanged between two particles (W)
Q_{iw}	Heat flux exchanged between a particle and a wall (W)
\vec{Q}_{cond}	Particle-to-particle conduction flux density (W/m^3)
$\vec{Q}_{cond,wall}$	Particle-to-wall conduction flux density (W/m^3)

\bar{Q}_{conv}	Granular convection flux density (W/m ³)
R_i	Radial position of particle i in a mixer (m)
R_{wall}	Radial position at the wall (m)
r or r_i	Radius of particles or particle i (m)
\vec{r}_{ij}	Center-to-center contact vector for the contact between two particles (m)
\vec{r}_{iw}	Center-to-center contact vector for the contact between particle i and the wall (m)
RSD	Relative standard deviation of particle concentration (-)
t	Time (s)
t^*	Characteristic time (s)
T_0	Initial temperature (K)
T_i	Temperature of particle i (K)
$T_{i,0}$	Initial temperature of particle i (K)
T_w	Wall temperature (K)
\bar{T}_b	Mean temperature of the bed (K)
$\bar{T}_{b,0}$	Mean initial temperature of the bed (K)
T^*	Dimensionless temperature (-)
Δt	Time step (s)
u^*	Characteristic linear velocity (m/s)
v_i	Linear velocity of particle i (m/s)
v_{rel}^t	Relative tangential velocity of the colliding particles (m/s)
V_i	Volume of particle i (m ³)
V_C	Size (volume) of the control volume (m ³)

V_p	Volume of a particle (m^3)
V_r	Radial velocity of particles (m/s)
V_t	Tangential velocity of particles (m/s)
V_y	Vertical velocity of particles (m/s)
Z_i	Vertical position of particle i in a mixer (m)
Z_{wall}	Vertical position at the wall (m)

List of Subscripts

0, 1, 2, 3	Subscripts for D and H in Table 2.1 which denote each part of the schematic in Fig. 2.1 of Chapter 2
------------	--

List of Greek Letters

α	Thermal diffusivity (m^2/s)
β	Fitting coefficient for decay equation (-)
γ	Fitting coefficient for decay equation (-)
$\tilde{\gamma}_n$	Normal damping coefficient (-)
$\tilde{\gamma}_t$	Tangential damping coefficient (-)
δ_n	Normal displacement (m)
δ_t	Tangential displacement (m)
θ_i	Theta position of particle i in a mixer (m)
θ_{wall}	Theta position at the wall (m)
μ_{conc}	Mean concentration of a type of particles ($\text{particles}/\text{m}^3$)
μ_r	Rolling friction coefficient (-)

μ_s	Sliding friction coefficient (-)
ν	Poisson's ratio (-)
ρ	Particle density (kg/m ³)
ρ_{bulk}	Bulk material density (kg/m ³)
σ_{conc}	Standard deviation of particle concentration (particles/m ³)
σ_T	Standard deviation of the bed temperature (K)
σ_T^*	Normalized standard deviation of the bed temperature (K)
τ_b	Thermal time of the bed (s)
τ_c	Contact time (s)
τ_p	Thermal time of a particle (s)
τ_s	Thermal time of the bed surface (s)
τ_{rij}	Stress resulting from the contact of particle i with particle j (Pa)
ϕ	Dimensionless ratio relating the thermal time of the bed, the thermal time of the particle, and the contact time (-)
ϕ_{ij}	Heat flux for the contact between particles i and j (W)
ϕ_{iw}	Heat flux for the contact between particles i and the wall (W)
ω	Agitation rate (rpm)
ω_i	Angular velocity of particle i (rad/s)
Ω	Volume of the bed (m ³)

ACKNOWLEDGEMENT OF PREVIOUS PUBLICATIONS

This dissertation contains significant portions of the following publications:

1. Hartmanshenn C., Khinast J. G., Papageorgiou C. D., Mitchell C., Quon J., Glasser B. J., Heat Transfer of Dry Granular Materials in a Bladed Mixer: Effect of Thermal Properties and Agitation Rate, *AIChE Journal*, 2019. 66(4):e16861.
2. Hartmanshenn C., Halota M., Khinast J. G., Papageorgiou C. D., Mitchell C., Quon L. J., Glasser B. J., Scale Up of Heat Transfer for Dry Granular Material in a Cylindrical Bladed Mixer, (Submitted 2020).
3. Hartmanshenn C., Patel S., Chakraborty N., Halota M., Khinast J. G., Papageorgiou C. D., Mitchell C., Quon L. J., Glasser B. J., Infrared Temperature Measurements and DEM Simulations of Heat Transfer in an Agitated Dryer, (Submitted 2020).
4. Hartmanshenn C., Khinast J. G., Papageorgiou C. D., Mitchell C., Quon L. J., Glasser B. J., Conduction and Granular Convection in a Bladed Mixer, (Submitted 2020)

REFERENCES

1. Muzzio, F.J., T. Shinbrot, and B.J. Glasser, *Powder technology in the pharmaceutical industry: the need to catch up fast*. Powder Technology, 2002. **124**(1-2): p. 1-7.
2. Sudah, O.S., D. Coffin-Beach, and F.J. Muzzio, *Quantitative characterization of mixing of free-flowing granular material in tote (bin)-blenders*. Powder Technology, 2002. **126**(2): p. 191-200.
3. Vagenas, G.K. and V.T. Karathanos, *Prediction of Moisture Diffusivity in Granular-Materials, with Special Applications to Foods*. Biotechnology Progress, 1991. **7**(5): p. 419-426.
4. Arias-Garcia, P.A., et al., *Physical Characterization of Granular Components Used in Road Construction*. Powders and Grains 2009, 2009. **1145**: p. 163-166.
5. Vidales, A.M., et al., *Granular components of cement: Influence of mixture composition*. Powder Technology, 2006. **163**(3): p. 196-201.
6. Muzzio, F.J., et al., *Solids mixing part A: Fundamentals of solid mixing*. Handbook of Industrial Mixing: Science and Practice, ed. J.W.S. Inc. 2004.
7. Nedderman, R.M., *Statics and Kinematics of Granular Materials*. 1992: Cambridge University Press.
8. Vargas, W.L. and J.J. McCarthy, *Heat conduction in granular materials*. AIChE Journal, 2001. **47**(5): p. 1052-1059.
9. Mullier, M.A., J.P.K. Seville, and M.J. Adams, *The Effect of Agglomerate Strength on Attrition during Processing*. Powder Technology, 1991. **65**(1-3): p. 321-333.
10. am Ende, D., et al., *Development and Application of Laboratory Tools To Predict Particle Properties upon Scale-Up in Agitated Filter-Dryers*. Organic Process Research & Development, 2013. **17**(10): p. 1345-1358.
11. Sahni, E.K. and B. Chaudhuri, *Numerical simulations of contact drying in agitated filter-dryer*. Chemical Engineering Science, 2013. **97**: p. 34-49.
12. Conder, E.W., et al., *The Pharmaceutical Drying Unit Operation: An Industry Perspective on Advancing the Science and Development Approach for Scale-Up and Technology Transfer*. Organic Process Research & Development, 2017. **21**(3): p. 420-429.
13. Kougoulos, E., C.E. Chadwick, and M.D. Ticehurst, *Impact of agitated drying on the powder properties of an active pharmaceutical ingredient*. Powder Technology, 2011. **210**(3): p. 308-314.
14. Shekunov, B.Y., et al., *Particle size analysis in pharmaceuticals: Principles, methods and applications*. Pharmaceutical Research, 2007. **24**(2): p. 203-227.
15. Lamberto, D.J., A. Diaz-Santana, and G. Zhou, *Form Conversion and Solvent Entrapment during API Drying*. Organic Process Research & Development, 2017. **21**(11): p. 1828-1834.
16. Jaeger, H.M., S.R. Nagel, and R.P. Behringer, *Granular solids, liquids, and gases*. Reviews of Modern Physics, 1996. **68**(4): p. 1259-1273.
17. Daerr, A. and S. Douady, *Two types of avalanche behaviour in granular media*. Nature, 1999. **399**: p. 241-243.

18. Peden, R., S. Bless, and M. Iskander, *Penetration of Granular Materials: New Experimental Techniques*. 27th International Symposium on Ballistics, Vols. 1 and 2, 2012: p. 1443-1452.
19. Knight, J.B., et al., *Density Relaxation in a Vibrated Granular Material*. Physical Review E, 1995. **51**(5): p. 3957-3963.
20. Nowak, E.R., et al., *Reversibility and irreversibility in the packing of vibrated granular material*. Powder Technology, 1997. **94**(1): p. 79-83.
21. Campbell, C.S., *The Stress Tensor for Simple Shear Flows of a Granular Material*. Journal of Fluid Mechanics, 1989. **203**: p. 449-473.
22. da Cruz, F., et al., *Rheophysics of dense granular materials: Discrete simulation of plane shear flows*. Physical Review E, 2005. **72**(2).
23. Savage, S.B. and K. Hutter, *The Motion of a Finite Mass of Granular Material down a Rough Incline*. Journal of Fluid Mechanics, 1989. **199**: p. 177-215.
24. Khosropour, R., et al., *Convection and size segregation in a Couette flow of granular material*. Physical Review E, 1997. **56**(4): p. 4467-4473.
25. Alam, M. and P.R. Nott, *Stability of plane Couette flow of a granular material*. Journal of Fluid Mechanics, 1998. **377**: p. 99-136.
26. Khakhar, D.V., et al., *Transverse flow and mixing of granular materials in a rotating cylinder*. Physics of Fluids, 1997. **9**(1): p. 31-43.
27. Clement, E., J. Rajchenbach, and J. Duran, *Mixing of a granular material in a bidimensional rotating drum*. Fractal Aspects of Materials, 1995. **367**: p. 513-517.
28. Cundall, P.A. and O.D.L. Strack, *A discrete numerical model for granular assemblies*. Geotechnique, 1979. **29**: p. 47-65.
29. Rognon, P., et al., *A scaling law for heat conductivity in sheared granular materials*. EPL (Europhysics Letters), 2010. **89**(5).
30. Perry, J.H., *Chemical Engineers Handbook*, ed. McGraw-Hill.
31. Kayrak-Talay, D., A. Horton, and K. Jacob, *Experimental studies in the thermal conductivity of bulk solids*, in *8th International Conference for Conveying and Handling of Particulate Solids*. 2015.
32. Weidenfeld, G., Y. Weiss, and H. Kalman, *A theoretical model for effective thermal conductivity (ETC) of particulate beds under compression*. Granular Matter, 2004. **6**(2-3): p. 121-129.
33. Vargas, W.L. and J.J. McCarthy, *Thermal expansion effects and heat conduction in granular materials*. Physical Review E, 2007. **76**(4): p. 041301.
34. Gan, J., Z. Zhou, and A. Yu, *Effect of particle shape and size on effective thermal conductivity of packed beds*. Powder Technology, 2017. **311**: p. 157-166.
35. Gupta, K.G., M.J. Laubitz, and A. Feingold, *An apparatus to measure the effect of moisture content of granular materials on their conductivity*. Letters in Heat and Mass Transfer, 1978. **5**(2): p. 89-97.
36. Abu-Hamdeh, N.H. and R.C. Reeder, *Soil thermal conductivity: Effects of density, moisture, salt concentration, and organic matter*. Soil Science Society of America Journal, 2000. **64**(4): p. 1285-1290.
37. Widenfeld, G., Y. Weiss, and H. Kalman, *The effect of compression and preconsolidation on the effective thermal conductivity of particulate beds*. Powder Technology, 2003. **133**(1-3): p. 15-22.

38. Mishra, I., et al., *Experimental validation of indirect conduction theory and effect of particle roughness on wall-to-particle heat transfer*. AIChE Journal, 2019. **65**(10).
39. Forgber, T., et al., *Heat transfer rates in sheared beds of inertial particles at high Biot numbers*. Granular Matter, 2017. **19**(1): p. 1-23.
40. Einav, I., et al., *10,000 – A reason to study granular heat convection*. AIP Conference Proceedings, 2013. **1542**(38): p. 38-45.
41. Sahni, E.K. and B. Chaudhuri, *Contact drying: A review of experimental and mechanistic modeling approaches*. International Journal of Pharmaceutics, 2012. **434**(1-2): p. 334-348.
42. Lim, H.L., K.P. Hapgood, and B. Haig, *Understanding and preventing agglomeration in a filter drying process*. Powder Technology, 2016. **300**: p. 146-156.
43. Emady, H.N., et al., *Prediction of conductive heating time scales of particles in a rotary drum*. Chemical Engineering Science, 2016. **152**: p. 45-54.
44. Shokri, N., et al., *Drying front and water content dynamics during evaporation from sand delineated by neutron radiography*. Water Resources Research, 2008. **44**(6): p. 1-11.
45. Huang, N., et al., *Flow of wet granular materials*. Physical Review Letters, 2005. **94**(2).
46. Shokri, N., M. Sahimi, and D. Or, *Morphology, propagation dynamics and scaling characteristics of drying fronts in porous media*. Geophysical Research Letters, 2012. **39**(9): p. 1-5.
47. Lekhal, A., et al., *Impact of agitated drying on crystal morphology: KCl–water system*. Powder Technology, 2003. **132**(2-3): p. 119-130.
48. Remy, B., J.G. Khinast, and B.J. Glasser, *Wet granular flows in a bladed mixer: Experiments and simulations of monodisperse spheres*. AIChE Journal, 2012. **58**(11): p. 3354-3369.
49. Lekhal, A., et al., *Characterization of granular flow of wet solids in a bladed mixer*. AIChE Journal, 2006. **52**(8): p. 2757-2766.
50. Scicolone, J.V., et al., *Effect of liquid addition on the bulk and flow properties of fine and coarse glass beads*. AIChE Journal, 2016. **62**(3): p. 648-658.
51. Lekhal, A., et al., *The effect of agitated drying on the morphology of l-threonine (needle-like) crystals*. International Journal of Pharmaceutics, 2004. **270**(1-2): p. 263-277.
52. Warner, A.M., J.D. Stafford, and R.E. Warburton, *Establishing a microbial control strategy for active pharmaceutical ingredients*. American Laboratory, 2007. **39**(12): p. 15-18.
53. Zhou, G.X., et al., *Determination and differentiation of surface and bound water in drug substances by near infrared spectroscopy*. Journal of Pharmaceutical Sciences, 2003. **92**(5): p. 1058-1065.
54. Papageorgiou, C.D., et al., *Development of Screening Methodology for the Assessment of the Agglomeration Potential of APIs*. Organic Process Research & Development, 2016. **20**(8): p. 1500-1508.
55. Nere, N.K., et al., *Drying process optimization for an API solvate using heat transfer model of an agitated filter dryer*. J Pharm Sci, 2012. **101**(10): p. 3886-95.

56. Hartmanshenn, C., M. Scherholz, and I.P. Androulakis, *Physiologically-based pharmacokinetic models: approaches for enabling personalized medicine*. J Pharmacokinet Pharmacodyn, 2016. **43**(5): p. 481-504.
57. Bhakay, A., et al., *Bioavailability Enhancement of Poorly Water-Soluble Drugs via Nanocomposites: Formulation-Processing Aspects and Challenges*. Pharmaceutics, 2018. **10**(3): p. 1-62.
58. Kolehmainen, J., et al., *Triboelectric charging of monodisperse particles in fluidized beds*. AIChE Journal, 2016. **63**(6): p. 1872-1891.
59. Zhang, S. and D.J. Lamberto, *Development of new laboratory tools for assessment of granulation behavior during bulk active pharmaceutical ingredient drying*. J Pharm Sci, 2014. **103**(1): p. 152-160.
60. Remy, B., J.G. Khinast, and B.J. Glasser, *Polydisperse granular flows in a bladed mixer: Experiments and simulations of cohesionless spheres*. Chemical Engineering Science, 2011. **66**(9): p. 1811-1824.
61. Boonkanokwong, V., et al., *The effect of the number of impeller blades on granular flow in a bladed mixer*. Powder Technology, 2016. **302**: p. 333-349.
62. Boonkanokwong, V., et al., *Flow of granular materials in a bladed mixer: Effect of particle properties and process parameters on impeller torque and power consumption*. Advanced Powder Technology, 2018. **29**(11): p. 2733-2752.
63. Sahni, E.K., R.H. Bogner, and B. Chaudhuri, *Systematic investigation of parameters affecting the performance of an agitated filter-dryer*. J Pharm Sci, 2013. **102**(7): p. 2198-2213.
64. Parris, J., et al., *Monitoring API drying operations with NIR*. Spectroscopy, 2005. **20**(2): p. 34-39.
65. Adamson, J., et al., *Development of Suitable Plant-Scale Drying Conditions That Prevent API Agglomeration and Dehydration*. Organic Process Research & Development, 2015. **20**(1): p. 51-58.
66. Dodda, A.G., *An Integrated Computational and Experimental Approach to Study and Scale-Up Vacuum Drying of Pharmaceutical Products*, in *Department of Chemical Engineering*. 2014, University of Massachusetts.
67. Li, W., *Drying of Pharmaceutical Powders Using An Agitated Filter Dryer*, in *Institute of Particle Science and Engineering*. 2014, The University of Leeds.
68. Boepple, B.R., *Heat Transfer in a Rotary Drum Using Infrared Camera Temperature Measurement*, in *Department of Chemical Engineering*. 2019, Arizona State University.
69. Lamberto, D.J., et al., *Laboratory methods for assessing API sensitivity to mechanical stress during agitated drying*. Chemical Engineering Science, 2011. **66**(17): p. 3868-3875.
70. Remy, B., et al., *Scale-up of agitated drying: Effect of shear stress and hydrostatic pressure on active pharmaceutical ingredient powder properties*. AIChE Journal, 2015. **61**(2): p. 407-418.
71. Schlunder, E. and N. Mollekopf, *Vacuum contact drying of free flowing mechanically agitated particulate material*. Chemical Engineering and Processing, 1984. **18**: p. 93-111.
72. Kwapinska, M., G. Saage, and E. Tsotsas, *Continuous versus discrete modelling of heat transfer to agitated beds*. Powder Technology, 2008. **181**(3): p. 331-342.

73. Hoekstra, L., P. Vonk, and L.A. Hulshof, *Modeling the Scale-Up of Contact Drying Processes*. Organic Process Research & Development, 2006. **10**: p. 409-416.
74. Havlica, J., et al., *The effect of rotational speed on granular flow in a vertical bladed mixer*. Powder Technology, 2015. **280**: p. 180-190.
75. Barczi, T., et al., *Effect of Bed Depth on Granular Flow and Homogenization in a Vertical Bladed Mixer via Discrete Element Method*. Chemical Engineering & Technology, 2015. **38**(7): p. 1195-1202.
76. Radl, S., et al., *Mixing characteristics of wet granular matter in a bladed mixer*. Powder Technology, 2010. **200**(3): p. 171-189.
77. Saeed, M.K. and M.S. Siraj, *Mixing study of non-spherical particles using DEM*. Powder Technology, 2019. **344**: p. 617-627.
78. Remy, B., B.J. Glasser, and J.G. Khinast, *The effect of mixer properties and fill level on granular flow in a bladed mixer*. AIChE Journal, 2010. **56**(2): p. 336-353.
79. Remy, B., et al., *Experiments and simulations of cohesionless particles with varying roughness in a bladed mixer*. Chemical Engineering Science, 2010. **65**(16): p. 4557-4571.
80. Yohannes, B., et al., *Scaling of heat transfer and temperature distribution in granular flows in rotating drums*. Phys Rev E, 2016. **94**(4): p. 042902.
81. Chaudhuri, B., F.J. Muzzio, and M.S. Tomassone, *Modeling of heat transfer in granular flow in rotating vessels*. Chemical Engineering Science, 2006. **61**(19): p. 6348-6360.
82. McCarthy, J.J., et al., *Mixing of granular materials in slowly rotated containers*. AIChE Journal, 1996. **42**(12): p. 3351-3363.
83. Bongo Njeng, A.S., et al., *Wall-to-solid heat transfer coefficient in flighted rotary kilns: Experimental determination and modeling*. Experimental Thermal and Fluid Science, 2018. **91**: p. 197-213.
84. Kaneko, Y., T. Shiojima, and M. Horio, *DEM simulation of fluidized beds for gas-phase olefin polymerization*. Chemical Engineering Science, 1999. **54**(24): p. 5809-5821.
85. Morris, A.B., et al., *A conductive heat transfer model for particle flows over immersed surfaces*. International Journal of Heat and Mass Transfer, 2015. **89**: p. 1277-1289.
86. Li, J. and D.J. Mason, *A computational investigation of transient heat transfer in pneumatic transport of granular particles*. Powder Technology, 2000. **112**(3): p. 273-282.
87. Rognon, P. and I. Einav, *Thermal transients and convective particle motion in dense granular materials*. Physical Review Letters, 2010. **105**(21): p. 218301.
88. Mindlin, R.D., *Compliance of elastic bodies in contact*. Journal of Applied Mechanics, 1949. **16**.
89. Yan, Z., et al., *Discrete element modelling (DEM) input parameters: understanding their impact on model predictions using statistical analysis*. Computational Particle Mechanics, 2015. **2**: p. 283-299.
90. Remy, B., J.G. Khinast, and B.J. Glasser, *Discrete element simulation of free flowing grains in a four-bladed mixer*. AIChE Journal, 2009. **55**(8): p. 2035-2048.
91. Lattanzi, A.M. and C.M. Hrenya, *Indirect conduction in gas-solids systems: Static vs. Dynamic effects*. AIChE Journal, 2017. **63**(10): p. 4685-4693.

92. Batchelor, G.K. and R.W. O'Brien, *Thermal or electrical conduction through a granular material*. Proceedings of the Royal Society of London. Series A, Mathematical and Physical Sciences, 1977. **355**(1682): p. 313-333.
93. Moser, D., S. Pannala, and J. Murthy, *Computation of Effective Thermal Conductivity of Powders for Selective Laser Sintering Simulations*. Journal of Heat Transfer, 2016. **138**(8): p. 1-9.
94. Morris, A.B., et al., *Development of soft-sphere contact models for thermal heat conduction in granular flows*. AIChE Journal, 2016. **62**(12): p. 4526-4535.
95. ToolBox, E. *Thermal conductivity of common materials and gases*. Engineering ToolBox 2003; Available from: https://www.engineeringtoolbox.com/thermal-conductivity-d_429.html.
96. Hogg, R., *Mixing and Segregation in Powders: Evaluation, Mechanisms and Processes*. Kona Powder and Particle Journal, 2009(27): p. 3-17.
97. Bridgwater, J., *Mixing of powders and granular materials by mechanical means - A perspective*. Particuology, 2012. **10**(4): p. 397-427.
98. Figueroa, I., W.L. Vargas, and J.J. McCarthy, *Mixing and heat conduction in rotating tumblers*. Chemical Engineering Science, 2010. **65**(2): p. 1045-1054.
99. Nguyen, H.T., et al., *Numerical simulation on the flow and heat transfer of polymer powder in rotational molding*. International Journal of Material Forming, 2014. **8**(3): p. 423-438.
100. Hare, C., M. Ghadiri, and R. Dennehy, *Prediction of attrition in agitated particle beds*. Chemical Engineering Science, 2011. **66**(20): p. 4757-4770.
101. Havlica, J., et al., *Granular dynamics in a vertical bladed mixer: Secondary flow patterns*. Powder Technology, 2019. **344**: p. 79-88.
102. Pantaleev, S., et al., *An experimentally validated DEM study of powder mixing in a paddle blade mixer*. Powder Technology, 2017. **311**: p. 287-302.
103. Sahni, E., et al., *Quantifying drying performance of a filter dryer: Experiments and simulations*. Advanced Powder Technology, 2012. **23**(2): p. 239-249.
104. Lee, J., T.S. Yun, and S.U. Choi, *The Effect of Particle Size on Thermal Conduction in Granular Mixtures*. Materials (Basel), 2015. **8**(7): p. 3975-3991.
105. Guo, Y., et al., *Predicting breakage of high aspect ratio particles in an agitated bed using the Discrete Element Method*. Chemical Engineering Science, 2017. **158**: p. 314-327.
106. Lattanzi, A.M. and C.M. Hrenya, *A coupled, multiphase heat flux boundary condition for the discrete element method*. Chemical Engineering Journal, 2016. **304**: p. 766-773.
107. Balzarini, M.F., et al., *Comparative study of hot air and vacuum drying on the drying kinetics and physicochemical properties of chicory roots*. J Food Sci Technol, 2018. **55**(10): p. 4067-4078.